

# Design of Demountable Toroidal Field Coils with REBCO Superconductors for a Fusion Reactor

by

Franco Julio Mangiarotti

Nuc. Eng., Balseiro Institute (2009)

S.M., Massachusetts Institute of Technology (2013)

Submitted to the Department of Nuclear Science and Engineering  
in partial fulfillment of the requirements for the degree of  
Doctor of Philosophy in Nuclear Science and Engineering  
at the

MASSACHUSETTS INSTITUTE OF TECHNOLOGY

February 2016

© Massachusetts Institute of Technology 2016. All rights reserved.

Author .....

Franco Julio Mangiarotti

Department of Nuclear Science and Engineering

January 19, 2016

Certified by .....

Joseph V. Minervini

Senior Scientist, Division Head, Fusion Technology & Engineering

Thesis Supervisor

Certified by .....

Dennis G. Whyte

Professor and Head, Department of Nuclear Science and Engineering

Thesis Reader

Accepted by .....

Ju Li

Battelle Energy Alliance Professor of Nuclear Science and Engineering

& Professor of Material Science and Engineering

Chair, Department Committee on Graduate Students



# Design of Demountable Toroidal Field Coils with REBCO Superconductors for a Fusion Reactor

by

Franco Julio Mangiarotti

Submitted to the Department of Nuclear Science and Engineering  
on January 19, 2016, in partial fulfillment of the  
requirements for the degree of  
Doctor of Philosophy in Nuclear Science and Engineering

## Abstract

The recent development of REBCO superconducting tapes, cabling methods and joint concepts could be a revolutionary development for magnetic fusion. REBCO has significantly better performance at high magnetic fields than traditional low temperature superconductors (LTS), and can be operated at a higher temperature than LTS for reduced thermodynamic cost of cooling. Use of REBCO superconductors in the magnet systems of tokamaks allows building demountable toroidal field (TF) coils, greatly simplifying reactor construction and maintenance.

A demountable TF coil system with REBCO superconductors for a fusion reactor has been conceptually designed. The coil system operates at 20 K, with a maximum magnetic field of 20 T. The magnets are divided into two coil segments and can be detached and remounted to allow the internal components of the reactor to be removed vertically as one piece. Operating at 20 T and 20 K, the stress in most of the coils is acceptable (less than 2/3 the yield strength and less than 1/2 the ultimate tensile strength of the structural materials). The strain in the superconductors is lower than the reversible degradation limit. The electrical resistance in each conductor joint is 10 n $\Omega$ . The total heat generation in the reactor superconducting TF magnets is approximately 1.9 MW, of which about 25 % is nuclear heating and 75 % joint heating. 71 MW of electricity are required for cooling the coils at 20 K, about 7 % of the electric energy the reactor generates. The expected time to warm-up the magnets from the operation temperature to room temperature is 7 days, and approximately the same for cool-down back to the operation temperature. The analysis of the conceptual magnet design is encouraging, as no insuperable problems have been identified. This conceptual design can be used as a starting point for a full engineering design of demountable fusion reactors magnets.

Thesis Supervisor: Joseph V. Minervini

Title: Senior Scientist, Division Head, Fusion Technology & Engineering

Thesis Reader: Dennis G. Whyte

Title: Professor and Head, Department of Nuclear Science and Engineering



# Acknowledgments

I would like to express my deepest gratitude to my advisor, Dr. Joseph Minervini, for his support, encouragement and advice during my time in MIT. His knowledge and expertise were invaluable to find solutions to my research problems, and to identify the drawbacks my proposed designs had. He has always been very supportive, giving exceptional guidance.

I am very grateful to Dr. Makoto Takayasu for his great assistance in designing and performing the superconductor experiments, and feedback on several details of the design.

I would also like to thank Prof. Dennis Whyte for his enthusiastic support of my research, his very positive comments and advice given during our many meetings, and for reviewing this thesis.

Thanks to Prof. Ronald Ballinger for his advice during our thesis evaluation committee meetings, and for reading and commenting this thesis. Thanks to Prof. Ian Hutchinson for being part of the thesis examining committee and reading the thesis.

Thanks to everyone in the group: Dr. Philip Michael and Dr. Alexey Radovinsky for their ideas and comments regarding the coil design, Dr. Leslie Bromberg for his feedback and assistance with Comsol, Dr. Peter Stahle for his help with the joint experiments.

Thanks to the ARC workgroup, as this project was greatly inspired in ARC. In particular thanks to Prof. Dennis Whyte, Brandon Sorbom, Jennifer Sierchio, Dr. Harold Barnard and Dr. Christian Haakonsen for very useful comments and discussions regarding the magnet and reactor design.

I would also like to thank all the PSFC staff, who helped me in many ways, such as giving advice and data, fabricating or providing parts for my experiments or attending to my seminars and providing criticism. Thanks to Rui Vieira for his comments and ideas regarding the magnet joints, William Beck and Samuel Pierson for experimental equipment and supplies, and Edward Fitzgerald, Dave Tracey and

David Arsenault for building part of the experimental setup. Thanks to Prof. Anne White and Prof. Jeffrey Freidberg for their great advice.

I am grateful for all the support and help I received from my family. Special thanks to my wife Leticia, who is always there for me (from either side of the Atlantic), for her emotional support, her help with my experiments and her advice during the writing of this thesis. I am very very thankful to Peter and Ruth, without their help I would not be here now. Thanks to them and Andreas for receiving me in their house every now and then, for a much needed family break. Thanks to my parents, Celia and Daniel, and to my siblings, Dante, Irene and Sofía, for supporting me every step of the way at six thousand miles away. Thanks to my parents-in-law Blanca and Corsino for their thoughtfulness.

Thanks to my friends in Boston. Mikhail, with whom I shared a home for almost five years; Joaquín, the other *cool* Argentinian in Boston; Silvia, Brandon, Juan, Chuteng and Noemie. Also to those who were in Boston but left: James, Emilio, Iain, Ronaldo and Hans. And to my friends around the world: Fer, Julia, Pablo, Diego, Pablito, Ricar, Marie, Fede, Leo, Manna, Cris, Tito...

This work was supported by the U.S. Department of Energy, Office of Fusion Energy Science under Grant DE-FC02-93ER54186.

# Contents

<b>1</b>	<b>Introduction</b>	<b>15</b>
1.1	Magnetic Fusion Reactors . . . . .	16
1.1.1	Tokamaks as power plants . . . . .	19
1.1.2	Advantages of fusion energy . . . . .	21
1.1.3	Selected existing, planned and designed tokamaks . . . . .	22
1.2	Background of Superconductivity . . . . .	25
1.3	Motivation and Scope of Thesis . . . . .	28
1.3.1	Proposed coil system concept . . . . .	30
1.3.2	Challenges related to the coil system concept . . . . .	32
<b>2</b>	<b>Choice of Materials</b>	<b>35</b>
2.1	Superconductor Properties . . . . .	35
2.2	Conductor grading . . . . .	37
2.3	Structural material choice . . . . .	46
<b>3</b>	<b>Magnet Design and Mechanical Analysis</b>	<b>51</b>
3.1	Magnet Design . . . . .	51
3.2	Stress analysis in the coil . . . . .	56
3.3	Stress analysis in the top joint . . . . .	64
<b>4</b>	<b>Design of the Electrical Joints</b>	<b>71</b>
4.1	Electrical joint concepts . . . . .	71
4.2	Potential joint designs . . . . .	74

4.3	Flat edge joint design characteristics . . . . .	78
4.4	Electrical Joint Insulation . . . . .	81
<b>5</b>	<b>Experimental characterization of Electrical Joints</b>	<b>87</b>
5.1	Pressure distribution on the contact surface . . . . .	89
5.2	Single tapes experiment and joint resistance distribution . . . . .	90
5.2.1	Experimental setup and procedure . . . . .	90
5.2.2	Single tapes results . . . . .	93
5.3	Cable experiment and total joint resistance . . . . .	96
5.3.1	Experimental setup and procedure . . . . .	96
5.3.2	Results for cable experiment . . . . .	98
5.4	Experiment conclusions and influence in the electrical joint design . .	101
<b>6</b>	<b>Cooling Requirements &amp; Maintenance Procedure</b>	<b>107</b>
6.1	Cooling during operation . . . . .	107
6.1.1	Cooling the coil conductors . . . . .	109
6.1.2	Cooling the electrical joints . . . . .	112
6.2	Maintenance protocol . . . . .	116
6.2.1	Coil warm-up and cool-down for maintenance . . . . .	117
<b>7</b>	<b>Conclusions</b>	<b>121</b>
7.1	Summary . . . . .	121
7.2	Applicability to other reactor designs . . . . .	122
7.3	Future Work . . . . .	123
	<b>Appendix A Critical current of REBCO tapes estimation</b>	<b>125</b>
	<b>Appendix B D-Shape calculation algorithm</b>	<b>129</b>
	<b>Appendix C Thermal properties of relevant materials</b>	<b>131</b>
C.1	Copper properties . . . . .	131
C.2	Stainless Steel 316LN properties . . . . .	133
C.3	REBCO tape properties . . . . .	134

C.4 Gaseous Hydrogen . . . . . 135



# List of Figures

1-1	Cross section and reactivity of fusion reactions . . . . .	17
1-2	Schematic drawing of a tokamak . . . . .	19
1-3	Critical surfaces of NbTi and BSCCO-2223 . . . . .	26
1-4	Commercial SuperPower 2G HTS YBCO Wires . . . . .	27
1-5	Cross section of SuperPower 2G HTS YBCO Wire, not to scale . . .	28
1-6	Critical current comparison of REBCO, Nb <sub>3</sub> Sn and NbTi wires at 4.2 K	30
1-7	Conceptual design of the TF coil system . . . . .	31
1-8	Illustration of the key issues addressed in this thesis and their relationships . . . . .	33
2-1	Cross section of SuperPower HTS YBCO Wire, not to scale . . . . .	36
2-2	Critical current of REBCO tapes vs. magnetic field angle to the tape, at several magnetic fields and 22 K . . . . .	37
2-3	Schematic drawing of the winding pack in the inner leg of the TF coils	39
2-4	Schematic drawing of the CICC cross section . . . . .	40
2-5	Maximum magnetic field components and minimum critical current density as a function of layer number . . . . .	41
2-6	Area composition of the TF coils CICC as a function of layer number	45
2-7	Schematic to-scale cross section drawing of the CICC of the first and last layers . . . . .	45
2-8	Plot of strain in the superconducting tape as a function of tensile stress in the structure, for different structural materials, at 20 K . . . . .	48

2-9	Plot of strain in the superconducting tape as a function of tensile stress in the structure, for different structural materials, at 20 K, near 0.4 % strain . . . . .	48
3-1	Conceptual design of the TF coils . . . . .	52
3-2	Mechanical joints concept . . . . .	52
3-3	Electrical joint concept . . . . .	53
3-4	Final conceptual design of the assembled TF coils . . . . .	53
3-5	Final conceptual design of the TF coils, exploded view . . . . .	54
3-6	Geometry of the magnetic field simulation of half a TF coil . . . . .	57
3-7	Toroidal magnetic field results of the magnetic field simulation of half a TF coil . . . . .	57
3-8	Poloidal magnetic field results of the magnetic field simulation of half a TF coil . . . . .	58
3-9	Radial component of Lorentz force in the winding pack from magnetic field simulation . . . . .	58
3-10	Vertical component of Lorentz force in the winding pack from magnetic field simulation . . . . .	59
3-11	Toroidal component of Lorentz force in the winding pack from magnetic field simulation . . . . .	59
3-12	Geometry of the mechanical stress simulation of half a TF coil . . . . .	60
3-13	Stress analysis of the TF coils, for 20 T operation . . . . .	61
3-14	Near the top joint. . . . .	62
3-15	Areas of the TF coils with stresses larger than 750 MPa, for 20 T operation . . . . .	62
3-16	Geometry of the magnetic field simulation of half a top TF electric joint	66
3-17	Magnetic field results of the magnetic field simulation of half a top TF electric joint . . . . .	66
3-18	Lorentz force in the joint from magnetic field simulation . . . . .	67



3-19	Geometry of the mechanical stress simulation of half the top joint of a TF coil . . . . .	68
3-20	Stress analysis of the top TF coil joint, for 20 T operation . . . . .	69
3-21	Areas of the the top TF coil joint with stresses larger than 750 MPa, for 20 T operation . . . . .	70
4-1	Joint options considered . . . . .	73
4-2	Potential displacements and rotations while mounting the top electrical joints . . . . .	75
4-3	Potential joint designs . . . . .	76
4-4	Cross section detail of the electrical joint . . . . .	79
4-5	Coil termination and jumper design . . . . .	80
4-6	Joint mounting procedure . . . . .	82
4-7	Schematic drawing of the insulation in the coil winding pack . . . . .	83
4-8	Schematic drawing of the insulation near the coil terminations . . . . .	83
4-9	Schematic drawing of the insulation in the jumper . . . . .	84
5-1	Components of the electrical joint sample . . . . .	88
5-2	Joint samples soldered . . . . .	88
5-3	Experiment setup for single tapes resistance measurement . . . . .	92
5-4	Voltage vs. current measurement for the single tapes test with feltmetal	94
5-5	Tape-to-tape resistance vs. applied pressure for the joint with felt-metal	94
5-6	Tape-to-tape resistance vs. applied pressure for the joint with 50 $\mu$ m Indium film . . . . .	95
5-7	Tape-to-tape resistance vs. applied pressure for the joint without material between the terminals . . . . .	95
5-8	Cable experiment samples with terminations . . . . .	97
5-9	Experiment setup for cable resistance measurement . . . . .	97
5-10	Voltage vs. current measurement for the cable test with Indium film .	99
5-11	Cable resistance vs. applied pressure for the joint with felt-metal . . .	99

5-12	Cable resistance vs. applied pressure for the joint with $50\mu m$ Indium film . . . . .	100
5-13	Cable resistance vs. applied pressure for the joint without material between the terminals . . . . .	100
5-14	Summary of joint resistance vs. applied pressure for the three surface conditions considered . . . . .	101
5-15	Electrical circuit model of the joint . . . . .	102
5-16	Resistance of bare joint as a function of the inverse square root of the applied average pressure . . . . .	103
5-17	Estimation of the termination-jumper connection resistance for the reactor design . . . . .	106
6-1	Geometry used for the temperature distribution simulation in the coil during operation . . . . .	111
6-2	Temperature distribution in the conductor during operation . . . . .	111
6-3	Schematic drawing of the cooling channels in the joint . . . . .	113
6-4	Geometry used for the temperature distribution simulation of the joint during operation . . . . .	115
6-5	Temperature distribution in the joint during operation . . . . .	115
6-6	Reynolds and Prandtl numbers for gaseous hydrogen heat transfer . . . . .	118
6-7	Temperature in the coil for warming up transient . . . . .	119
6-8	Temperature in the coil for cooling down transient . . . . .	119
7-1	Modification of joint concept for other reactor designs . . . . .	123
A-1	Critical current of REBCO tapes vs. magnetic field angle to the tape, at several magnetic fields and 22 K . . . . .	126

# Chapter 1

## Introduction

The recent advancement of commercially available REBCO<sup>1</sup> superconducting tapes [1, 2], cabling methods [3, 4, 5] and joint concepts [6, 7] could be a revolutionary development for magnetic confinement fusion. REBCO superconductors can operate at much higher magnetic field than traditional low temperature superconductors (LTS) such as  $Nb_3Sn$  and  $NbTi$ . Also, REBCO tapes maintain their good performance at high fields when operated at higher temperatures than LTS [8]. These two traits make REBCO tapes very attractive for high field, high current density applications such as magnetic fusion reactors. These reactors can benefit from the high field performance through an increase of fusion power density, allowing in turn the reactor size to be reduced or the total power generation increased.

Traditionally, superconducting toroidal field (TF) magnets for tokamak fusion reactors have been designed as continuously wound coils, with LTS conductors. Some reactors that have this magnet design are ARIES-I [9] and ITER [10]. Due to this design constraint, which produces a closed topology toroid composed of the individual TF coils, other components that are placed inside these coils must be assembled *in situ*, and complex sector maintenance schemes must be developed to replace the internal parts. The higher operation temperature enabled by the use of REBCO superconductors allows splitting the TF coils in two, a common design choice for

---

<sup>1</sup>Rare Earth Bismuth Copper Oxide. Most commonly in the form of Yttrium Barium Copper Oxide ( $YBa_2Cu_3O_{7-x}$ ), doped with other rare earth elements such as Samarium and Gadolinium, and with other elements such as Zirconium.

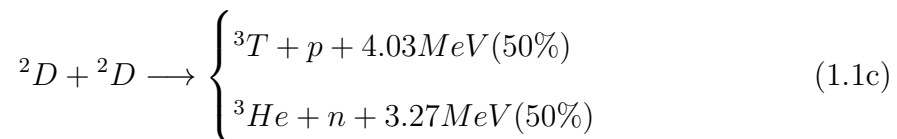
copper conductor magnets, easing the limitations on the construction of the internal components of the reactor, at the relatively low cost (when compared to using LTS) of having higher resistance in the coils. Some reactor studies such as Vulcan [11, 12] and ARC [13] take advantage of this in their reactor design.

This thesis presents a new, demountable TF coil design with REBCO superconductors for an existing fusion reactor design, ARIES-I, chosen due to its relatively conservative plasma physics and aggressive magnet design. The proposed coil design is divided in two parts; the joint areas are on the top of the coil, near the central column, and in the outer mid-plane of the coil. The mechanical and electrical joints are designed to withstand the operating loads and are demountable.

In this chapter, the main characteristics of magnetic fusion reactors and superconductors are discussed. A general background of magnetic fusion reactors, and tokamaks in particular, is given in the first section. The following section presents a general background of superconductivity, and in particular of REBCO superconductors. In the third section the motivations and goals of this thesis work are presented, along with the conceptual design of the proposed TF magnet system.

## 1.1 Magnetic Fusion Reactors

Nuclear fusion is a reaction in which two atomic nuclei collide and form a new, typically larger, atomic nucleus. The three main fusion reactions that are typically considered to produce net energy are as follows, with their energy gain  $Q$  stated in MeV:



These reactions have several technical differences. D-T fusion requires tritium, a

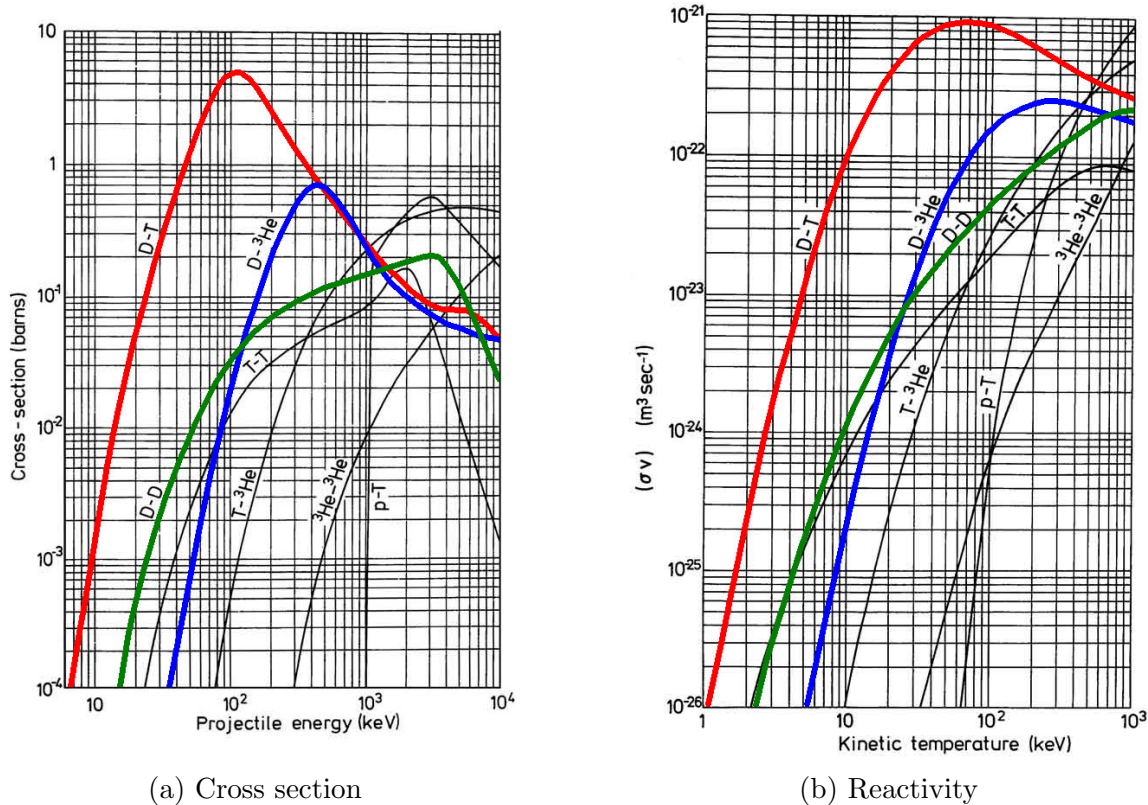


Figure 1-1: Cross section and reactivity of fusion reactions. Plots adapted from [14]. The curves corresponding to D-T, D-D and D-<sup>3</sup>He are highlighted in red, green and blue respectively.

radioactive isotope not naturally available, and must be bred in the reactor through neutron capture of lithium-6 to satisfy its fuel demands. D-<sup>3</sup>He fusion requires helium-3, a very rare stable isotope, usually obtained from the decay of tritium. D-D fusion only requires deuterium, a stable, abundant and easy to obtain hydrogen isotope.

The fusion products are also different in the three reactions. D-T fusion generates a large numbers of neutrons, which activate and damage the structural materials and must be moderated to extract the useful fusion energy. D-<sup>3</sup>He fusion only generates charged particles, with the proton carrying most of the energy, making direct conversion of fusion energy to electricity a possible and attractive option. D-D fusion generates half as many neutrons and protons per fusion event.

The most significant difference from an engineering point of view, however, is the difference in the cross sections ( $\sigma$ ) of the reactions. The cross sections are shown in Figure 1-1a, as a function of the projectile energy. The fuel in thermonuclear

fusion devices will have a Maxwellian velocity distribution characterized by a single temperature; the reactivity ( $\langle\sigma v\rangle$ ) for these nuclear reactions as function of the fuel temperature is shown in Figure 1-1b. The reaction rate ( $f$ , number of fusion events per unit volume and time) of a Maxwellian fusion fuel is:

$$f = A n_1 n_2 \langle\sigma v\rangle \quad (1.2)$$

Where  $n_1$  and  $n_2$  are the volumetric nuclei density of the two fuel species, and  $A$  is 1 if the two species are different or  $1/2$  if the species are the same. The reactivity versus temperature curves for the three reactions look similar, but D-T has its peak at much lower temperatures than D-D and D-<sup>3</sup>He at lower temperatures, making D-T fusion the preferred reaction for fusion power plants. Taking into consideration power balance, the well-known Lawson criterion informs that the optimal D-T operation temperature is about 15 keV, i.e. this temperature requires the lowest product of plasma pressure and energy confinement time. At 15 keV the reactivity of D-T is about two orders of magnitude larger than D-D and D-<sup>3</sup>He. A more detailed explanation of the physics of nuclear fusion can be found in [15], Chapters 2 and 3.

To reach the elevated temperatures required for the fusion reaction, the fusion fuel cannot be in contact with solid materials. There are several possible mechanisms to confine the fuel from contacting room temperature material, but, at present, magnetic confinement fusion is the leading technological solution for the challenge of achieving controlled fusion reactions on Earth. This confinement concept is based on the fact that, in the presence of a magnetic field, charged particles follow helical trajectories around it. Magnetic confinement fusion devices maintain the fusion fuel as a plasma with temperature in excess of 15 keV achieved in the laboratory. The magnetic field configuration in these devices allow the particles to be confined in a finite space. While some experiments utilize open magnetic field lines configurations (such as solenoids or magnetic bottles), toroidal configurations with closed magnetic field lines are the leading geometry for all major fusion reactors.

### 1.1.1 Tokamaks as power plants

Tokamaks are magnetic confinement fusion devices, with the plasma confined in an axisymmetric torus by strong toroidal magnetic fields. The tokamak is the most promising fusion device, from a power generation perspective [15]. In Figure 1-2 a schematic drawing of a tokamak is shown. The fusion fuel in the plasma state is shown in yellow, contained inside a vacuum chamber. The blanket surrounds the vacuum chamber completely on the outside. The main component within the blanket is a material rich in lithium-6 and neutron moderators and multipliers. It moderates the fusion neutrons, absorbing the neutron energy by converting to thermal energy and then further used to generate electric power and provides the tritium breeding reaction. The blanket also shields the magnets from most of the nuclear radiation induced by the highly penetrating 14.1 MeV neutrons produced by the D-T fusion reaction.

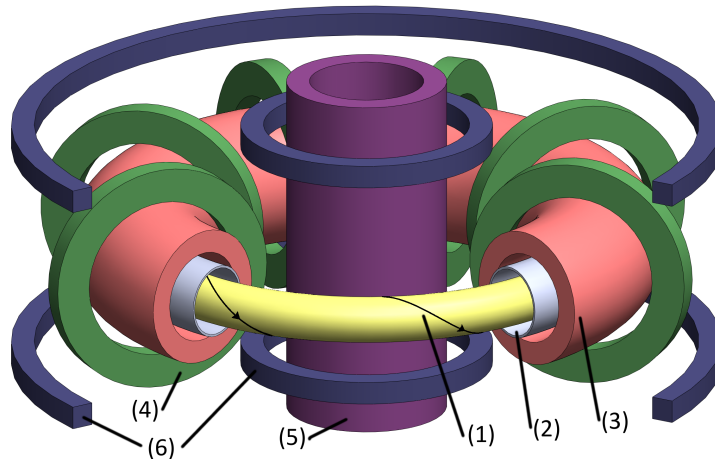


Figure 1-2: Schematic drawing of a tokamak. The fusion fuel (1) is in plasma state, inside a vacuum chamber (2). The blanket (3) acts as neutron moderator and shield, and is where tritium is bred. The toroidal field coils (4), poloidal field coils (5) and central solenoid (6) generate the required magnetic field (black arrows) for plasma stability.

Three kinds of magnets generate the required magnetic field: the toroidal field is generated by the toroidal field (TF) coils, and the poloidal field is generated by the central solenoid (CS) and the poloidal field (PF) coils. The different magnet systems

usually are required for different functions, and have different operation patterns: the TF coils are operated at constant current and are required for the background toroidal magnetic field for stabilizing the plasma; the CS is a pulsed magnet used for plasma start-up and shaping, and it is often used as a transformer (inducing a toroidal current in the plasma); the PF coils are used for plasma shaping and position control, and normally their current is adjusted as needed during the reactor operation.

A tokamak power plant would likely operate with D-T fuel. From equation (1.2), the optimum fuel mixture would be equal parts of both isotopes at density  $n/2$ . In this situation, the total fusion power generated ( $P_F$ ) would be

$$P_F = \int 17.6 \text{ MeV } f \, dr^3 = \int 17.6 \text{ MeV } \frac{n^2}{4} \langle \sigma v \rangle \, dr^3 \quad (1.3)$$

Where the integral is over the plasma volume ( $V_P$ ). At the plasma temperatures of interest ( $T$ , about 15 KeV), the reaction rate of D-T fuel is approximately proportional to the square of the plasma temperature. Replacing the plasma pressure ( $p = nT$ ) into equation (1.3):

$$P_F \propto \int p^2 \, dr^3 \quad (1.4)$$

An important tokamak parameter is the toroidal beta ( $\beta_T$ ), the ratio of the plasma pressure to the magnetic pressure, defined as:

$$\beta_T = \frac{2\mu_0 \bar{p}}{B_0^2} \quad (1.5)$$

with  $\bar{p}$  the volume averaged plasma pressure and  $B_0$  the toroidal magnetic field on the plasma axis, which defines the major radius  $R_0$  of the plasma toroid. The  $\beta_T$  factor is limited by magneto-hydrodynamic stability, and in general reactor designs assume an operating  $\beta_T$  close to this limit. Replacing equation (1.5) into (1.4) yields:

$$\frac{P_F}{V_P} \propto \bar{p}^2 \propto \beta_T^2 B_0^4 \quad (1.6)$$

Equation (1.6) highlights the importance of the magnitude of the toroidal magnetic



field in a fusion reactor. High magnetic fields yield much higher power density ( $\frac{P_F}{V_P}$ ), which in turn allows either increasing the total energy production of the reactor, or reduction of its volume. A central motivation to this thesis is to explore the possibility of doubling  $B_0$  compared to existing superconductor magnet technology since this provides an order-of-magnitude improvement in power density. Some reactor designs, as will be shown in Section 1.1.3, leverage high magnetic field designs in one or both of these directions.

### 1.1.2 Advantages of fusion energy

Nuclear fusion energy has several advantages over traditional and renewable energy sources, such as hydrocarbons and natural gas combustion, wind and solar power, and nuclear fission energy.

- Practically limitless fuel reserves in the planet: Deuterium is abundant in nature and relatively easy to obtain. Tritium does not exist in nature, but can be generated from Lithium-6. World reserves of these two isotopes (Deuterium and Lithium-6) can generate enough power for the entire world for over 20,000 years at the present electricity demand rate.
- Reduced radioactive waste: the Deuterium-Tritium nuclear reaction generates Helium-4 (a stable isotope) and neutrons. The neutrons may interact with the structural elements near the plasma core, however the irradiated materials (such as stainless steel) have a relatively short half-life. After plant decommissioning, the irradiated materials would only require about 100 years of storage for the radiation levels to be low enough to not pose any public hazard.
- Low production of greenhouse gases: as no oil or carbon derivatives are burned in a fusion power plant, the greenhouse gases production would be minimal or non-existent.
- High availability: a fusion reactor would generate energy as a baseload plant, without any limitations imposed by environmental events (such as clouds, rain,

time of day or high or low wind speed).

- No meltdown danger: the amount of fuel in the reactor at any moment is very small, and an out-of-control chain reaction is impossible. Even though the fuel temperature is very high, its collision against the reactor vessel would not be enough to cause structural damage to the reactor.

Fusion energy production is an attractive alternative to other energy sources. It can generate reliable energy in steady state without the unwanted greenhouse gases and high level radioactive waste byproducts. A lengthier discussion about different sources of energy can be found in [15], Chapter 1.

### 1.1.3 Selected existing, planned and designed tokamaks

In this subsection several tokamak designs of interest are presented. The first set of reactors described are either built or under construction; the designs described afterward are conceptual designs without any present construction plans. In Table 1.1 the main parameters of these reactors are shown. Note that this list is not exhaustive.

#### **Built and under construction:**

- JET (Joint European Torus) is the world's largest (in terms of plasma volume) magnetic confinement plasma physics experiment, located at Culham Science Centre in Oxfordshire, UK. It achieved first plasma in 1983, and in 1997 it produced 16.1 MW of fusion power, the current world record [22].
- JT-60 was a tokamak located in Ibaraki Prefecture, Japan. It was in operation from 1985 to 2010, and in 1996 it achieved the world record of fusion triple product<sup>2</sup>:  $1.53 \cdot 10^{21} keV s/m^3$ . The reactor is currently being upgraded, changing its coils to NbTi superconducting coils and renamed JT-60SA. Operation is expected to start by 2019 [23, 24].

---

<sup>2</sup>The fusion triple product is a figure of merit of the operation conditions of the fusion reactor. It is the product of plasma density, temperature and confinement time. The minimum required triple product to reach net power production is  $3 \cdot 10^{21} keV s/m^3$ .

Table 1.1: Comparison between selected reactor designs

Reactor	$R_0$ [m]	$B_0$ [T]	Coil material	$P_F$ [MW]
<i>Built and under construction</i>				
JET [16]	2.96	4.0	Copper	16
JT-60 [16]	3.40	4.2	Copper/NbTi	–
DIII-D [16]	1.66	2.2	Copper	–
Alcator C-MOD [16]	0.67	8.0	Copper	–
EAST [16]	1.75	3.5	NbTi	–
KSTAR [16]	1.80	3.5	Nb <sub>3</sub> Sn	–
ITER [16]	6.20	5.3	Nb <sub>3</sub> Sn	500
<i>Conceptual Designs</i>				
ARIES-I [9]	6.75	11.3	Nb <sub>3</sub> Sn, NbTi	1925
A-SSTR2 [17]	6.20	11.0	BSCCO-2212	5000
VECTOR [18, 19]	3.75	4.7	BSCCO/REBCO	1800
PPCS-A [20]	9.55	7.0	Nb <sub>3</sub> Sn	5000
Vulcan [11]	1.20	7.0	REBCO	–
ARC [13]	3.30	9.2	REBCO	525
ARIES-ACT1 [21]	6.25	6.0	Nb <sub>3</sub> Sn	1813
ARIES-ACT2 [21]	9.75	8.75	Nb <sub>3</sub> Sn	2637

References: major radius  $R_0$ , toroidal magnetic field at the major radius  $B_0$ , and fusion power  $P_F$ .

- DIII-D is a tokamak located in San Diego, California, USA. It the largest magnetic fusion user facility in the U.S. It started operations in 1986. It has a flexible shaping coil systems that allow to produce a variety of plasma shapes [25].
- Alcator C-Mod is a tokamak at the MIT Plasma Science and Fusion Center, located in Cambridge, Massachusetts, USA. It is the tokamak with the highest toroidal magnetic field and highest plasma pressure. It started operations in 1993 [26].
- EAST (Experimental Advanced Superconducting Tokamak) is a tokamak located in Hefei, China. It started operations in 2006. It is one of the first

divertor topology tokamaks to have fully superconducting magnets, made of NbTi [27].

- KSTAR (Korea Superconducting Tokamak Advanced Research) is a tokamak located in Daejeon, South Korea. It achieved first plasma in 2008. It is one of the first shaped divertor tokamaks to have completely superconducting magnets: its toroidal field coils are built with Nb<sub>3</sub>Sn and the poloidal field coils with Nb<sub>3</sub>Sn and NbTi [28].
- ITER (International Thermonuclear Experimental Reactor and Latin for “the way”) is a tokamak under construction in Cadarache, France. It is an international project, funded by China, the European Union, India, Japan, Russia, South Korea and the United States. It will be the largest tokamak in the world, with more than twice the major radius of JET. Construction started in 2006, and first plasma is expected by 2025 [29]. It will have fully superconducting magnets: its central solenoid and toroidal field coils will use Nb<sub>3</sub>Sn superconductors, and its poloidal field coils will use NbTi superconductors. ITER is expected to reach 500 MW of fusion power [30].

### **Reactor concept designs:**

- ARIES-I is the first reactor design from the ARIES program, a US-based integrated fusion reactor design activity. It is a design with conservative plasma physics but aggressive magnet engineering, with the goal of producing 1 GW of steady-state electric power. It has been selected as the base design for this thesis work. [9]
- A-SSTR2 is a relatively large (2.55 GW net electric power) steady state power plant design by JAERI in Japan. It is high-field, using BSCCO-2212 high temperature superconductors in the TF coils. [17]
- VECTOR is a tight aspect ratio reactor concept, designed by JAERI in Japan. Due to its low aspect ratio, the maximum magnetic field in the TF coils is

similar to high-field reactors, but the field on plasma axis is similar to ITER. Its original design used BSCCO-2212 as superconductor for the TF coils [18], and REBCO superconductors were considered in a later publication [19].

- PPCS-A is one of the five reactors designed in the European power plant conceptual study (PPCS) [20]. These reactors are conceived as the bridge between ITER and a first-of-a-kind fusion power plant, and thus use similar technology such as  $\text{Nb}_3\text{Sn}$  superconductors.
- Vulcan is a compact reactor designed at MIT for plasma-material interaction research. It has high-field and has demountable TF coils based on REBCO superconductors to allow easier change of the plasma facing components for testing [11].
- ARC is a compact, high-field reactor designed at MIT. It is inspired by Vulcan, also having demountable TF coils and REBCO superconductors. Its modular design allows ARC to be used as a power plant and also as a fusion nuclear science facility [13].
- ARIES-ACT are the latest designs from the ARIES program. ARIES-ACT includes four reactor concepts, with conservative and advanced assumptions both of the plasma physics and of the engineering technology used. The two designs analyzed in more detail are ACT1 (advanced physics and advanced technology) and ACT2 (conservative physics and conservative technology) [21].

## 1.2 Background of Superconductivity

Superconducting materials have zero electrical resistivity under certain conditions. Most commonly, the superconductive state is reached by sufficiently lowering the temperature of the material, typically below 4–100 K. The other two major factors that influence the superconducting property of these materials are the electrical current density through the superconductor, and the external magnetic field applied to

it. Additionally, some types of superconducting materials are sensitive to mechanical strain.

At a given temperature and applied magnetic field, the maximum current density that the material can carry while remaining in the superconductive state is called the *critical current density* ( $J_C$ ). As an example, the surface of critical current density vs. temperature and magnetic field (the *critical surface*) of two different superconductors are shown in Figure 1-3. The *critical temperature* of the superconductor is the highest temperature at which the material is still superconductive.

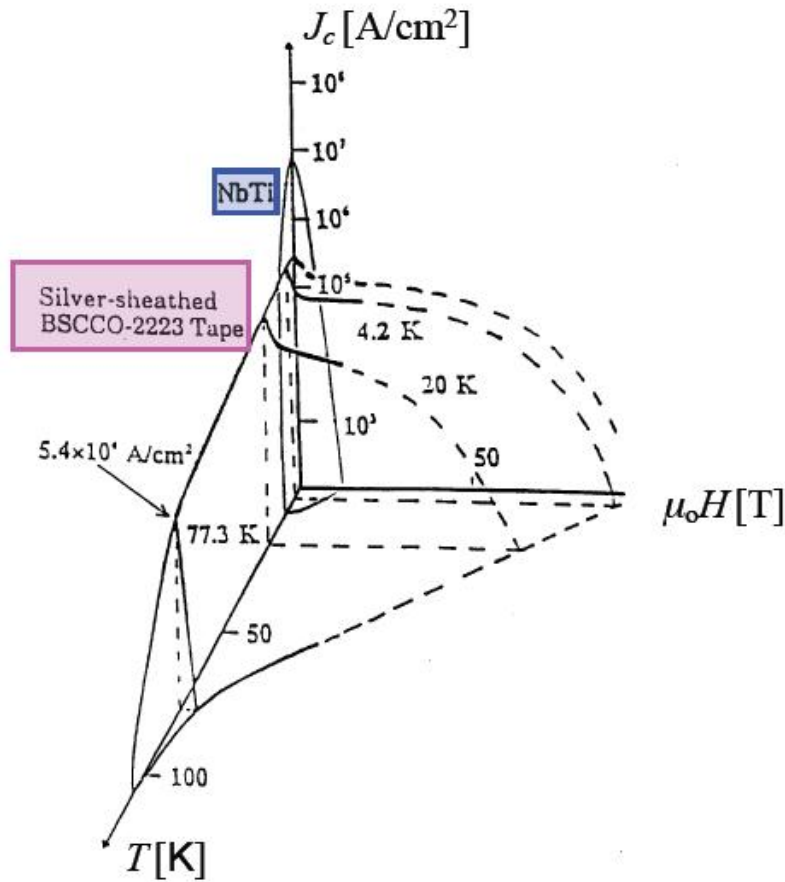


Figure 1-3: Critical surfaces of NbTi and BSCCO-2223 [31]. The materials are only superconducting when they operate in the space inside these surfaces. Note the logarithm scale for current density.

Often, commercially available superconductors are divided in two groups: *low temperature superconductors* (LTS) such as  $Nb_3Sn$  and  $NbTi$ , and the *high temperature*

*superconductors* (HTS) such as *REBCO* and *BSCCO*<sup>3</sup>. There are several differences between LTS and HTS; the most important are the critical temperature at low magnetic field (for LTS close to liquid helium, for HTS higher than liquid nitrogen), and the material characteristics (LTS are metallic alloys or compounds, while HTS are ceramics). Also, LTS were discovered decades earlier than HTS, and thus the development of fabrication and cabling methods for LTS conductors are much more advanced.

Low temperature superconductors NbTi and Nb<sub>3</sub>Sn, and high temperature superconductor BSCCO-2212 are commercially available in fine round wires. REBCO and BSCCO-2223 conductors are commercially available as tapes, usually 0.1–0.3 mm thick and 4–12 mm wide. BSCCO conductors in general have much lower strength than REBCO conductors, due to differences in the material composition. For high temperature, high mechanical load applications REBCO is generally the preferred option.

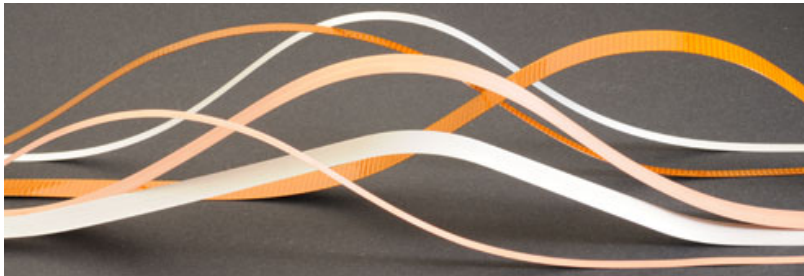


Figure 1-4: Commercial SuperPower 2G HTS YBCO Wires [32]. Tapes are 2–12 mm in width and 0.1 mm in thickness. Note the ease with which the tapes bend in plane.

In Figure 1-4 a picture of REBCO tapes manufactured by SuperPower Inc. is shown, and in Figure 1-5 a detail of the cross section of a standard commercial configuration. Depending on the manufacturer and model, different tape configurations are available; however, in all cases layers with high electrical resistivity are present (in the case of the figure, the substrate -hastelloy- and the buffer layers), allowing low resistance current transfer into or out of the REBCO layer only from the opposite side of the tape. The substrate is a high strength material, and provides mechanical

<sup>3</sup>Bismuth Strontium Calcium Copper Oxide. There are two main compounds: BSCCO-2212 ( $Bi_2Sr_2CaCu_2O_{8+x}$ ) and BSCCO-2223 ( $Bi_2Sr_2Ca_2Cu_3O_{10+x}$ ).

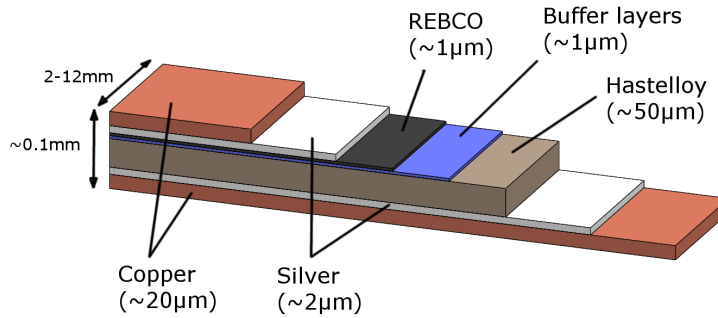


Figure 1-5: Cross section of SuperPower 2G HTS YBCO Wire, not to scale. The superconductor layer is  $1 \mu\text{m}$  thick.

support for the brittle REBCO layer.

Several cabling methods for making high current REBCO cables have been proposed, such as helical windings on a round former [33], ROEBEL cabling of tapes cut in a zigzag pattern [34], conductors on round core (CORC) [4] and twisting stacked tape cables (TSTC) [3, 35]. TSTC provides high current density, efficient tape usage and allows constructing cables for high current density and high magnetic field applications, such as nuclear fusion reactors.

### 1.3 Motivation and Scope of Thesis

REBCO superconductors can be a game-changer innovation for fusion reactors. When at high magnetic field, REBCO TF coils with a small resistance operating at relatively high temperature (20–30 K) have a lower thermodynamic cost of cooling and much greater thermal stability than traditional LTS TF coils at their operation temperature of 4.2 K. Because of this, continuous winding is not the only option for REBCO coils, and they could be built with a series of small resistance joints. Indeed due to the present limitations for the length of HTS tapes of about 1 km, it is likely that for the large scale coils required in fusion the use of joints will be necessary. The joints location can be engineered to make the REBCO TF coils demountable in a way that the internal components of the tokamak can be accessed from the top of the machine with a standard crane.



Traditional tokamak designs, such as ARIES-I and ITER, have continuously wound superconducting coils. Due to this design constraint, the internal components of the reactor (such as vacuum vessel, blanket, cooling conduits) have to be assembled *in-situ* with a strategy that is called “sector maintenance”. Since these components are the most damaged from the fusion reactions, a yearly maintenance would require removing and re-assembling them, with tight tolerances, in a radioactive environment. In the case of ITER, which must use sector maintenance where all internal components are removed in sections between the TF coils, the expected intervention time for removing a single blanket module is 2 months, and changing the entire blanket would take 2 years [36].

With this new approach of demountable TF coils, the internal components can be vertically removed as a full piece. The vacuum vessel and plasma facing components can be built *ex-situ*, in a specialized factory where achieving higher tolerances would be possible. This also allows for a liquid blanket design, such as that proposed in ARC [13]. The expected maintenance tasks for this reactor concept are outlined in Chapter 6; two of the expected slower tasks, magnet warm-up and cool-down between the operation temperature and room temperature, are expected to last about 7 days each.

Besides the higher operation temperature, REBCO allows for a higher magnetic field operation, as is shown in Figure 1-6 because unlike LTS the critical current has very little degradation up to and past 30 T. This will allow for superconducting coils that operate in the 23–30 T range, which is not accessible with LTS. The use of REBCO conductors instead of LTS for coils in nuclear fusion would greatly improve the performance, as has been proposed in several studies [12, 13, 19, 39].

The goal of this thesis is to conceptually design a new demountable TF coil system with REBCO superconductors for an existing fusion reactor design. The design has to provide vertical access to the internal components of the tokamak, reasonably fast and with reliable assembly protocols and low probability of operation failure. The coil system concept is presented in the next subsection; the second subsection discusses the key issues of the design and the strategy to evaluate it.

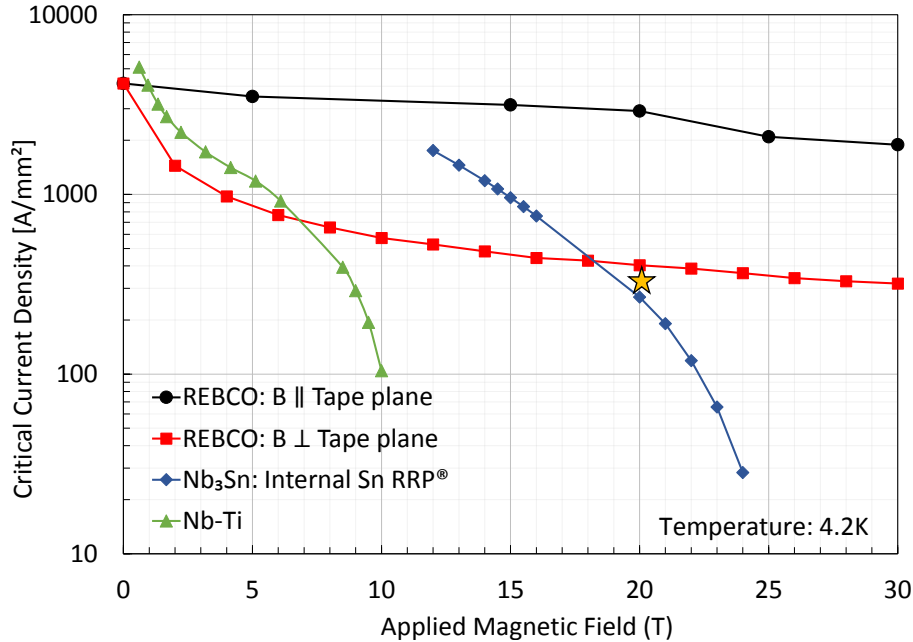


Figure 1-6: Critical current comparison of REBCO, Nb<sub>3</sub>Sn and NbTi wires at 4.2 K. Data compiled by Peter Lee in 2014 [37]. For magnetic fields larger than 18 T, at 4.2 K, REBCO outperforms both low temperature superconductors. REBCO superconductor has higher critical current density when the magnetic field is parallel to the tape plane; new REBCO tapes formulations, such as those from University of Houston [38], have higher critical current density perpendicular to the magnetic field (more than 1000 A/mm<sup>2</sup> at 30 T). The yellow star represents the superconductor operating point (current density and magnetic field) at the highest magnetic field area and 20 K for the proposed demountable T coils.

### 1.3.1 Proposed coil system concept

The fusion reactor concept ARIES-I was used as baseline and starting design point. This reactor was chosen due to its relatively conservative plasma physics and aggressive magnet design. The main parameters of the reactor are presented in Table 1.2.

The TF magnet concept is shown in Figure 1-7. The TF coil system will have 16 coils, supported in the central column by wedging against each other. The coils will use REBCO superconductors, cooled by liquid hydrogen at 20 K. They are divided in two parts; the joint areas are on the top of the coil, near the central column, and in the outer mid-plane of the coil. The mechanical and electrical joints are designed to withstand the operating mechanical loads and are demountable. The electrical joints have a small electrical resistance, and are located further outside the mechanical

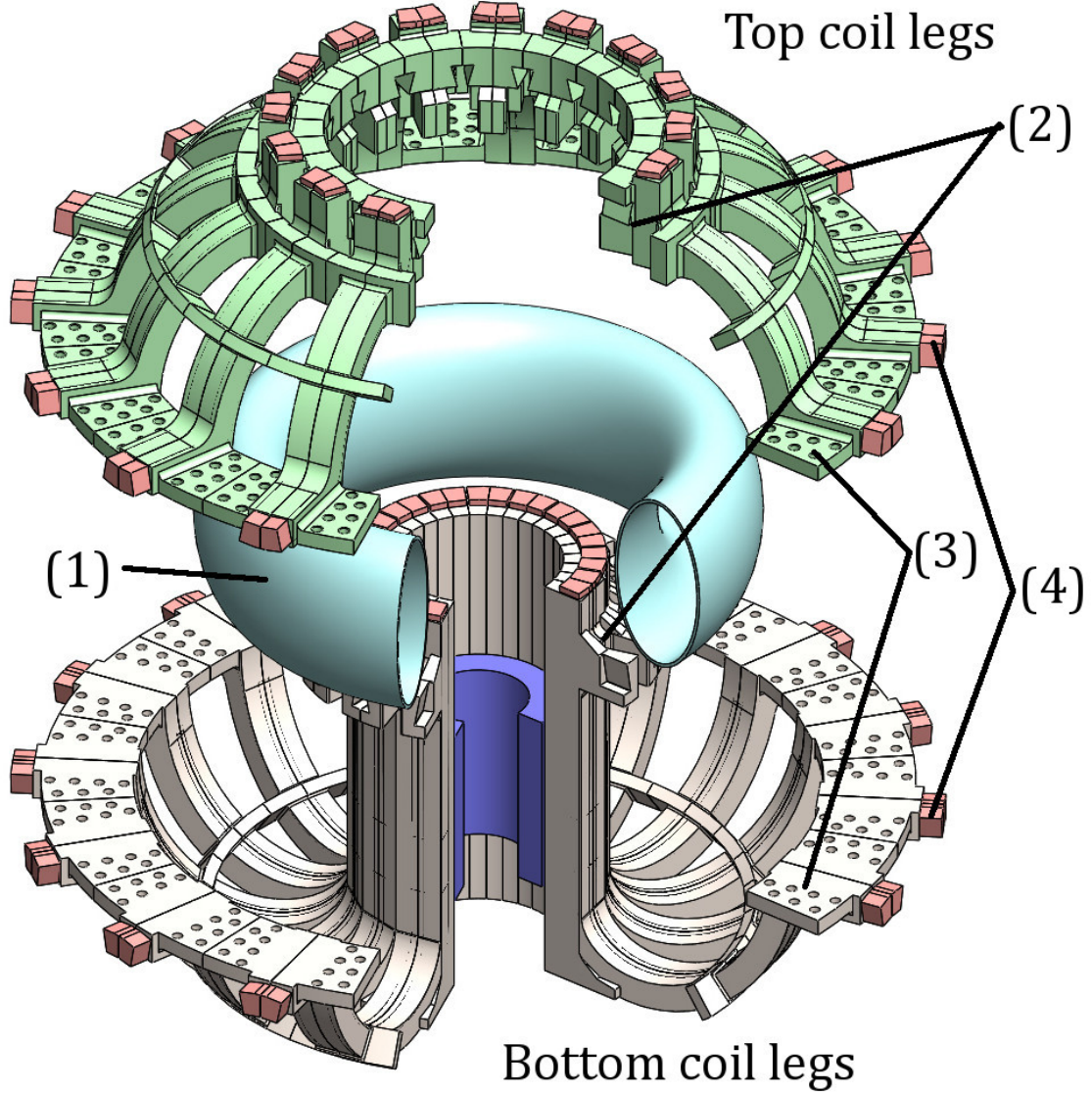


Figure 1-7: Conceptual design of the TF coil system. The coils are disassembled, with the vacuum vessel (1) in the process of being removed. The coils are supported by wedging against each other. The coil mechanical joints are (2) and (3). (2) is a triple dovetail joint, (3) is a bolted joint. (4) are the electrical terminations. The electrical joint is located at the electrical terminations, connected with auxiliary joint structures (not shown).

Table 1.2: Design parameters of ARIES-I [9, 40]

Quantity	Magnitude
Major radius	6.75 m
Aspect ratio	4.5
Maximum magnetic field on TF coil	20 T
Magnetic field on plasma axis	11 T
Number of TF coils	16
Net electrical power generated	1000 MW
Normalized beta	3.2 %
Greenwald density fraction	0.61
Kink safety factor on plasma edge	4.85
L-mode confinement enhancement factor	1–2

joints to reduce the mechanical load on them. The bottom part of the TF coils are stationary, and the top part will be removable vertically. The total weight of the removable part of the coil system is 4800 metric tons, a weight that can be lifted by modern cranes. The demountable coil geometry has negligible effect on the magnetic field uniformity, compared with ARIES-I continuously wound coils.

### 1.3.2 Challenges related to the coil system concept

The most important issues related to the proposed TF coil design are shown in Figure 1-8: the large forces in the coils, the joints and the maintenance time evaluation. That figure also outlines the strategy to analyze whether the issues will be show-stoppers, or if a satisfactory engineering solution can be found. It must be noted that the scope of this thesis is to roughly assess the viability of the magnet design, and not to perform a full engineering design of the coils. Therefore most of the subsystems described in the following chapters are only conceptually designed.

To evaluate the mechanical response to the large forces in the coils, a study of the coil grading will be necessary in order to decide if strong enough structural materials are available. This is discussed in Chapter 2.

The magnet and joint design are presented in Chapter 3, and stress simulations

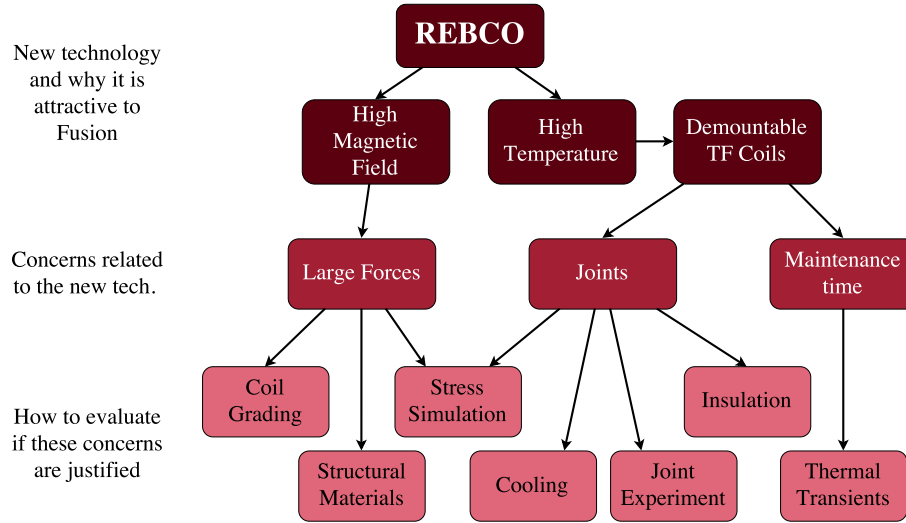


Figure 1-8: Illustration of the key issues addressed in this thesis and their relationships.

of the coil and the mechanical joint are also reported in that chapter.

The design of the electrical joints and their insulation is discussed in Chapter 4. The results of a small scale joint experiment is presented in Chapter 5, with an estimation of the performance of the electrical joints. Evaluation of the cooling requirements of the reactor during operation is given in Chapter 6.

To estimate the required maintenance time, a calculation of cooling-down and warming-up times is reported in Chapter 6, with some additional approximations of the required time to perform other tasks such as joint disassembly and replacement of internal components.

Chapter 7 concludes this thesis with a summary of the results, and feedback to improve the design and expected future work.



# Chapter 2

## Choice of Materials

### 2.1 Superconductor Properties

Commercially available REBCO tapes are usually composed of several layers, as is shown in Figure 2-1. The REBCO layer typically represents only 1 % of the tape thickness. When in the superconducting state all the current through the REBCO tape flows in the REBCO layer, therefore the electrical properties of the tapes depend mostly on the properties of the thin REBCO layer. The mechanical properties, on the other hand, depend mostly on the substrate (hastelloy in the figure) and coating (copper) layers. In this thesis the REBCO tapes will be assumed to be *SuperPower HTS YBCO Wire*, with 50  $\mu\text{m}$  thick hastelloy substrate and two 20  $\mu\text{m}$  thick copper coating layers. In Table 2.1 relevant mechanical properties of these REBCO tapes and the main components are summarized.

The most important electrical property of REBCO superconductors is the critical current density ( $J_C$ ). It depends on several factors: the magnitude and orientation of the applied magnetic field, temperature and strain. However the REBCO tapes production is not yet fully optimized, and year after year new developments improve  $J_C$  and different aspects of its dependence to magnetic field, temperature and strain, making older publications of REBCO tapes characterization present lower values than what is achievable today. Therefore, the values presented in this section must not be taken as the maximum  $J_C$  attainable, but as a conservative approximation of its

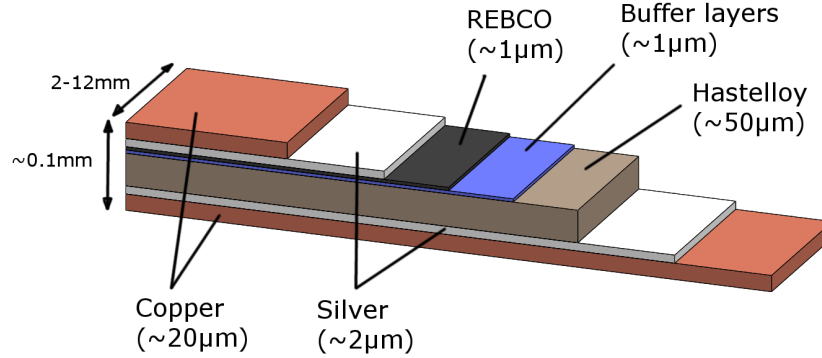


Figure 2-1: Cross section of SuperPower HTS YBCO Wire, not to scale. The superconductor layer is  $1 \mu\text{m}$  thick, which corresponds to 1 % of the tape thickness. The substrate layer is hastelloy, its thickness  $50 \mu\text{m}$ . The superconductor tape is coated with copper  $20 \mu\text{m}$  thick on each side.

Table 2.1: Mechanical properties SuperPower HTS YBCO Wire and its components.

Material	E [GPa]	TE [%]
SuperPower tape [41]	161	-0.291*
Hastelloy C276 [42, 43]	205	-0.29
Copper [44]	138	-0.293

References: elastic modulus  $E$  at 4.2 K and thermal expansion  $TE$  from 300 K to 4.2 K. \*: calculated as the weighted average of hastelloy and copper.

value.

A correlation of critical current density at 22 K ( $J_C^{22}$ ) as function of the magnetic field and its angle was made. The details of how this correlation was calculated are discussed in Appendix A. In Figure 2-2 the value of  $J_C^{22}$  versus the angle between the magnetic field and the normal direction to the tape is shown for several magnetic fields, calculated according to equation (A.1).

Tensile strain in the superconducting layer reduces the critical current density. Several studies [45, 46] have shown that regardless of the composition of the REBCO tape, the critical current of the tape is reduced by 5 % at a strain level of 0.4–0.45 %. The irreversible degradation of critical current usually occurs at around 0.6 % strain.



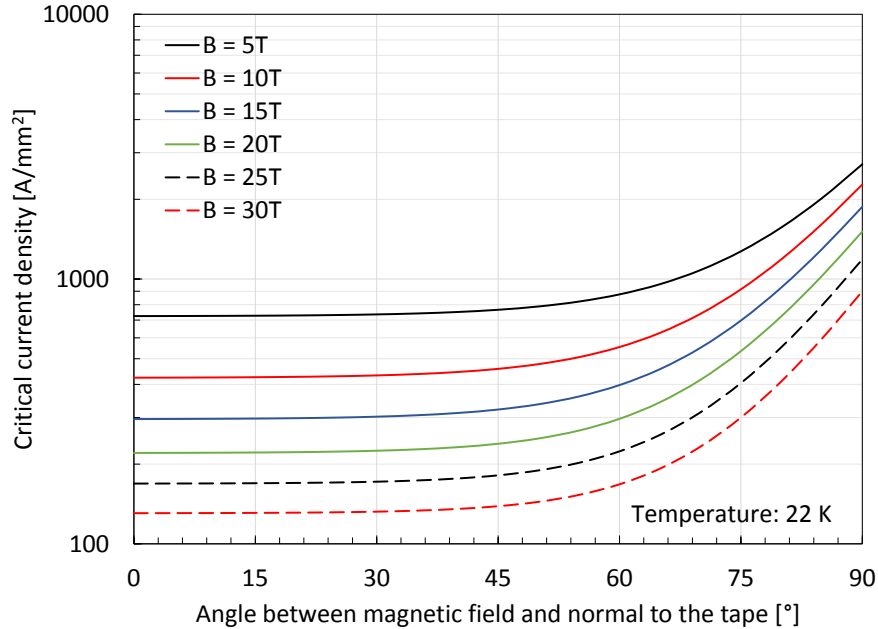


Figure 2-2: Critical current of REBCO tapes vs. magnetic field angle to the tape, at several magnetic fields and 22 K. The data shown here was calculated with the correlation described in Appendix A, and was used for the calculations in Section 2.2.

For the purposes of this work the strain influence in the critical current will be ignored, but the maximum tensile strain in the tape will be kept below 0.4 %.

## 2.2 Conductor grading

The TF coil winding pack is composed by 13 graded layers of cable-in-conduit conductors (CICC). The innermost six layers (closest to the plasma) have 20 turns, the other seven layers have 18 turns, for a total of 246 turns per TF coil. The CICC are composed of a 60 mm square jacket, with a square conductor inside composed of copper stabilizer and six REBCO stacks. The copper stabilizer has a 7 mm cooling channel in its center. The REBCO stacks are aligned such that the toroidal magnetic field is parallel to the tape. The structural material that composes the jacket was not decided at this point, and will be discussed in Section 2.3. A schematic drawing of the winding pack in the inner leg of the TF coils and some relevant dimensions are shown in Figure 2-3, and a schematic drawing of the cross section of the CICC is

shown in Figure 2-4.

The total required current in each TF coil  $I_{TF}$  can be calculated as follows:

$$I_{TF} = \frac{1}{N_{TF}} \frac{2\pi}{\mu_0} R_0 B_0 \quad (2.1)$$

where  $N_{TF}$  is the number of TF coils,  $R_0$  is the major radius of the tokamak, and  $B_0$  the toroidal magnetic field on plasma axis. Substitution in equation (2.1) with the data from Table 1.2, the current per TF coil is 23.2 MA turn. At 246 conductors per coil, the corresponding conductor current ( $I_{CICC}$ ) is approximately 94 kA.

In each layer, the minimum critical current density will be in the area of maximum magnetic field. The maximum toroidal magnetic field  $B_T^{Max}(L)$  in each layer  $L$  was calculated from Ampère's law as follows:

$$B_T^{Max}(L) = \frac{\mu_0}{2\pi R(L)} \sum_{l=L}^{13} I_{CICC} N(l) \quad (2.2)$$

with  $R(L)$  the radial position of layer  $L$  and  $N(l)$  the number of conductors in layer  $l$ . The maximum combined radial magnetic field  $B_R^{Max}(L)$  in each layer  $L$  was estimated from a finite element simulation of the magnetic field produced by the central solenoid and poloidal field coils, based on the ARIES-I design. The value of  $B_R^{Max}(L)$  is approximately:

$$B_R^{Max}(L) = 2.5T + 5.5 \frac{T}{m^2} (R(L) - 3.25m)^2 \quad (2.3)$$

The total maximum magnetic field  $B^{Max}(L)$  is calculated as:

$$B^{Max}(L) = \sqrt{[B_T^{Max}(L)]^2 + [B_R^{Max}(L)]^2} \quad (2.4)$$

And the angle  $\theta(L)$  between the normal to the tape surface and the magnetic field is calculated as:

$$\theta(L) = \arctan \left( \frac{B_T^{Max}(L)}{B_R^{Max}(L)} \right) \quad (2.5)$$

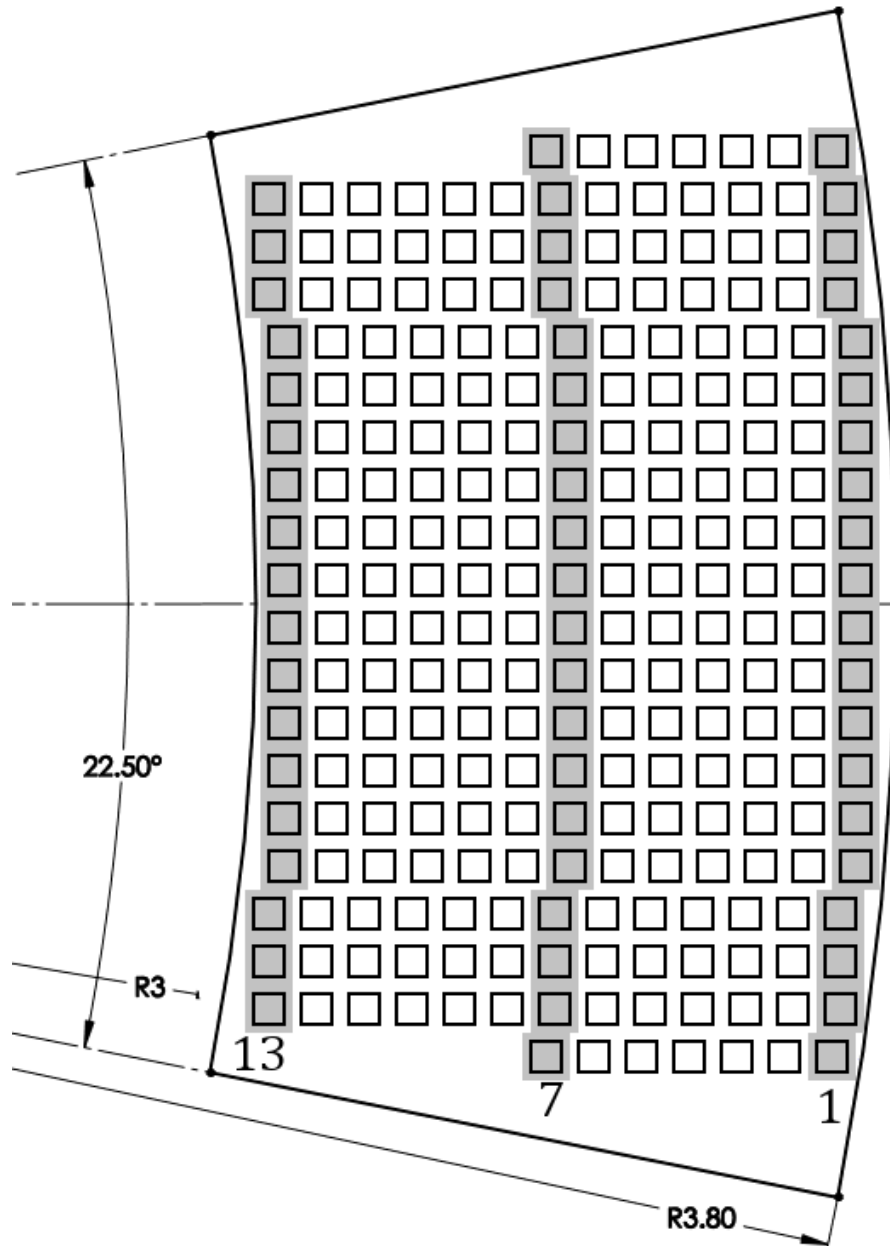


Figure 2-3: Schematic drawing of the winding pack in the inner leg of the TF coils. Dimensions in meters. The squares correspond to the approximate location of the copper and superconductor part of the conductors in the coil. Three layers are highlighted: #1 is the innermost layer, #7 is the middle layer and #13 is the last layer.

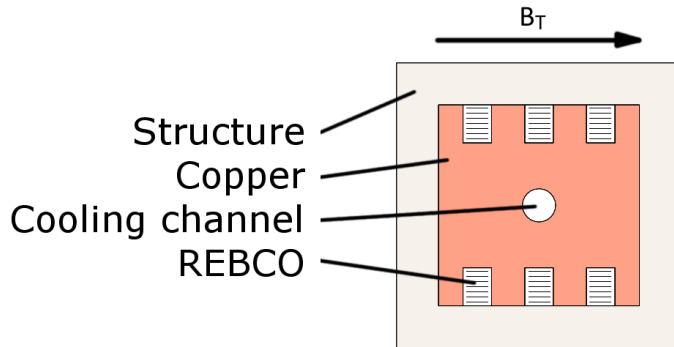


Figure 2-4: Schematic drawing of the CICC cross section. The lines in the REBCO stacks represent the orientation of the tapes. The toroidal magnetic field  $B_T$  is parallel to the REBCO tapes as represented with the black arrow.

The minimum critical current density of each layer  $J_C(L)$  is calculated using equations (2.4) and (2.5) in (A.1):

$$J_C(L) = J_C^{22}(B^{Max}(L), \theta(L)) \quad (2.6)$$

The maximum toroidal and radial components of the magnetic field, and the minimum critical current density in each layer are shown in Figure 2-5. As a conservative calculation, the amount of REBCO tapes in each layer is calculated such that the current density does not exceed 50 % of the minimum critical current density. The required cross sectional area of superconducting tapes  $A_{SC}(L)$  is determined as:

$$A_{SC}(L) = 2 \frac{I_{CICC}}{J_C(L)} \quad (2.7)$$

The amount of copper is determined such that in case of a quench, the conductor does not exceed 200 K, as recommended by Iwasa in [47], Chapter 8. If a quench occurs, the superconductor locally becomes normal. Assuming all the superconductors in a cross section become normal, the current starts flowing in the copper. The conductor starts heating up locally due to Joule heat; the heat generation per unit length is:

$$[A_{Cu}(L)\delta_{Cu}c_{Cu}(T) + A_{SC}(L)\delta_{SC}c_{SC}(T)] \frac{dT}{dt} = \frac{\rho_{cu}(T, B)}{A_{Cu}(L)} I^2(t) \quad (2.8)$$

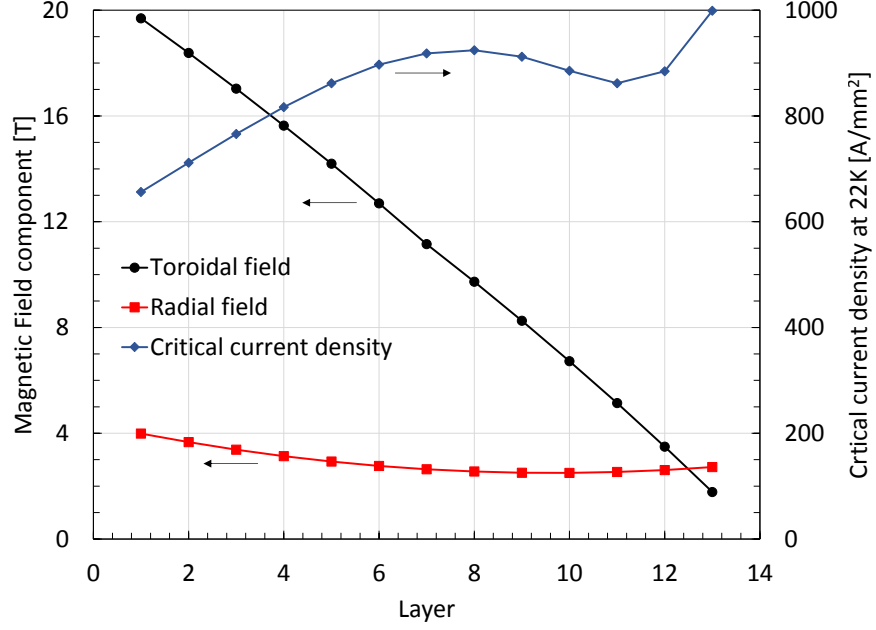


Figure 2-5: Maximum magnetic field components and minimum critical current density as a function of layer number. The first layer is the innermost layer (closest to the plasma), as shown in Figure 2-3. The operating current density in each layer is 50 % of the minimum critical current density.

where  $A_{Cu}$  is the area of copper in layer  $L$ ,  $\delta_{Cu}$  and  $\delta_{SC}$  the mass density of copper and superconductor tape respectively,  $c_{Cu}(T)$  and  $c_{SC}(T)$  the specific heat of copper and superconductor respectively (both functions of temperature  $T$ ),  $\rho_{cu}(T, B)$  the electrical resistivity of copper (a function of temperature and magnetic field  $B$ ) and  $I$  the current through the conductor (a function of time  $t$ ). The density and specific heat of the main components of the superconductor tape (Hastelloy [43] and copper) are very similar; to simplify the calculations, the properties of the superconducting tape will be assumed to be the same as copper, yielding:

$$[A_{Cu}(L) + A_{SC}(L)] \delta_{Cu} c_{Cu}(T) \frac{dT}{dt} = \frac{\rho_{cu}(T, B)}{A_{Cu}(L)} I^2(t) \quad (2.9)$$

At a given temperature, the resistivity of copper increases with higher magnetic field. To simplify the calculations the magnetic field in the copper region will be assumed (conservatively) to be constant and equal to the maximum magnetic field in layer  $L$ . Rearranging these terms, and integrating between the initial values  $T = T_i$

and  $t = 0$ , and final values  $T = T_f$  and  $t = t_f$  yields:

$$[A_{Cu}^2(L) + A_{Cu}(L)A_{SC}(L)] \int_{T_i}^{T_f} \frac{\delta_{Cu}c_{Cu}(T)}{\rho_{Cu}(T, B^{Max}(L))} dT = \int_0^{t_f} I^2(t) dt \quad (2.10)$$

For a fixed maximum magnetic field, the left integral depends only on the initial and final temperature values. The temperature dependency of the resistivity and specific heat are summarized in Appendix C. For a temperature change from 20 K to 200 K, the value of this integral  $Z(L)$  is:

$$Z(L) = \int_{20K}^{200K} \frac{\delta_{Cu}c_{Cu}(T)}{\rho_{Cu}(T, B^{Max}(L))} dT \quad (2.11)$$

After a quench, the current  $I$  is kept equal to the operation value  $I_{CICC}$  for a time  $\tau_1$ , until the quench is detected and confirmed. At that point the coils are shunted by discharge resistors, and the power supply is turned off; the current decays exponentially with a characteristic time  $\tau_2$ . Assuming the final time is infinite:

$$\int_0^{t_f} I^2(t) dt = \int_0^{\tau_1} I_{CICC}^2 dt + \int_{\tau_1}^{\infty} \left[ I_{CICC} \exp\left(-\frac{t - \tau_1}{\tau_2}\right) \right]^2 dt \quad (2.12a)$$

$$= I_{CICC}^2 \left( \tau_1 + \frac{1}{2} \tau_2 \right) \quad (2.12b)$$

Replacing equations (2.11) and (2.12b) into equation (2.10) and solving for  $A_{Cu}(L)$ :

$$A_{Cu}(L) = \frac{A_{SC}(L)}{2} \left[ \sqrt{1 + 4 \left( \frac{I_{CICC}}{A_{SC}(L)} \right)^2 \frac{\tau_1 + \tau_2/2}{Z(L)}} - 1 \right] \quad (2.13)$$

The value of  $\tau_1$  is 7 s, estimated as three times the expected ITER time value (2.2 s [48]) from quench start to quench detection and confirmation, rounded up. The value of  $\tau_2$  is calculated as:

$$\tau_2 = \frac{L_{TF}}{R_{Dis}} \quad (2.14)$$

where  $L_{TF}$  is the TF coils inductance and  $R_{Dis}$  the discharge resistance. Each TF coil will be connected to a discharge resistor; the value of the resistance is estimated assuming the maximum voltage per TF coil in case of quench is equal to that of ITER:

$$\frac{R_{Dis}}{N_{TF}} I_{CICC} = \frac{R_{Dis}^I}{N_{TF}^I} I_{CICC}^I \quad (2.15)$$

where  $N_{TF}$  is the number of TF coils, and the super-index ‘‘I’’ denotes the values of the corresponding quantity for ITER. The discharge resistance is then:

$$R_{Dis} = \frac{N_{TF} I_{CICC}^I}{N_{TF}^I I_{CICC}} R_{Dis}^I \quad (2.16)$$

The value of the TF coils inductance is estimated from the stored magnetic energy  $E_{TF}$  and the current in the conductors ( $I_{CICC}$ ) as:

$$E_{TF} = \frac{1}{2} L_{TF} I_{CICC}^2 \quad (2.17)$$

This equation allows to compare the inductance of the present design with the inductance of ITER:

$$L_{TF} = \frac{E_{TF}}{E_{TF}^I} \left( \frac{I_{CICC}^I}{I_{CICC}} \right)^2 \cdot L_{TF}^I \quad (2.18)$$

Replacing equations (2.18) and (2.16) into equation (2.14) and substituting  $\tau_2^I = L_{TF}^I / R_{Dis}^I$  yields:

$$\tau_2 = \frac{E_{TF}}{E_{TF}^I} \frac{N_{TF}^I I_{CICC}^I}{N_{TF} I_{CICC}} \tau_2^I \quad (2.19)$$

For reference the maximum voltage per TF coil in case of quench  $V_Q$  is calculated as follows:

$$V_Q = \frac{R_{Dis}}{N_{TF}} I_{CICC} = \frac{L_{TF} I_{CICC}}{16 \tau_2} \quad (2.20)$$

Replacing  $L_{TF}$  from equation (2.17):

$$V_Q = \frac{2E_{TF}}{N_{TF}\tau_2 I_{CICC}} \quad (2.21)$$

All the values in equations (2.19) and (2.21) are available in [10] for ITER and in [9] for the ARIES-I design. For convenience they are summarized in Table 2.2, along with the calculated value of  $\tau_2$ : 29 s.

Table 2.2: ITER and ARIES-I TF coil properties relevant for equation (2.19).

Quantity	ITER	ARIES-I
Stored magnetic energy $E_{TF}$ [GJ]	41	132
Number of coils $N_{TF}$	18	16
Current in conductor $I_{CICC}$ [kA]	68	94
Maximum quench voltage $V_Q$ [kV]	6.1	6.1
Discharge time constant $\tau_2$ [s]	11	29

Table 2.3: Composition of layers 1, 7 and 13.

Layer	1	7	13
Structure	50.2 %	54.7 %	58.6 %
Copper	40.7 %	38.5 %	35.1 %
REBCO	8.0 %	5.7 %	5.2 %
Cooling channel	1.1 %	1.1 %	1.1 %

The area fraction for superconductor, copper, structure and cooling channel is shown in Figure 2-6, and a scaled drawing of the cross section of the first and last layers CICC is shown in Figure 2-7. The composition of the first, middle and last layers are summarized in Table 2.3. Layer 1 requires the largest amount of superconductor, equivalent to 6 stacks of 80 tapes 6 mm wide. This conductor design is conservative in several aspects: the current density does not exceed 50 % of the minimum local critical current density, calculated taking into account the maximum toroidal and radial magnetic field in the conductor layer. The critical current density of the tapes is a conservative approximation of its value, as the performance of REBCO tape superconductors is still being improved by manufacturers. Lastly, the



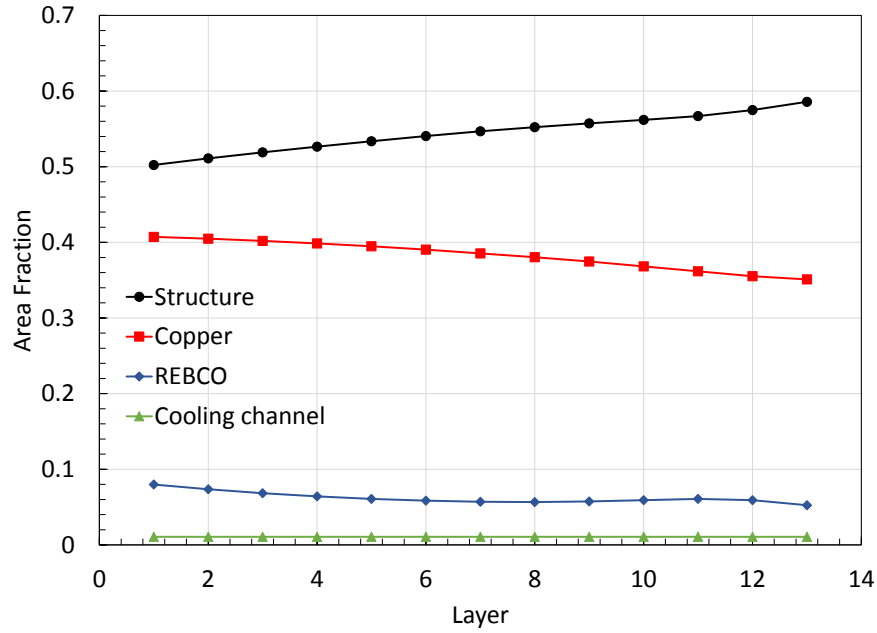


Figure 2-6: Area composition of the TF coils CICC as a function of layer number. The first layer is the innermost layer (closest to the plasma), as shown in Figure 2-3.

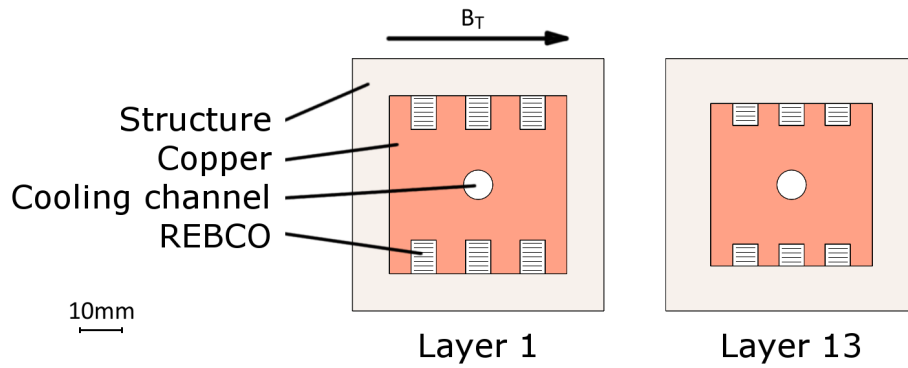


Figure 2-7: Schematic to-scale cross section drawing of the CICC of the first and last layers. The scale on the left is 10 mm. Layer 1 requires 6 stacks of 80 REBCO tapes, 6 mm wide; layer 13 requires 52 tapes of the same width in each of the 6 stacks. The lines in the REBCO stacks represent the orientation of the tapes. The toroidal magnetic field  $B_T$  is parallel to the REBCO tapes as represented with the black arrow.

required amount of copper is such that in a quench, the temperature in the superconductors does not exceed the conservative value of 200 K.

## 2.3 Structural material choice

There are a number of conditions the structural material must meet to be considered for the coil structure. The material must support the large Lorentz forces in the conductors without yielding, and have a reasonable ductility and fracture toughness. It also must be stiff enough to keep the strain in the superconducting tapes lower than 0.4 %, as discussed in Section 2.1. The material must be relatively easy to machine.

A first list of potential materials was made from commonly used or considered structural materials in other fusion reactor magnets. Additionally, other materials with significantly higher yield strength or stiffness were considered as candidates, because the stresses overall are expected to scale as the square of the magnetic field. A list of these materials and their properties is presented in Table 2.4. Most materials are not properly characterized at 20 K, and their properties at 4.2 K or at 77 K were used instead, depending on data availability.

To compare several materials a simplified model was used, for the composition of the first layer of the coil. In this case, the tensile strain in the superconducting tape ( $\epsilon_T$ ) depends on the tensile stress in the conductor ( $\sigma_C$ ) as follows:

$$\epsilon_T = \frac{\sigma_C}{E_{Eff}} + \Delta\epsilon_{\Delta T} \quad (2.22)$$

where  $E_{Eff}$  is the effective elastic modulus of the conductor at 20 K, and  $\Delta\epsilon_{\Delta T}$  is the thermal contraction difference between the whole conductor and the superconductor from 300 K to 20 K.  $E_{Eff}$  is calculated as:

$$E_{Eff} = x_{St}E_{St} + x_{Cu}E_{Cu} + x_T E_T \quad (2.23)$$

with  $x_i$  and  $E_i$  the proportion and elastic modulus of the material  $i$ , and the sub-indexes  $T$ ,  $Cu$  and  $St$  meaning superconducting tape, copper and structure re-

Table 2.4: Mechanical properties of structural material candidates.

Material	E [GPa]	$\sigma_Y$ [MPa]	UTS [MPa]	RA [%]	$K_{1C}$ [MPa $\sqrt{m}$ ]	TE [%]
Type 316LN [49, 50]	193 $\flat$	1122 $\flat$	1534 $\flat$	40 $\flat$	222 $\flat$	-0.33
Haynes 242 [50]	229 $\dagger$	1340	1968	21	142	-0.2
18Ni(250) [51]	186 $\dagger$	2250 $\natural$	2340 $\natural$	27 $\natural$	120 $\dagger$	-0.283 $\natural$
CSUS-JN1 [52, 53]	203	1336	1812	44	214	-0.272
Incoloy 908 [54, 50]	177	1216	1694	28	185	-0.17
Inconel 718 [55, 56]	211	1408	1816	20.2	112.3	-0.213
Inconel x750 [56]	223 $\natural$	1085 $\natural$	1696 $\natural$	42 $\natural$	–	-0.22 $\natural$
Hastelloy C276 [42, 43]	205	809	–	–	–	-0.29
Zylon 90% [57, 58]	255 $\natural$	–	5070 $\natural$	–	–	0.18 $\natural$
Tungsten [59]	360 $\dagger$	517 $\dagger$	759 $\dagger$	–	–	-0.14 $\natural$

List of properties for different materials: elastic modulus  $E$ , yield strength  $\sigma_Y$ , ultimate tensile strength  $UTS$ , area reduction  $RA$ , fracture toughness  $K_{1C}$  and thermal expansion  $TE$ . Data measured at 4.2 K unless noted:  $\dagger$  for data at 300 K,  $\natural$  for data at 77 K,  $\natural$  for data at 20 K and  $\flat$  for data at 7 K. Thermal expansion is from 300 K to 4.2 K unless noted:  $\natural$  from 300 K to 20 K.

spectively. The thermal contraction difference  $\Delta\epsilon_{\Delta T}$  is calculated as:

$$\Delta\epsilon_{\Delta T} = x_{St} TE_{St} + x_{Cu} TE_{Cu} - (1 - x_T) TE_T \quad (2.24)$$

with  $TE_i$  the thermal expansion from 300 K to 20 K of the material  $i$ . Note that most materials contract when cooling from 300 K to 20 K, thus their corresponding thermal expansion would be negative. The only material of those considered in Table 2.4 with a positive thermal expansion is Zylon, making it unattractive for structural material in the winding pack.

A plot of the strain in the superconducting tape vs the applied tensile strain in the conductor is shown in Figure 2-8, and a close-up of this plot near 0.4 % tape strain is shown in Figure 2-9. These plots allow one to quickly evaluate the performance of the different materials, comparing the stress in the structure that corresponds to 0.4 % strain in the tape ( $\sigma_{0.4}$ ). The four best materials using this metric are:

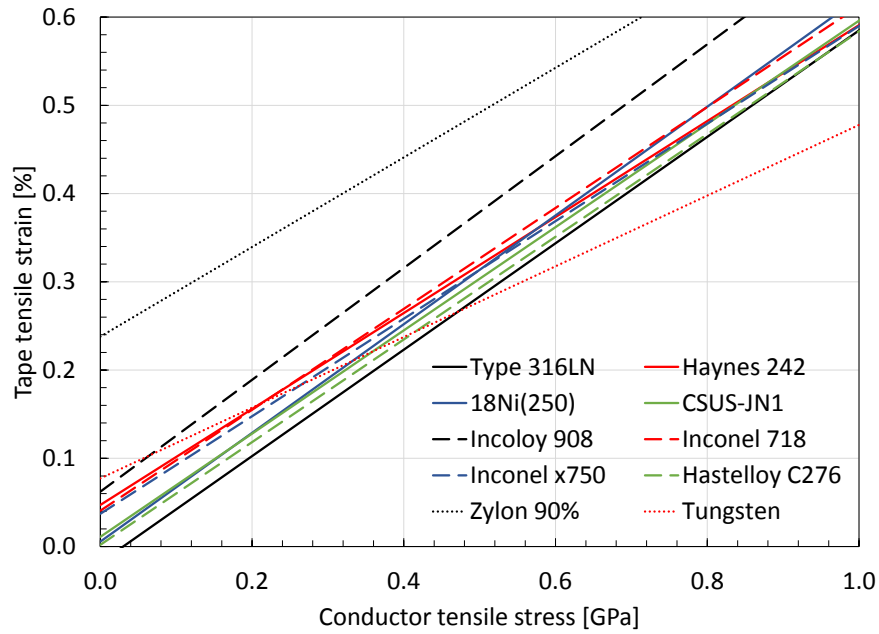


Figure 2-8: Plot of strain in the superconducting tape as a function of tensile stress in the structure, for different structural materials, at 20 K.

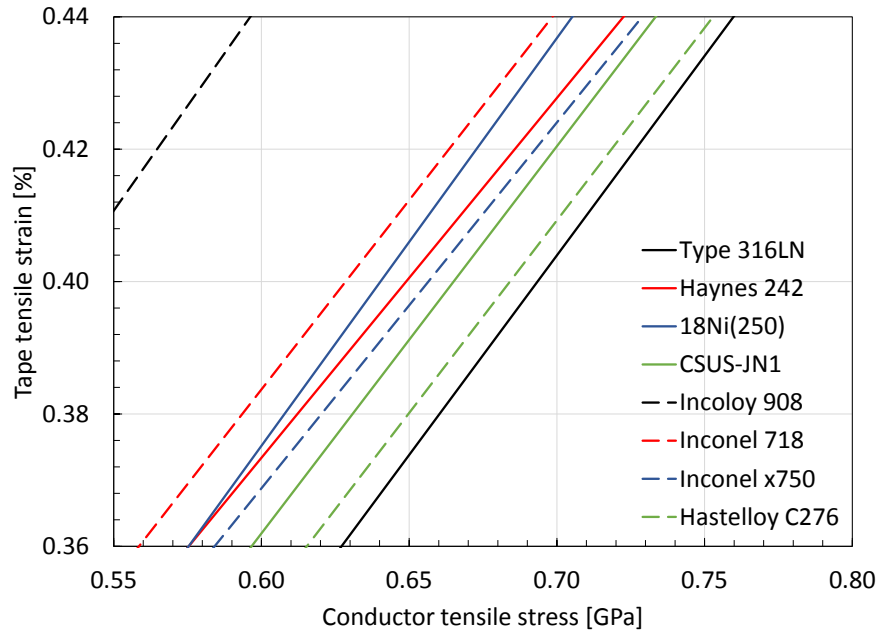


Figure 2-9: Plot of strain in the superconducting tape as a function of tensile stress in the structure, for different structural materials, at 20 K, near 0.4 % strain. The best materials, which allow the highest conductor stress within the allowed strain, are Stainless steel 316LN, Hastelloy C276 and CSUS-JN1.

- Tungsten:  $\sigma_{0.4} = 810 \text{ MPa}$ . Tungsten is the highest on the list due to its high stiffness. However, tungsten is very brittle at these temperatures, is very hard to machine and its properties are not well studied for cryogenic structural use, therefore it was discarded as an option.
- Stainless steel 316LN:  $\sigma_{0.4} = 690 \text{ MPa}$ . This material was thoroughly tested for use in ITER TF coils [49], and its yield strength is around 1122 MPa. Stainless steel 316LN was chosen as the structural material for the TF coils.
- Hastelloy C276:  $\sigma_{0.4} = 685 \text{ MPa}$ . This material is used as substrate for REBCO superconducting tapes by some manufacturers, including SuperPower Inc. It is not attractive as a structural material because of its low yield strength (only 809 MPa at 4.2 K).
- CSUS-JN1:  $\sigma_{0.4} = 665 \text{ MPa}$ . This material has similar properties to 316LN and also has been thoroughly tested for use in fusion reactors [52], but its performance is slightly worse and is less common in large scale production compared with 316LN, and it was not chosen as the structural material for the coils.

It must be noted that data for most of the materials considered is not complete at 4–20 K. Further evaluation of material properties, in particular 18Ni(250), might change the conclusion from these curves. Also, improving the mechanical resistance to strain of the REBCO tapes might allow for a higher total stress. For instance, if the REBCO tapes could be manufactured such that their maximum allowed strain was 0.6 % instead of 0.4 %, stainless steel 316LN would not be a good option because it would operate close to its yield stress, while CSUS-JN1 and 18Ni(250) would still have a significant margin to yield.



# Chapter 3

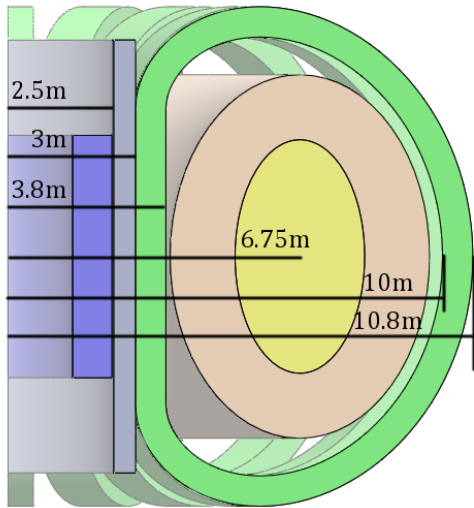
## Magnet Design and Mechanical Analysis

### 3.1 Magnet Design

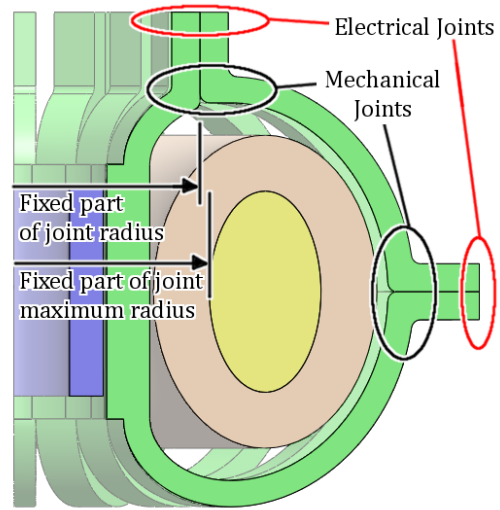
As was mentioned in Section 1.3, the ARIES-I design was used as a baseline and starting point for the TF coils design. The radial build of ARIES-I TF coils was extracted from [9], and used to obtain the base D-shape with the Matlab code presented in Appendix B. A poloidal cross section of the base D-shape TF coil is shown in Figure 3-1a, with relevant dimensions noted.

The ARIES-I design includes a bucking cylinder to support the the inner leg of the TF coils. For this design, the bucking cylinder was removed in favor of a thicker TF coil to support the coils inner leg by wedging.

The joints in the coil are in the outer mid-plane and on the top of the coil. The location of the top joint is limited by the size of the vacuum vessel, imposing a maximum radius of the non-removable part such that the vacuum vessel can still be removed vertically. To improve the reliability of the joints between the legs of the coil, their mechanical and electrical aspects are separated: the mechanical joints are closer to the center of the coil, and the electrical joints are further away from the plasma chamber, to minimize the forces in the electrical joint area. This concept is

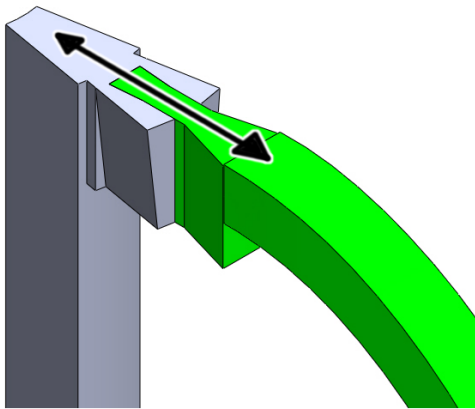


(a) Cross section of baseline D-shape TF coil from ARIES-I.

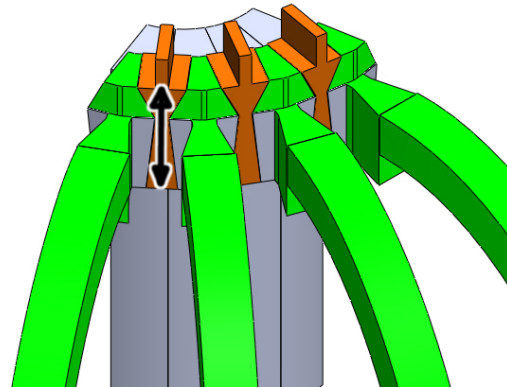


(b) Modification on the baseline TF coil to allow for two joints.

Figure 3-1: Conceptual design of the TF coils. Note that the bucking cylinder from the ARIES-I design (in dark gray) was removed in favor of a thicker TF coil to support the coils inner leg by wedging.



(a) Conceptual design of the triple dovetail mechanical top joint, first stage: the top leg (in green) of the TF coil slides vertically in the inner leg (gray), and a dovetail in the top leg supports the radial force (represented by the arrow).



(b) Conceptual design of the triple dovetail mechanical top joint, second stage: an auxiliary part (orange) slides in radially between adjacent TF coils, with a double dovetail in an hourglass-shape to support the vertical forces (represented by the arrow).

Figure 3-2: Mechanical joints concept.



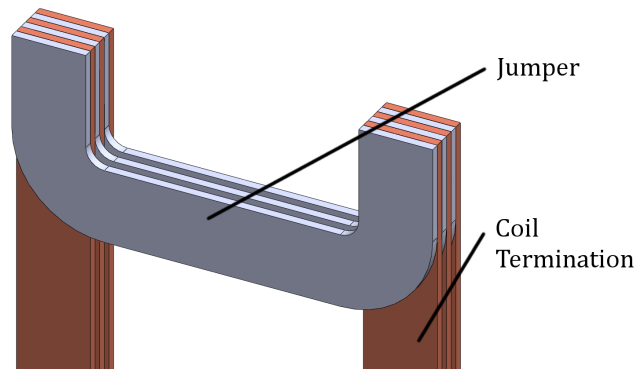


Figure 3-3: Electrical joint concept. The current in the coil termination and in the jumper flow in opposite directions in the contact area, producing a negligible net local magnetic field. This reduces the net Lorentz force on the jumper segment ends. The net vertical Lorentz force in the jumper is taken by a separate structural component.

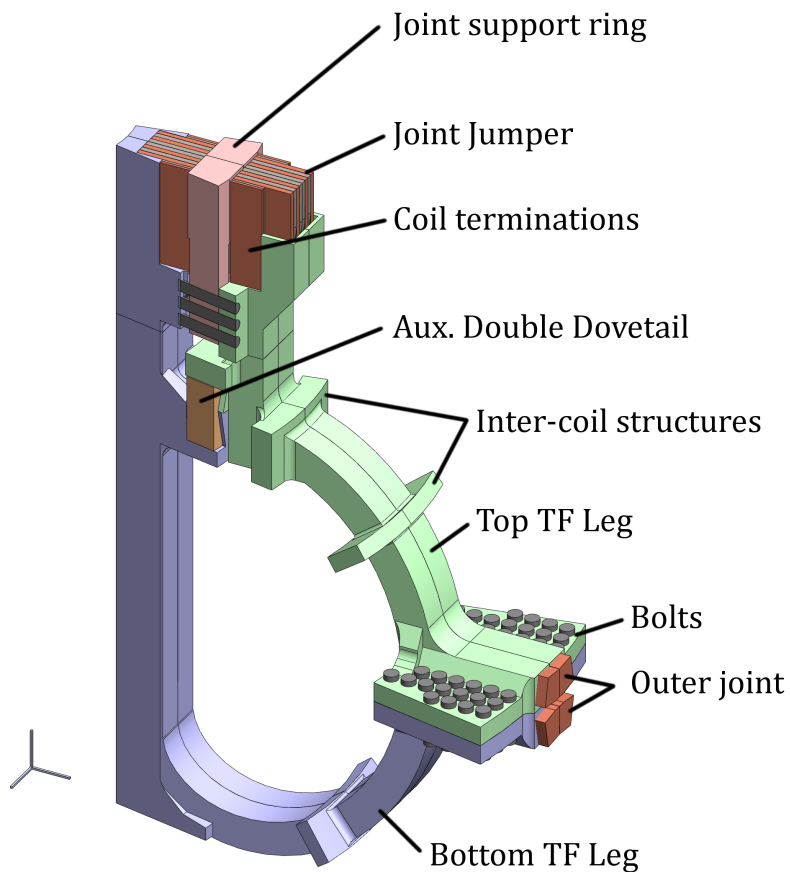


Figure 3-4: Final conceptual design of the assembled TF coils. A  $22.5^\circ$  section is shown, corresponding to a single coil, with its parts named. The outer midplane electrical joint is not shown for clarity. The scale in the bottom left is 1 m in each direction.

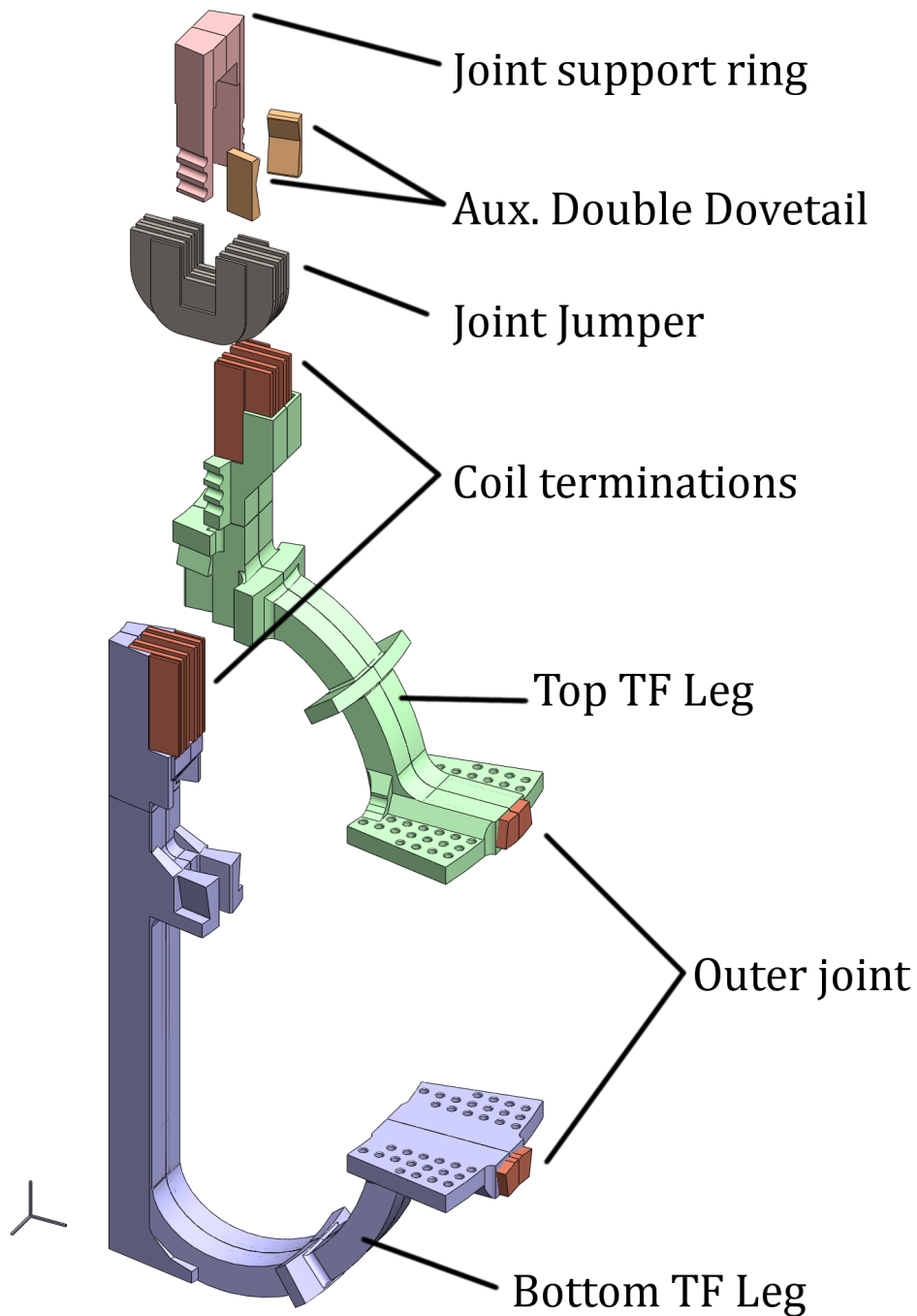


Figure 3-5: Final conceptual design of the TF coils, exploded view. A 22.5° section is shown, corresponding to a single coil, with its parts named. The outer electrical joint and the bolts are not shown for clarity. The number of coil terminations and jumpers are larger than shown in this illustration, but for clarity it was limited to six. The scale in the bottom left is 1 m in each direction.

illustrated in Figure 3-1b.

The outer mid-plane mechanical joint is supported by bolts. The top joint is much more challenging than the other due to the larger magnetic field in that area (the magnetic field is roughly inversely proportional to the radial position) and due to the lower available transverse area. As such, it is the main focus of the design.

The top mechanical joint is supported by a triple dovetail system, as shown in Figures 3-2a and 3-2b. The top leg of the TF coil has a dovetail that fits in a socket in the inner leg of the TF and supports the radial bursting force. The orientation of this dovetail union is such that the top leg is free to slide in and out vertically. An auxiliary part that slides in radially between adjacent coils has an hourglass-shaped double dovetail to support the vertical bursting force. Pins hold the auxiliary double dovetails during operation to prevent them from moving radially outwards.

The electrical joints are composed by the coil terminations and U-shaped jumper plates between them, as shown in Figure 3-3. There are two electrical unions per conductor in each joint area, for a total of 984 electrical unions per coil. The coil terminations are flat, oriented parallel to the plane of the coil. The jumpers slide between two consecutive terminations, and are pressed against the terminations with bladders and pins. The electrical connection in each union is ensured by individual springplates. Further detail on the electrical joint is given in Chapter 4.

In the area of electrical connection the current in the coil termination and in the jumper are opposite. This makes the net magnetic field in that area zero, and the net Lorentz force in the joint area practically null. This allows in the design that the loading of the forces to produce sufficient electrical contact do not change appreciably through coil energization, which is a desired feature for reliability. The coil and jumper terminations can be flexible in the electrical connection area, to allow for the relative displacement of top and bottom legs of the TF coil.

The vertical Lorentz load in the U-shaped jumpers is taken by the joint support ring, a thick steel ring that fits on top of the jumpers. The ring has vertical extensions with pin holes in their ends. The ring is held with pins to the TF coil structure.

The final conceptual design of the TF coils is shown in Figure 3-4. In Figure 3-

5 an exploded view of the TF coil is shown. It must be noted that the design is not optimized; it is a “proof of concept” design, to present the joint concept and to evaluate if the forces can be withstood. Further work will be required to simplify the design, to minimize the number of components and to assure a reliable methodology to assemble and disassemble the joints with remote maintenance tools.

## 3.2 Stress analysis in the coil

To estimate the stress levels in the TF coils during operation, a 3-D finite element analysis was performed using COMSOL, a commercial multiphysics code [60]. The stress simulation was performed in two steps. The first step was to obtain the Lorentz load in the TF coil; for this purpose, magnetic field simulations were performed on the conductors and PF coils only. According to the ARIES-I design [9], the out-of-plane forces in the TF coils are about one order of magnitude smaller than the in-plane forces. The second step was to do the stress simulation of the full coil using the Lorentz force in the conductors as input.

The maximum allowable von Mises stress in the coil structure is defined as 2/3 of the yield stress of the structural material, similar to the ITER criterion [61]. This criterion is consistent with the guidelines by Mott ([62], Chapter 5), of a maximum allowable von Mises stress of 50–80 % the yield stress. For stainless steel 316LN at 7 K the maximum allowable von Mises stress is approximately 750 MPa; at 20 K the maximum allowable stress is expected to be within 2 % of that value, estimated from stainless steel 316 data from [63]. This maximum allowable stress is also lower than 1/2 the ultimate tensile strength of the structural material.

For the magnetic field simulation, the analyzed domain is a toroidal half of the winding pack of a TF coil, and a section of the PF coils and plasma, shown in Figure 3-6. The half-width winding pack was simulated as a multi-turn coil with uniform current density, with a total current of 11.6 MA. Air surrounds the winding pack. The current and location of the PF coils and plasma was taken from [9], with the exception of one coil (PF4,U), which would be superimposed with the top joint of the TF coil

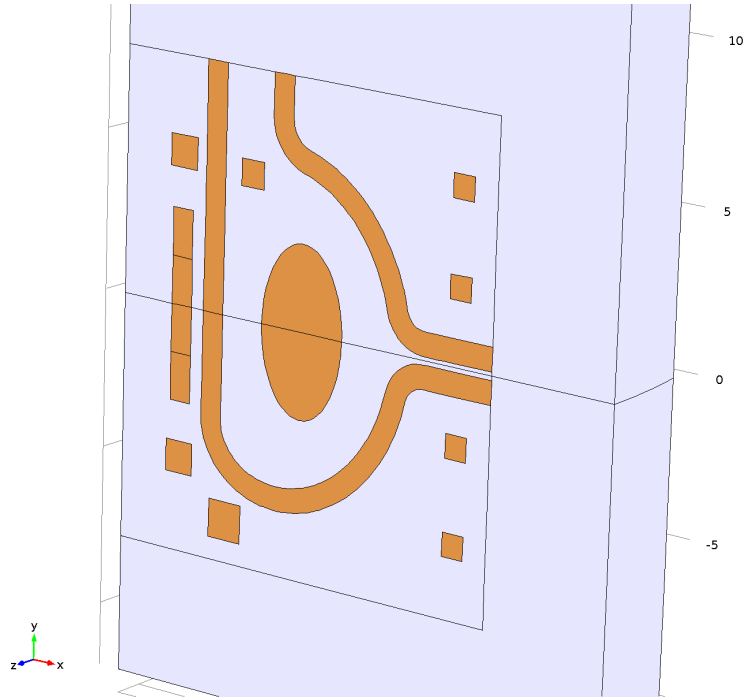


Figure 3-6: Geometry of the magnetic field simulation of half a TF coil. The copper colored parts are the PF and TF coils, the gray part is air.

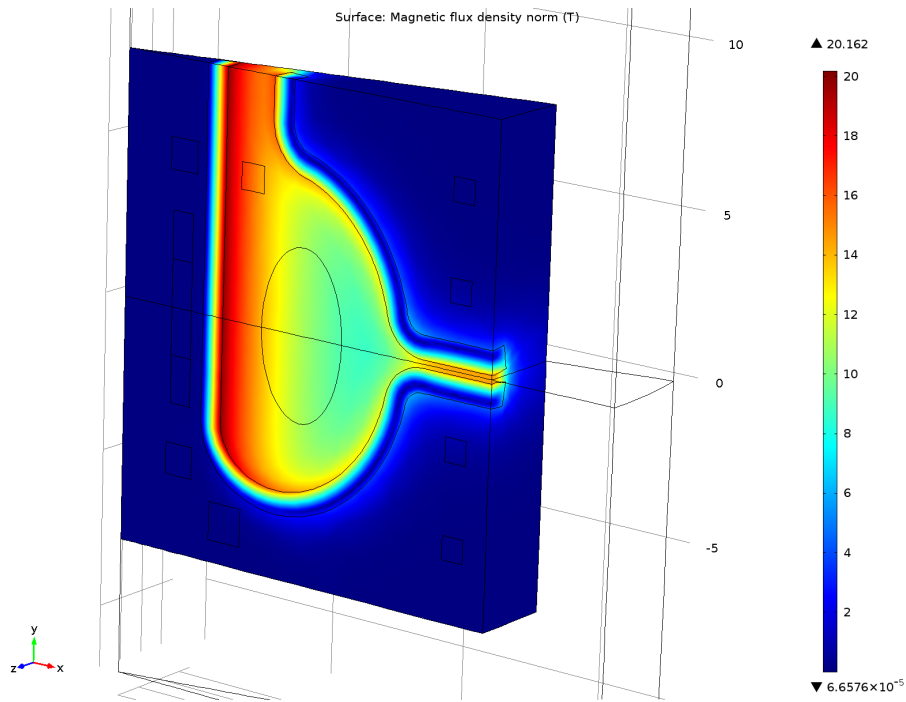


Figure 3-7: Toroidal magnetic field results of the magnetic field simulation of half a TF coil. The largest magnetic field is near 20.2 T, in the inner leg of the TF coil.

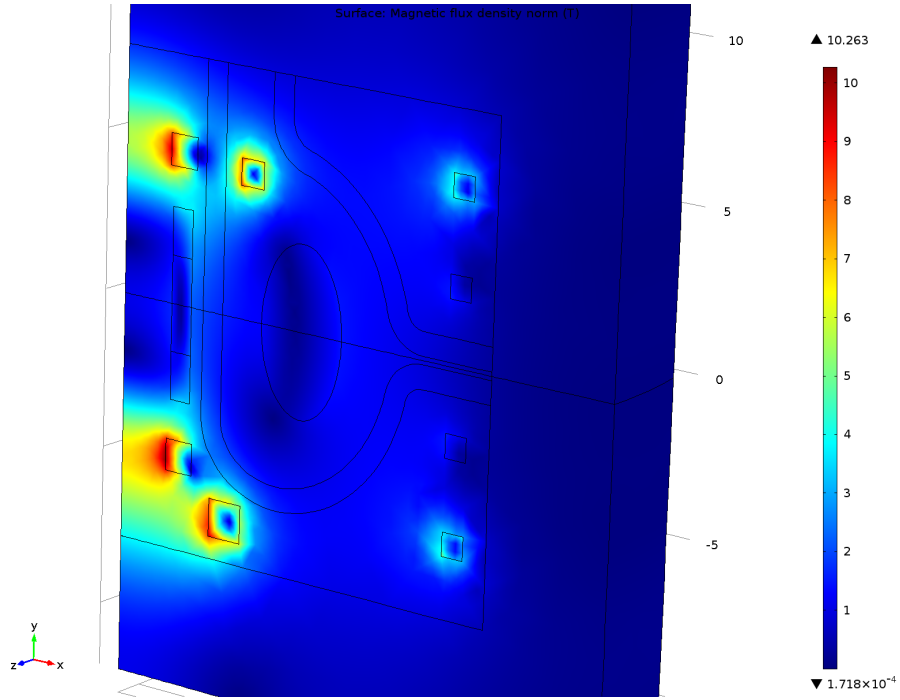


Figure 3-8: Poloidal magnetic field results of the magnetic field simulation of half a TF coil.

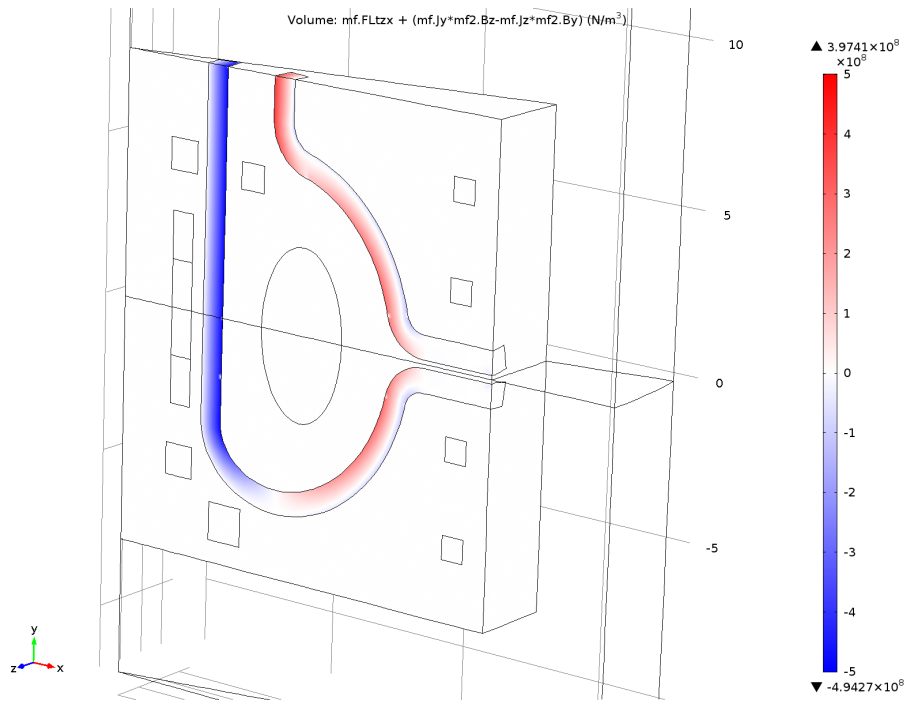


Figure 3-9: Radial component of Lorentz force in the winding pack from magnetic field simulation. The color scale is the same in Figures 3-9, 3-10 and 3-11.

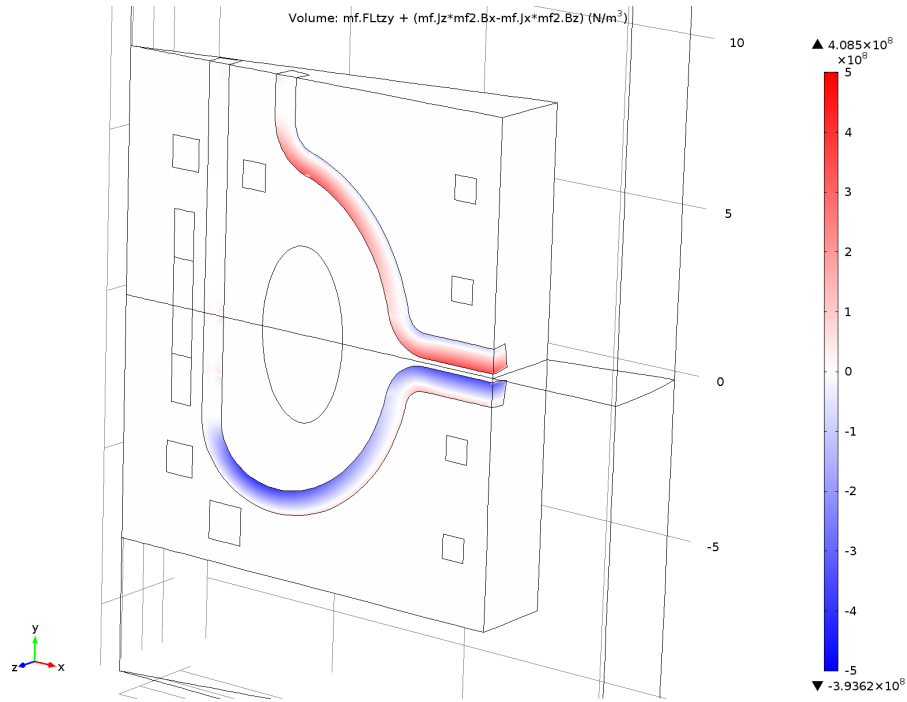


Figure 3-10: Vertical component of Lorentz force in the winding pack from magnetic field simulation. The color scale is the same in Figures 3-9, 3-10 and 3-11.

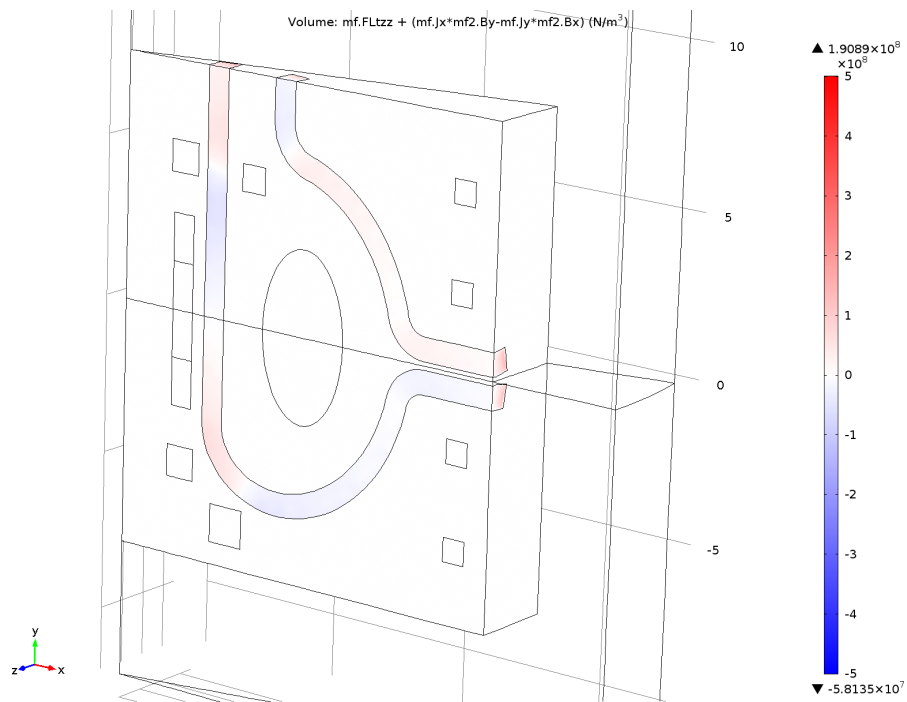
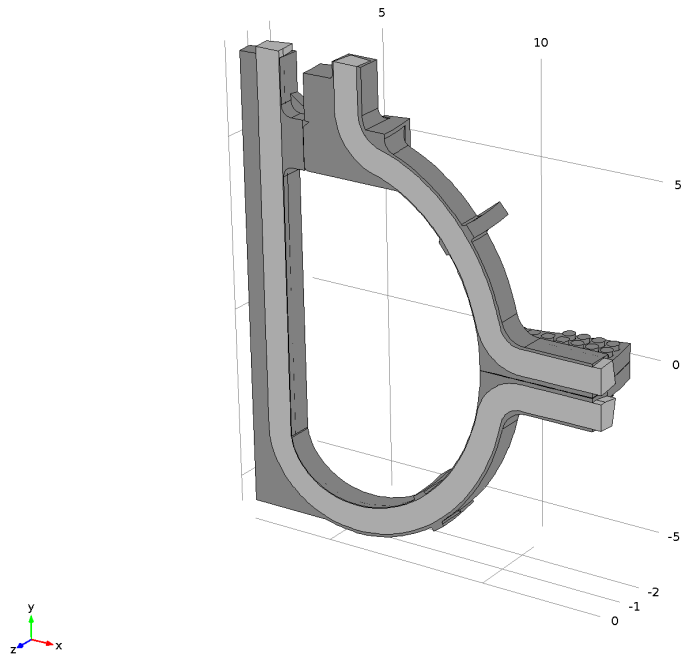
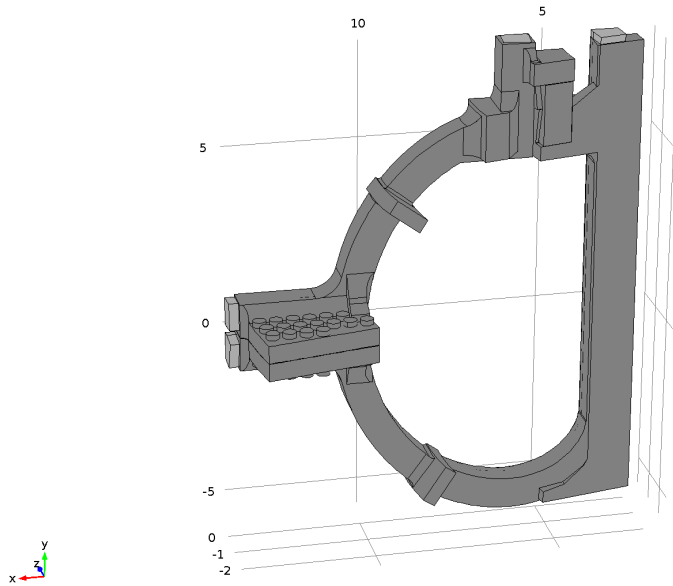


Figure 3-11: Toroidal component of Lorentz force in the winding pack from magnetic field simulation. The color scale is the same in Figures 3-9, 3-10 and 3-11.



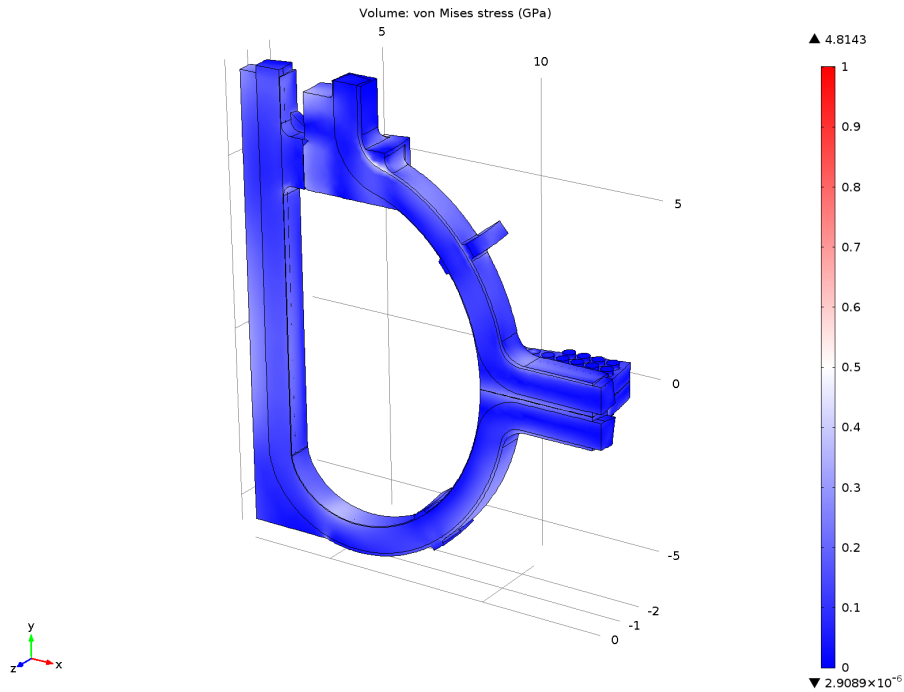
(a) View from coil vertical mid-plane.



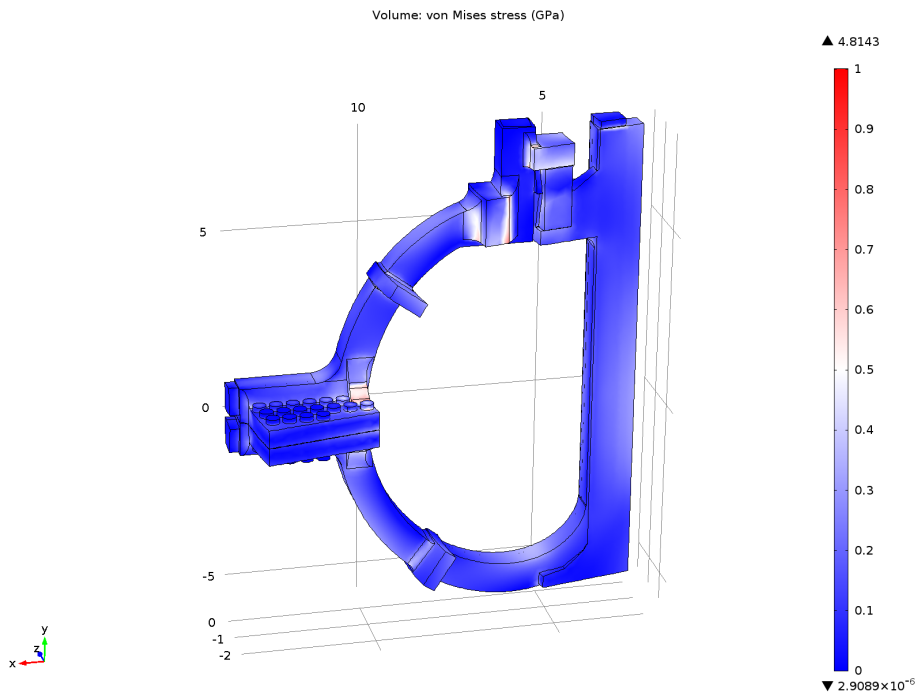
(b) View from inter-coil plane.

Figure 3-12: Geometry of the mechanical stress simulation of half a TF coil. The light gray colored part is the winding pack of the TF coil, the dark gray part is the coil case.





(a) View from coil vertical mid-plane.



(b) View from inter-coil plane.

Figure 3-13: Stress analysis of the TF coils, for 20 T operation. The color scale is the von Mises stress, between 0 and 1 GPa. The stresses in most of the coil case structure are lower than 750 MPa. A few places in the bolts have larger stresses, shown in Figure 3-14.

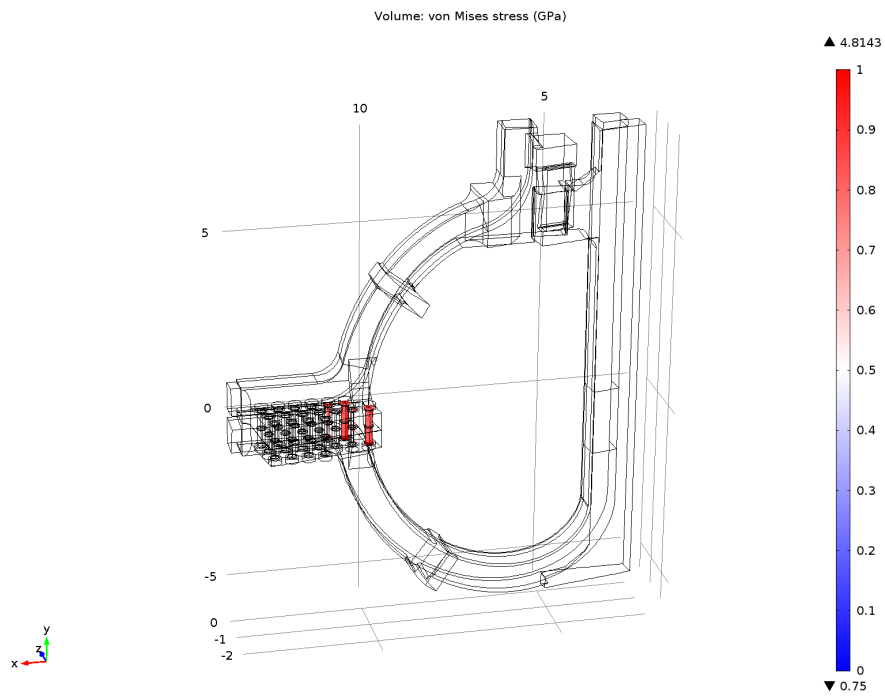


Figure 3-14: Near the top joint.

Figure 3-15: Areas of the TF coils with stresses larger than 750 MPa, for 20 T operation. These areas are only in the bolts in the outer joint. Obtaining an engineering solution to reduce the stresses in these areas is critical.

Table 3.1: PF coils and plasma location and current.

Coil name	Radial position [m]	Vertical position [m]	Current [MA]
PF1,U,L	2.2	$\pm 0.75$	-5.1
PF2,U,L	2.2	$\pm 2.25$	-3.6
PF3,U,L	2.2	$\pm 4.75$	14.6
PF4,U	4.8	4.5	17.4
PF4,L	4.0	-6.40	24.5
PF5,U,L	12.5	$\pm 5.40$	-8.1
PF6,U,L	12.5	$\pm 2.40$	-1.8
Plasma	6.75	0.0	10.2

and moved towards the plasma with its current adjusted accordingly. As this coil is located in a high magnetic field area, it would require REBCO superconductors for operation. In Table 3.1 the characteristics of the PF coils and plasma are summarized. The magnitude of the currents in the PF coils correspond to the “high beta” operation mode of ARIES-I; a more complete analysis of all the operation modes of the PF coils is beyond the scope of this thesis.

To calculate the toroidal magnetic field, the boundary conditions assumed are “perfect magnetic conductor” in the two symmetry planes, which corresponds to forcing the magnetic field to be perpendicular to the surfaces; and “magnetic insulator” in the remaining boundary surfaces, which corresponds to forcing the magnetic field to be parallel to the surfaces. For the poloidal magnetic field calculation, the boundary conditions assumed are “magnetic insulator” in the two symmetry planes, which corresponds to forcing the magnetic field to be parallel to the surfaces, and “perfect magnetic conductor” in the remaining boundary surfaces, which corresponds to forcing the current density parallel to the surfaces. The magnetic field results are shown in Figures 3-7 and 3-8, and the Lorentz load distribution results are shown in Figures 3-9, 3-10 and 3-11. The maximum toroidal magnetic field in the TF coil is 20.2 T, as expected from the ARIES-I data.

For the mechanical stress simulation, the analyzed domain is a toroidal half of a

TF coil, shown in Figures 3-12a and 3-12b. The coil case material is stainless steel 316LN, and the winding pack was simulated as a homogeneous isotropic material with average properties, with an average composition corresponding to layer 1 of the winding pack: 50.2 % steel, 40.7 % copper and 8.0 % superconductor. The properties of these materials are detailed in Tables 2.1 and 2.4. Roller boundary conditions were applied to surfaces in the symmetry planes, and the joint areas were simulated as contact pairs.

The results for the von Mises stress in the coils are shown in Figures 3-13a and 3-13b. Operating at a maximum magnetic field of 20 T, the stresses in the coil structure are acceptable: lower than 500 MPa in the smeared winding pack and lower than 750 MPa in most of the structure. A few minor parts in the outer joint bolts have stresses larger than 750 MPa, as shown in Figure 3-14. Obtaining an engineering solution to reduce these stresses to allowable levels is critical; possible solutions include the use of specialized high strength materials for the bolts or a different joint design with shear pins instead of tension bolts. However the effort required to successfully design these areas with acceptable design is beyond the scope of this thesis.

### **3.3 Stress analysis in the top joint**

The stresses in the top electrical joint of the TF coil were estimated in a similar way to the main section of the TF coils, as described in Section 3.2. A magnetic field simulation was first performed to obtain the Lorentz load in the joint elements, which was used as input for the mechanical stress simulation.

For the magnetic field simulation, the analyzed domain is a toroidal half of the top joint conductors of a TF coil, shown in Figure 3-16. The half-width coil terminations were simulated as two multi-turn coil, with a total current of 11.6 MA each. The three jumpers were simulated as multi-turn coils with the same current density, carrying a total current of 11.6 MA between the three. Air surrounds the terminations and jumper. The boundary conditions assumed are “perfect magnetic

conductor” in the two symmetry planes, which corresponds to forcing the magnetic field to be perpendicular to the surface; and “magnetic insulator” in the remaining boundary surfaces, which corresponds to forcing the magnetic field to be parallel to the surface. The magnetic field results are shown in Figure 3-17, and the Lorentz load distribution results are shown in Figures 3-18a and 3-18b. The maximum magnetic field is 20.1 T, similar to the maximum obtained in Section 3.2.

For the mechanical stress simulation, the analyzed domain is a toroidal half of the top joint of a TF coil, shown in Figures 3-19a and 3-19b. The coil case and support ring material is stainless steel 316LN, and the material of the joint terminations and jumper is the same as the winding pack in Section 3.2. Roller boundary conditions were applied to surfaces in the symmetry planes, and the joint areas were simulated as contact pairs. Additional roller conditions were applied to the wide face of the jumpers to improve the simulation computing time. While this constraint is not completely realistic, in the reactor design, additional pin and bladder mechanisms would lock the jumpers against the coil terminations, as mentioned in Section 3.1. These would apply preload to the conductor faces so that a minimum contact pressure of approximately 100 MPa would be maintained to minimize the joint resistance.

The results for the von Mises stress in the joints are shown in Figures 3-20a and 3-20b. The stresses in the joint are acceptable: lower than 500 MPa in the smeared conductor and jumper, and lower than 750 MPa in most of the structure. A few parts around the pins holding the support ring have stresses larger than 750 MPa, as shown in Figure 3-21. Obtaining an engineering solution to reduce these stresses to allowable levels is critical; possible solutions include the use of specialized high strength materials for the pins and sockets. However the effort required to successfully design these areas with acceptable design is beyond the scope of this thesis.

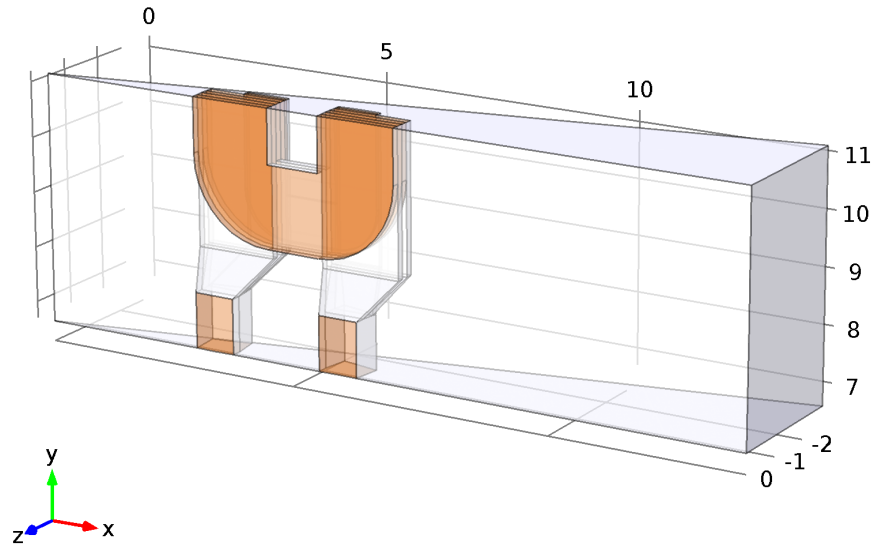


Figure 3-16: Geometry of the magnetic field simulation of half a top TF electric joint. The copper colored parts are the conductors in the joint, the gray part is air.

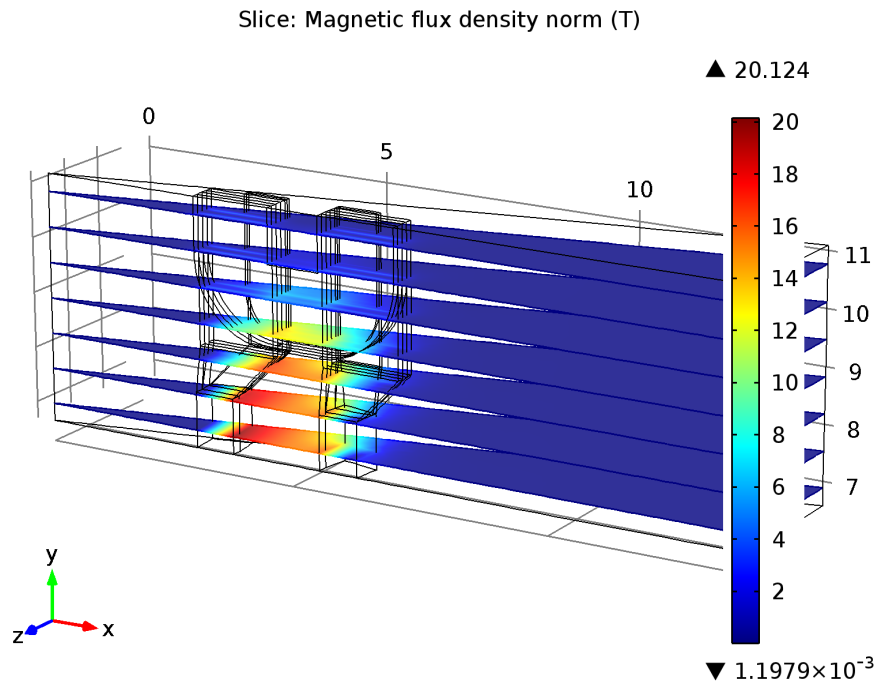
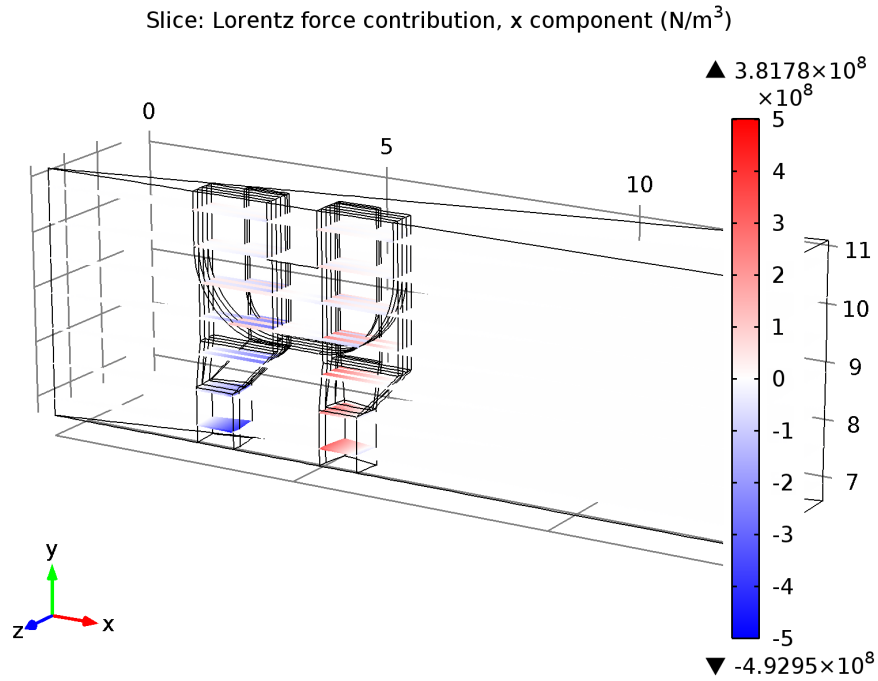
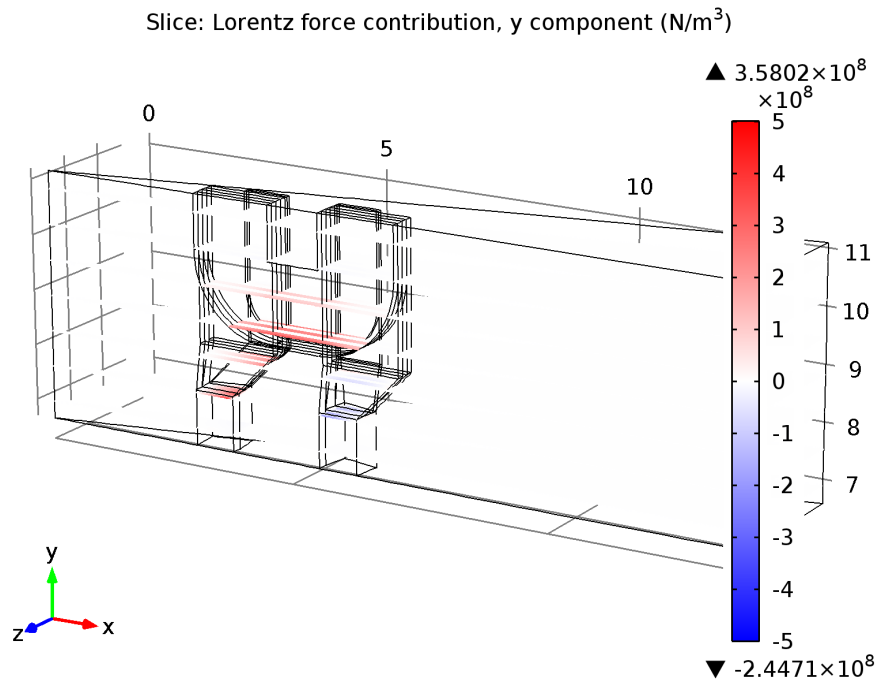


Figure 3-17: Magnetic field results of the magnetic field simulation of half a top TF electric joint. The results are plotted for seven horizontal planes. The largest magnetic field is near 20.1 T, in the inner leg of the TF coil. The magnetic field in the joint area is nearly zero, as expected.

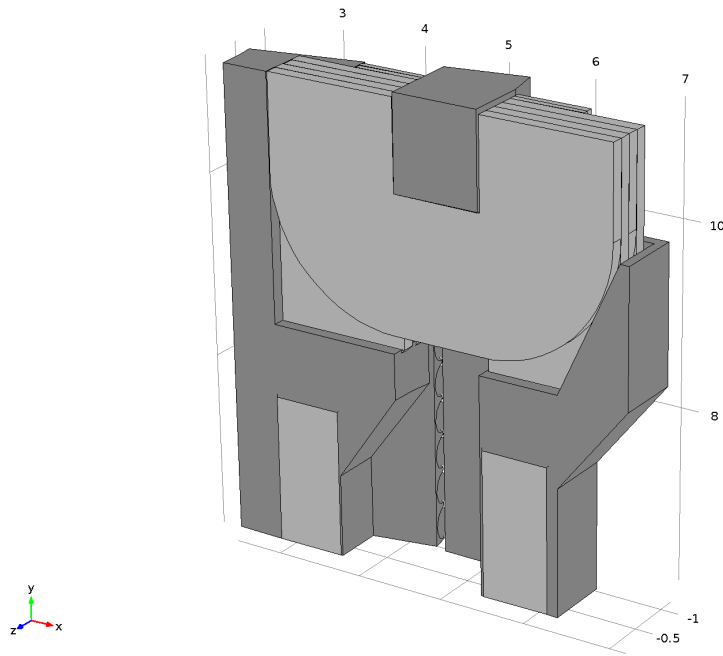


(a) Lorentz force, radial component.

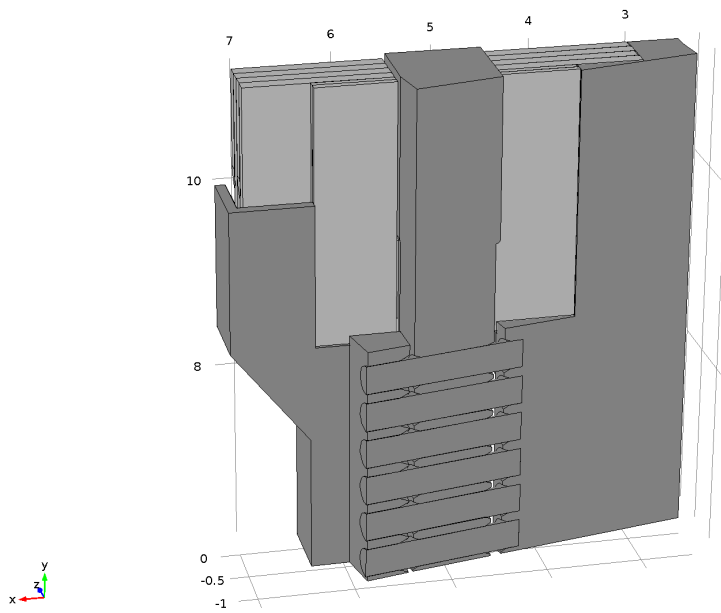


(b) Lorentz force, vertical component.

Figure 3-18: Lorentz force in the joint from magnetic field simulation: (a) radial component, (b) vertical component. The results are plotted for seven horizontal planes. The color scale is the same in both figures. The Lorentz force is nearly zero in the joint area.



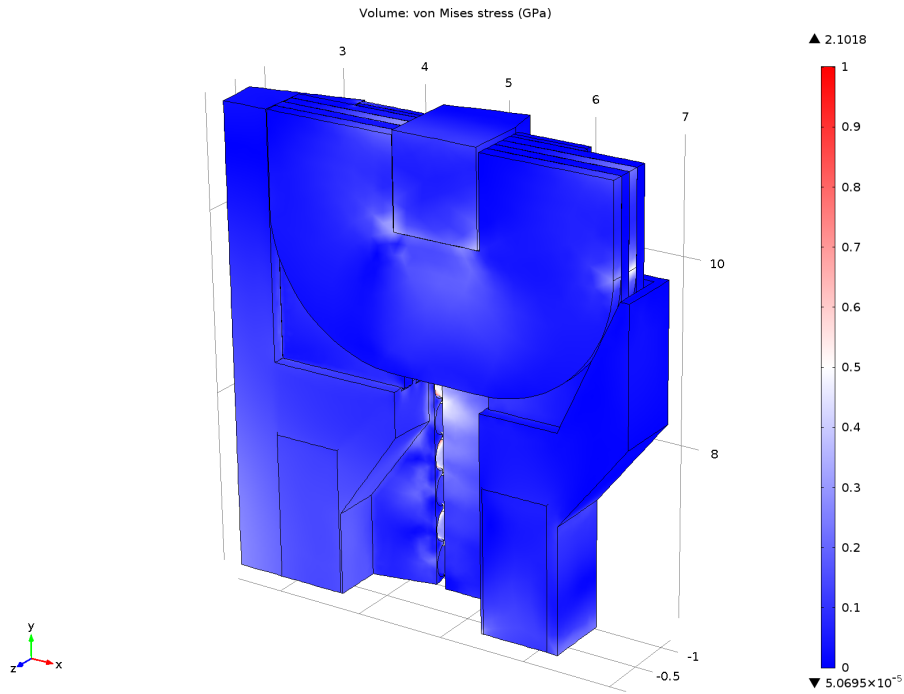
(a) View from coil vertical mid-plane.



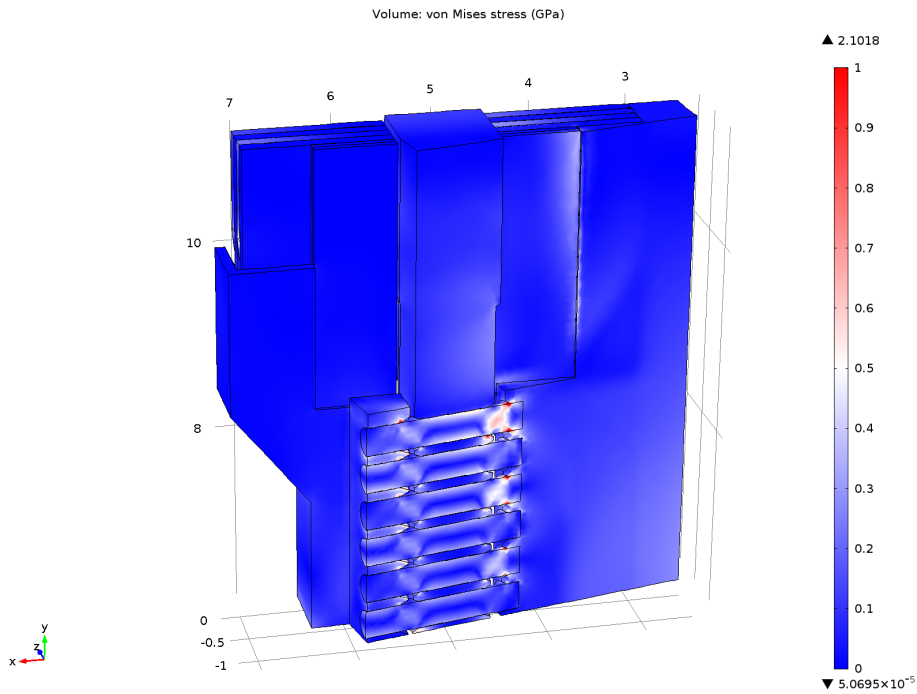
(b) View from inter-coil plane.

Figure 3-19: Geometry of the mechanical stress simulation of half the top joint of a TF coil. The light gray colored part is the winding pack of the TF coil, the dark gray part is the coil case and other structural parts.





(a) View from coil vertical mid-plane.



(b) View from inter-coil plane.

Figure 3-20: Stress analysis of the top TF coil joint, for 20 T operation. The color scale is the von Mises stress, between 0 and 1 GPa. The stresses in most of the structure are lower than 750 MPa. A few places have larger stresses, shown in Figure 3-21.

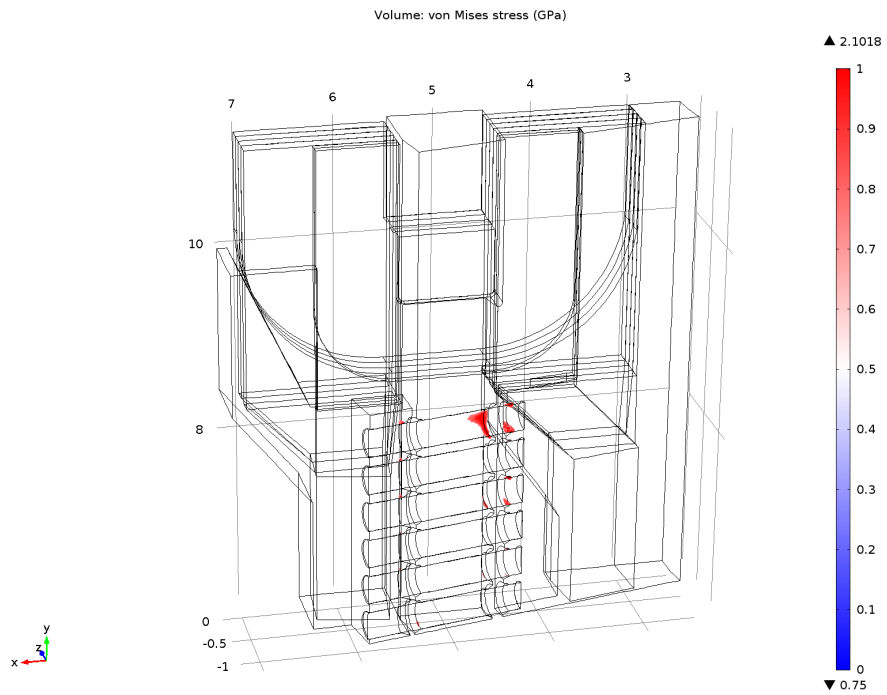


Figure 3-21: Areas of the the top TF coil joint with stresses larger than 750 MPa, for 20 T operation. Obtaining an engineering solution to reduce the stresses in these areas is critical.

# Chapter 4

## Design of the Electrical Joints

The viability of the electrical joints will be assessed considering the ease of construction of the joint parts, ease of joint installation, and the required electrical power to cool and operate the joints.

The ease of construction depends mostly on the joint design. The ease of joint installation is limited by the proposed geometry: planar jumpers that fit between rows of coil terminations; however, the particular joint design geometry may add additional constraints. The target joint resistance is in the order of 10 n $\Omega$  per conductor. As will be detailed in Section 6.1, for such joint resistance the electrical power required to cool the joint and nuclear heating in the entire coil system would be approximately 71 MW.

The target joint resistance is much larger than that of other proposed demountable TF coil designs such as Vulcan [12] and ARC [13], due to the design decision of including a copper layer as contact surface. This copper layer protects the REBCO tapes, eliminating the risk of damaging the superconductors during the installation of the joint, which makes the joint design more reliable.

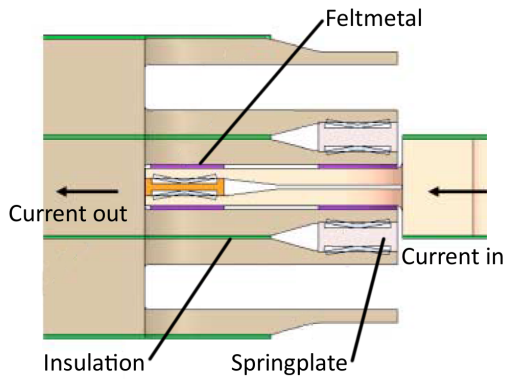
### 4.1 Electrical joint concepts

For joints with REBCO superconductors, the orientation of the REBCO tapes with respect to the joint surface is critical for the joint performance. The substrate in the

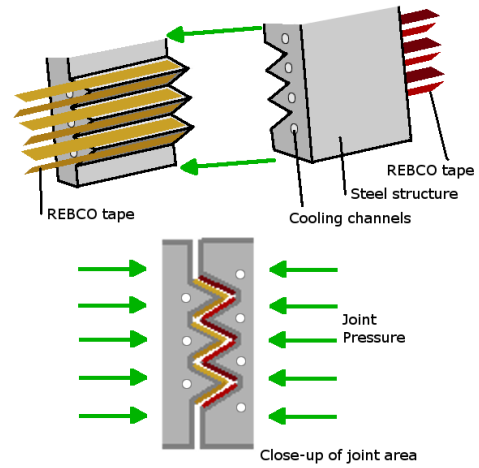
REBCO tapes has a very high resistivity, essentially insulating one of the faces of the tapes. The opposite face has very low resistivity due to the copper coating; current can also flow through the edges of the tape in the thin copper layer. This geometry must be taken into account in the joint design.

In order to choose the best joint concept for the TF coils, several resistive and superconducting electrical joint designs were analyzed. The designs are shown in Figure 4-1, and summarized below.

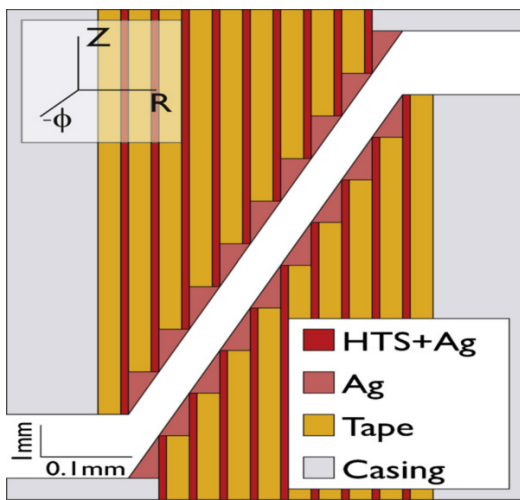
- Sliding joints. This joint concept is used in the copper TF coils of Alcator C-Mod [64]. It is composed by flat copper surfaces pressed with springplates. These joints are easy to mount and are designed to move with respect to each other during operation. They require a sacrificial interface material (copper feltmetal) between the joint surfaces to improve the contact after displacement, at the cost of higher resistance.
- Comb joints. This joint style was developed during the ARC reactor studies [13, 65]. It consists in individual REBCO superconducting tapes mounted on “comb teeth” structures and pressed against each other. It has low resistance due to individual contact of each superconducting tape, however it has very low fabrication tolerances and high risk of damaging the superconductors. Additionally, this design is relatively new and untested.
- Lap/butt joints. Design used in the Vulcan reactor studies [12], consisting on stacks of REBCO tapes arranged in a “staircase” structure and coated with a silver layer to create a single planar mating surface. It has low resistance and space requirements, but the joint design has low fabrication tolerances and high risk of damaging the superconductors.
- Round joint with helical termination tape. Design by Takayasu [7], consisting on stacks of tapes pressed against a cylindrical former. An additional tape is wrapped helically around the former, crossing the tapes in the stack one by one. The assembly is soldered inside a copper tube. This design is relatively easy to



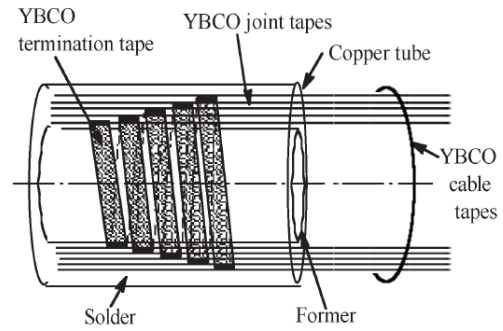
(a) Sliding joint [64]



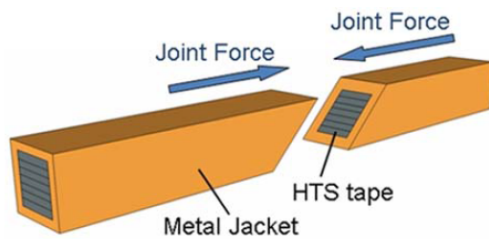
(b) Comb joint [13, 65]



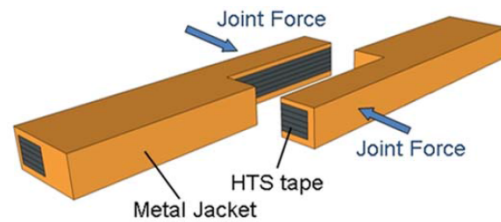
(c) Lap/butt joint [12]



(d) Round joint [7]



(e) Butt joint [6]



(f) Edge joint [6]

Figure 4-1: Joint options considered.

build and is resistant to surface scraping, however it requires a circular instead of a planar contact surface.

- Butt joint. Studied by Ito [6], consists in stacks of REBCO tapes sliced at  $45^\circ$  and pressed together. This concept is similar to the lap/butt joint from Vulcan, only with a much wider angle. This joint design has low resistance and space requirements, at the cost of low fabrication tolerances and higher risk of damage – the slicing process may introduce additional damage to the tapes.
- Edge joint. Studied by Ito [6], it is composed by stacks of REBCO tapes polished and joined on the edges. This option has high tolerances but high damage risk due to the exposed REBCO tape edges.

## 4.2 Potential joint designs

Four joint designs were developed for the demountable TF coils, based on the six designs presented in the previous section. In all cases a thin copper layer is the contact surface. This copper layer protects the REBCO tapes, eliminating the risk of damaging the superconductors during the installation of the joint, at the cost of a higher joint resistance. The designs were qualitatively evaluated with respect of five parameters: ease of construction, ease of installation, REBCO tapes orientation, expected joint resistance and resistance distribution in the joint.

The ease of installation is related to the mounting tolerances of the jumper. In Figure 4-2 the potential displacements and rotations of the jumper during mounting are shown and named for the top joint. The jumper is inserted parallel to the terminations, in the  $Z$  direction. Once it is inserted, it is pressed against the terminations in the  $\Theta$  direction. This mounting scheme has low tolerances to  $\Theta$ -displacements and to  $R\Theta$ - and  $Z\Theta$ -rotations; however, depending on the joint design the tolerances for the other movements may also be low. The outer joint presents similar challenges, with the  $Z$  and  $R$  directions exchanged. In this chapter, only the top joint will be analyzed and assumed to be representative of the outer joints.

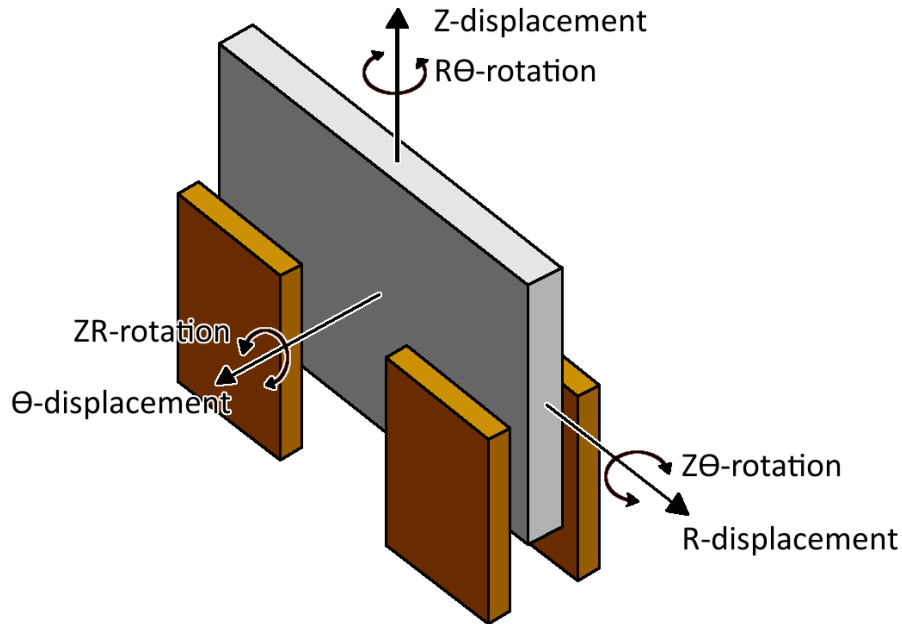
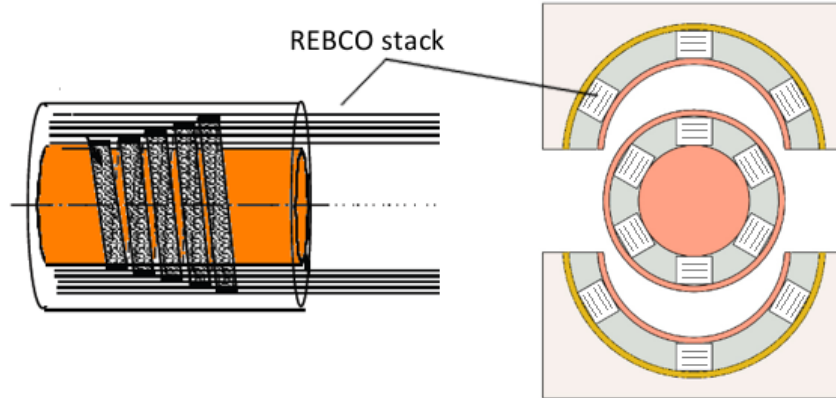


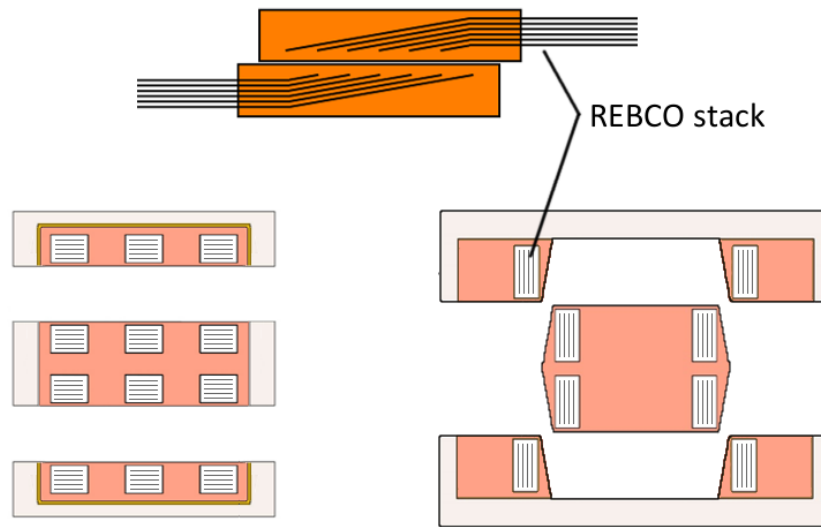
Figure 4-2: Potential displacements and rotations while mounting the top electrical joints. The gray part represents the jumper, the brown parts the coil terminations. For joint mounting, the jumper would move in the  $Z$  direction, with a small movement in the  $\Theta$  direction to make contact at the end. All the other displacements and rotations are unwanted. For the outer joints the  $Z$  and  $R$  directions are exchanged.

The four joint designs are described below. A schematic drawing of their design is shown in Figure 4-3, and a summary of their qualitative evaluation in Table 4.1.

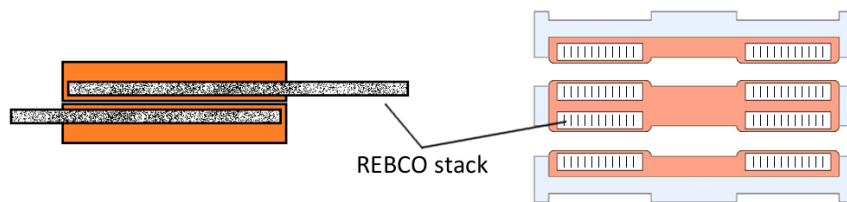
- Round termination and socket (Figure 4-3a): this design is based on the design by Takayasu [7]. It was analyzed at an early stage of the development of the magnet design, at which the six REBCO stacks in the coil were twisted in a round copper core with helical grooves. In the joint area a termination tape is wound around the tapes, making contact to each of them to provide a low resistance current path out of the termination into the joint socket. The tape stacks in the termination are soldered inside a copper tube. In the jumper, the corresponding socket is a concave copper half-tube with three REBCO stacks. Several perpendicular tapes contact the low resistance face of the superconducting tapes in the stacks to provide the electrical low resistance path in a similar way to the termination.



(a) Round termination joint concept. Left: side view. Right: cross section



(b) Flat scarf joint concept. Top: side view. Bottom left: cross section, option #1. Bottom right: cross section, option #2.



(c) Flat edge joint concept. Left: side view. Right: cross section

Figure 4-3: Potential joint designs. Orange components are copper. Light gray components are steel. Dark gray parts are Sn-Pb solder. White parts are REBCO stacks, with the lines representing the orientation of the tapes.



This joint is most difficult to build of the four analyzed, due to the need of weaving a helical tape around the termination tapes. It has very low tolerances to ZR-rotations and R-displacements during installation. The conductors in the termination are twisted. The resistance distribution is expected to be relatively uniform, in the order of 100 n $\Omega$  per tape from Takayasu’s measurements, and the total resistance is expected to be low.

- Flat scarf joint, version #1 (Figure 4-3b, left): this design is similar to the lap/butt joint, but the ends of the tape stack are slightly bent such that the “staircase” structure is parallel to the Z-R plane, as shown in Figure 4-3b. The stacks are soldered in a copper plate with grooves, and an additional copper layer is soldered over the tape stacks to prevent damage to the superconductor.

This joint is relatively easy to build, as the component are simple and do not require special additional tapes. It does not have constraints to ZR-rotations and R-displacements while mounting. The superconductor stack in the termination and in the winding pack is perpendicular to the toroidal magnetic field ( $\Theta$  direction), the orientation with the lowest performance. The total resistance is expected to be low, but the resistance distribution is dependent on the relative exposed area of each tape in the termination and is expected to not uniform.

- Flat scarf joint, version #2 (Figure 4-3b, right): this design is similar to the scarf joint #1, with the superconductor stacks parallel to the  $\Theta$  direction, the orientation with the highest performance. For this conductor orientation, the contact surface is almost perpendicular to the Z-R plane. The resulting socket structure in the jumper is similar to the round termination, with low mounting tolerances to ZR-rotations and R-displacements.

This joint is somewhat harder to build than the scarf joint #1 due to the oblique contact surfaces. The total resistance and resistance distribution is similar to the scarf joint #1.

- Flat edge joint (Figure 4-3c): this design is similar on the edge joint design by

Ito [6]. The superconductor stack is oriented parallel to the toroidal magnetic field, and the edges form the joint area. The stacks are soldered in a copper plate with grooves, and an additional copper layer is soldered over the tape stacks to prevent damage. The contact surface is parallel to the Z-R plane.

This joint is about as easy to build as the scarf joint #1. It presents the orientation advantages of both flat scarf joint options, but without their disadvantages: the superconductor are oriented parallel to the  $\Theta$  direction and the design does not present constraints to ZR-rotations and R-displacements while mounting. The resistance distribution is expected to be even as all tapes will have the same exposed area, however the total resistance may be higher than the other three designs due to the unfavorable geometry of the tape edge.

Table 4.1: Summary of qualitative assessment of the joint designs considered.

Joint concept	Ease of construction	Ease of installation	Conductor orientation	Resistance distribution	Expected resistance
Round	medium	worst	twisted	even	low
Scarf #1	good	good	perp. to $\Theta$	uneven	low
Scarf #2	medium	bad	parallel to $\Theta$	uneven	low
Edge	good	good	parallel to $\Theta$	even	medium

The design chosen is the flat edge joint, as it is the design with the most advantages with the only drawback of higher expected resistance. Such a choice is most appropriate where the recirculating power is not such a constraint. Thus this may be best suited to a Fusion Nuclear Science Facility mission. A more detailed design of the joint components and mounting procedure are given in the next section.

### 4.3 Flat edge joint design characteristics

The conceptual design of the joint is shown in Figure 4-4, to illustrate the mounting system. In a similar fashion to the Alcator C-MOD sliding joints [64], each superconductor stack in the jumper is individually pressed with springplates against the

corresponding stack in the coil termination. The jumper structure is pressed against the coil termination structure with bladders, and kept in place with pins. The bladder pressure and pin tolerances are selected to maintain a minimum surface pressure in the joints after the magnet is cooled down and energized. This design ensures each stack-to-stack connection makes good contact.

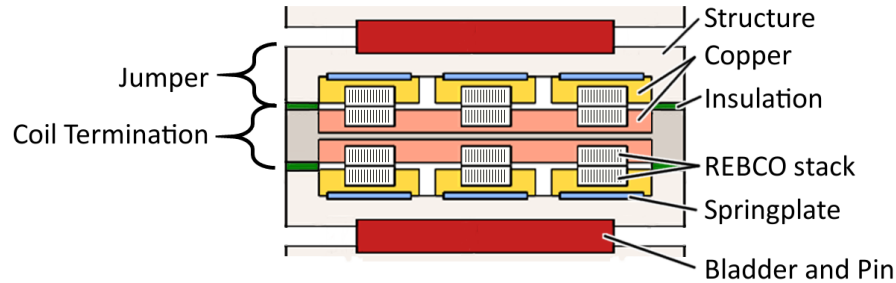
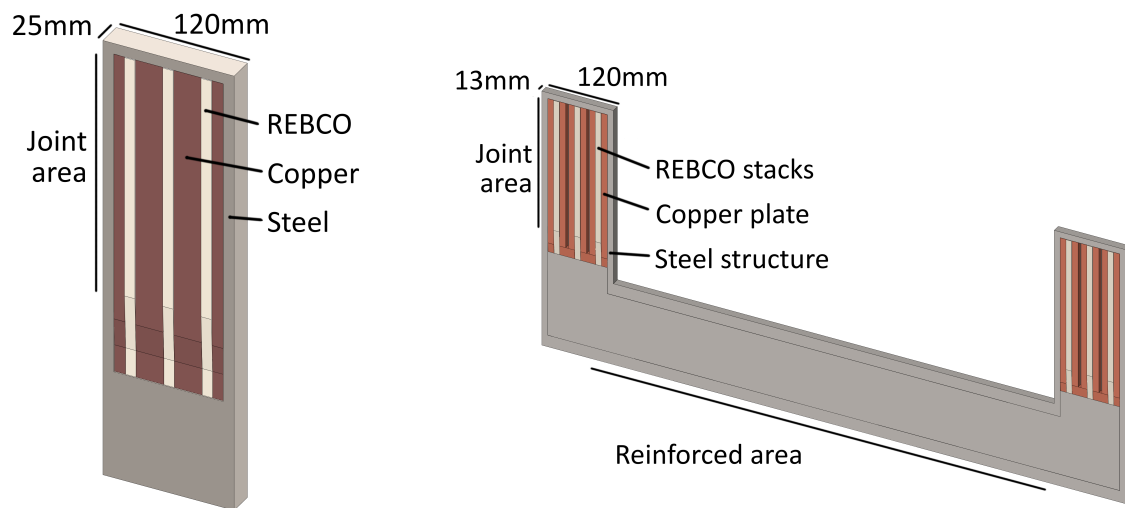


Figure 4-4: Cross section detail of the electrical joint. The superconductor stacks are covered with a copper layer in the contact area. The superconductor tapes are oriented vertically in this drawing and make contact through the edges. Springplates press each joint individually to guarantee good contact.

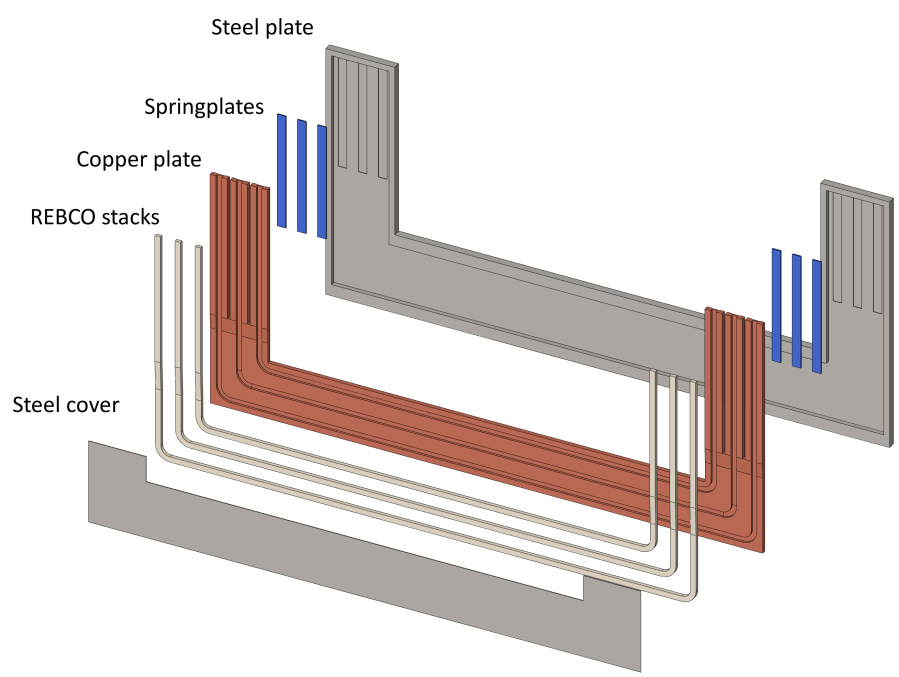
The coil termination design is shown in Figure 4-5a. The termination consists of six REBCO stacks soldered into two copper plates. An I-shaped steel structure holds the copper plates in place. A 1 mm thick copper layer is soldered over the exposed edge of the REBCO stacks for protection. Conservatively, the amount of copper in the termination is the same as in the coil conductor; the required amount of copper is lower than this due to its lower magneto-resistance in this area. The amount of structural steel required is much lower than in the coil due to the negligible Lorentz force.

Two jumpers are required for each coil termination pair. The jumper design is shown in Figure 4-5b, and an exploded view is shown in Figure 4-5c. It is composed of three REBCO stacks soldered on a U-shaped copper plate. The copper plate is mounted on a steel support plate and is slotted near the ends, to make three independently moving termination areas. Springplates are mounted between the steel and copper plates near the ends. A 1 mm thick copper layer is soldered over the exposed edge of the REBCO stacks for protection. The amount of copper in the



(a) Coil termination

(b) Jumper



(c) Exploded view of jumper

Figure 4-5: Coil termination and jumper design.

jumper is the same as in the termination. The amount of steel in the connection area is the same as in the termination; the rest of the jumper is reinforced to support the Lorentz force.

The size of the termination is not optimized, only roughly estimated to evaluate the required joint space. Each conductor termination is 120 mm wide in the R direction and 25 mm wide in the  $\Theta$  direction. The size of the jumper in the connection area is 120 mm by 13 mm. The terminations are supported in the R direction against other terminations, and are 35 mm separated from the adjacent terminations in the  $\Theta$  direction. The length of the joint is calculated to achieve the 10 n $\Omega$  joint resistance, as estimated from our experimental data in Section 5.4. The local cooling channels for both the jumper and the termination are located in the copper plates, and are described in Section 6.1.2.

The mounting procedure of the joint is illustrated in Figure 4-6. Two adjacent jumpers are inserted together “back to back” between two rows of coil terminations (Figure 4-6a). This way, there is a 4–5 mm gap between the jumpers and each row of terminations. Once the jumpers are roughly at the correct Z position (Figure 4-6b), they are aligned in the R and Z direction with a precision mechanism (Figure 4-6c). Then the jumpers are separated and positioned against the terminations in the  $\Theta$  direction (Figure 4-6d).

After all the jumpers are in position as described, the bladders are pressurized to press the jumpers against the terminations (Figure 4-6e). Pins are then inserted between the jumpers to maintain the pressure during cooldown and operation (Figure 4-6f), and the bladders are deflated and removed (Figure 4-6g).

Lastly, the joint support ring is lowered in place and it is bolted to the TF coil structure.

## 4.4 Electrical Joint Insulation

Insulation in the winding pack and in the joint is required to protect the conductors from electric damage during high voltage events, such as during a quench. The

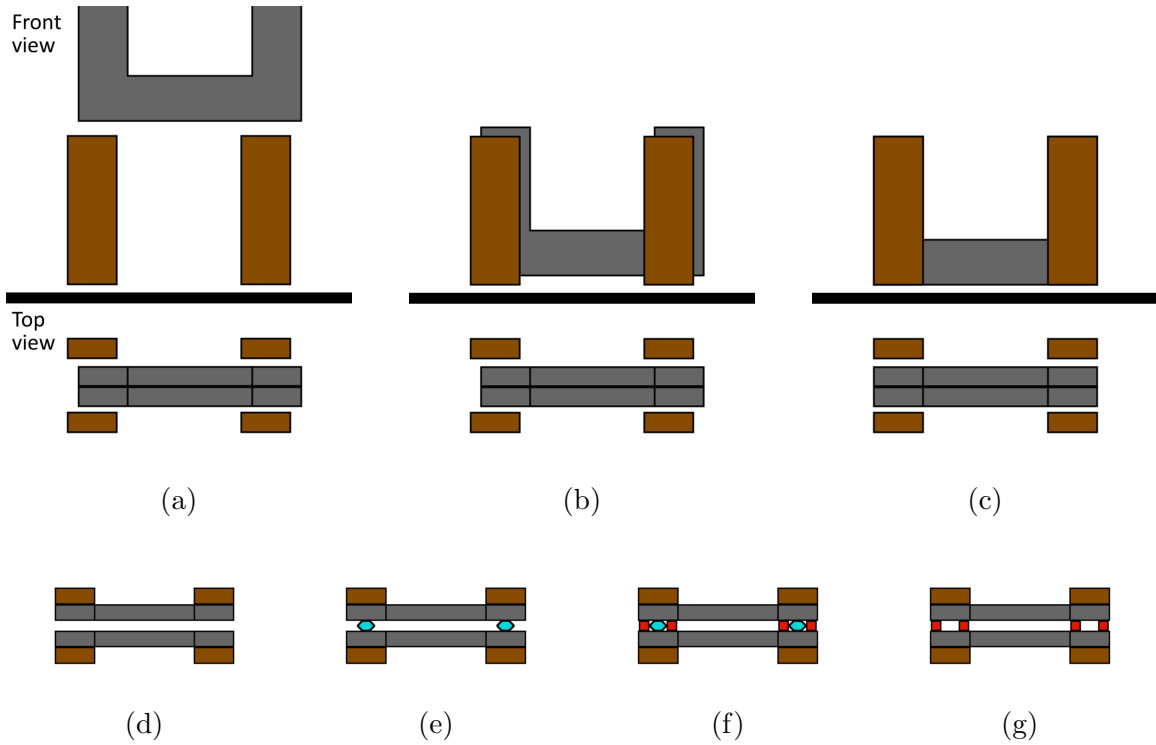


Figure 4-6: Joint mounting procedure. The gray component represents the jumper, the brown components are the coil terminations. The blue hexagons represent the bladders. The red components represent the pins.

insulation in the winding pack is inspired by the KSTAR design, as described by Chung [66, 67]. In the joint region the insulation design is more challenging, because it cannot be one continuous piece as in the winding pack.

The insulation is divided into three parts, each addressing a different electrical risk, and are summarized below. A schematic drawing of the insulation in the winding pack, coil terminations and jumpers are shown in Figures 4-7, 4-8 and 4-9 respectively.

- Insulation between adjacent conductors: the voltage between two adjacent conductors is proportional to the number of turns between the conductors. The maximum number of turns between two adjacent conductors is twice the number of layers (26); the maximum such voltage is  $V_{CC}$ .

The conductor insulation surrounds each individual conductor in the winding pack and in the coil terminations. In the jumper, this insulation is located between the copper plates and the steel plate. The insulation is similar to the

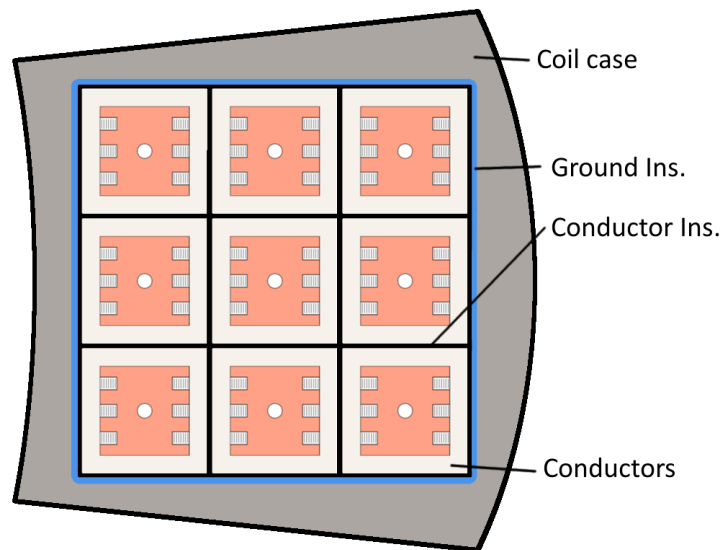


Figure 4-7: Schematic drawing of the insulation in the coil winding pack. The insulation material is Kapton and S2-glass tapes and epoxy resin. The maximum voltage is 640 V between conductors, and 6.1 kV to ground. The conductor insulation is 0.4 mm thick, the ground insulation is 2.5 mm thick.

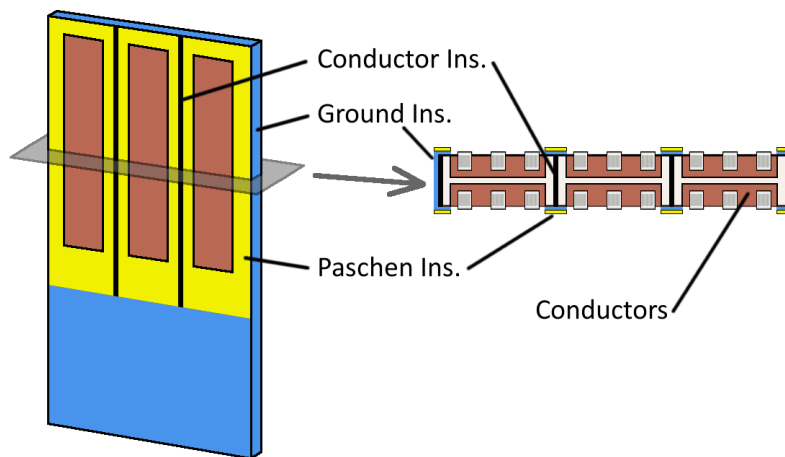


Figure 4-8: Schematic drawing of the insulation near the coil terminations. The insulation material is Kapton and S2-glass tapes and epoxy resin for the ground and conductor insulation, and Torlon for the Paschen insulation. The ground insulation covers all exposed surfaces of the termination. The conductor insulation is wrapped around the structure of each individual termination. The area around the electrical connection is sealed with the Paschen insulation. The maximum voltage is 640 V between conductors, and 6.1 kV to ground. The conductor insulation is 0.3 mm thick, the ground insulation is 2.5 mm thick.

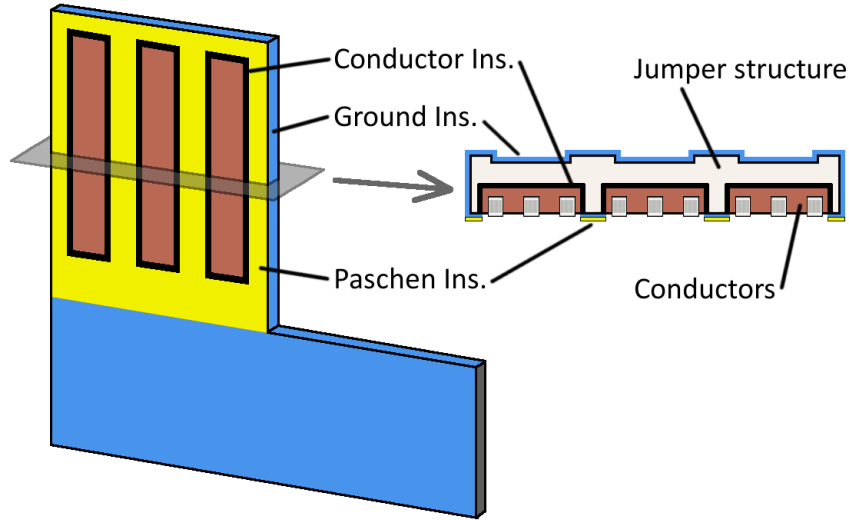


Figure 4-9: Schematic drawing of the insulation in the jumper. The insulation material is Kapton and S2-glass tapes and epoxy resin for the ground and conductor insulation, and Torlon for the Paschen insulation. The ground insulation covers all exposed surfaces of the jumper. The conductor insulation is located between the conductors and the steel plate. The area around the electrical connection is sealed with the Paschen insulation. The maximum voltage is 640 V between conductors, and 6.1 kV to ground. The conductor insulation is 0.3 mm thick, the ground insulation is 2.5 mm thick

KSTAR design [66], using Kapton and S2-glass tapes and epoxy resin.

- Insulation to ground: assuming one of the current leads of the TF coils is grounded, the voltage from any conductor to ground is proportional to the number of turns between the conductor and the current lead. The maximum voltage to ground ( $V_{CG}$ ) would occur in the opposite current lead.

The ground insulation surrounds the winding pack in the coil, and covers the areas exposed to the grounded elements in the joint, such as the ends of the coil case and the structural part of the jumpers. As in the KSTAR design, the ground insulation is epoxy impregnated S2-glass tapes.

- Insulation against Paschen breakdown: Paschen breakdown happens between two conductor surfaces exposed to gas. At any gas pressure, there is a distance between the surfaces such that the breakdown voltage is minimum. For gaseous



hydrogen at 85 K this minimum voltage ( $V_{Pa}$ ) is approximately 275 V [68].

To prevent electric arcs all the exposed conducting surfaces are insulated. The ground insulation fulfills this function in most of the coil and jumper. In the joint areas, the surface around the electrical connection is sealed with an additional overlapping compliant insulation of Torlon (a polyamide-imide) in the jumper.

The maximum voltage in a TF coil in a quench ( $V_Q$ ) event is the maximum voltage to ground  $V_{CG}$ . It is calculated in Section 2.2, and its value is presented in Table 2.2: 6.1 kV

Keeping the maximum voltage 10 times lower than the breakdown voltage of insulation, the voltage per thickness for epoxy impregnated S-glass insulation is 2.5 kV/mm [67]. The required ground insulation thickness is at least 2.5 mm. Since  $V_{CG}$  is much larger than  $V_{Pa}$ , this insulation is enough to protect against Paschen discharges in the areas where it is applied.

The ratio of maximum voltage between two conductors  $V_{CC}$  to maximum voltage to ground  $V_{CG}$  is equal to the ratio of the number of turns for each case (26 turns for adjacent conductors, 246 turns in the entire TF coil).  $V_{CC}$  can be calculated as:

$$V_{CC} = \frac{26}{246} V_{CG} = 640 \text{ V} \quad (4.1)$$

The turn-to-turn insulation has Kapton tape in addition to S2-glass tape. The design voltage per thickness for this insulation is higher, because Kapton has a higher breakdown voltage. Conservatively, using the same value (2.5 kV/mm) as in the ground insulation, the required conductor insulation is 0.3 mm.

Although information about the tracking strength of these insulation materials at 20 K in low pressure hydrogen gas is not available, tracking breakdown along the insulation surface is not expected to be of concern. According to Haarman [69], the tracking strength of several insulation materials (Mylar, paper phenolic, polyethylene and Nylon) at 4 K and in 0.9 atm gaseous helium is close to 4 kV/cm. The typical distance between two conductors is at least 2 cm, yielding a tracking voltage of 8 kV,

which is approximately 9 times higher than the maximum expected voltage between conductors  $V_{CC}$ .

# Chapter 5

## Experimental characterization of Electrical Joints

A set of small scale experiments was performed in order to characterize the proposed electrical joints. The joint samples configuration is similar to the electrical joint described in Chapter 4. Each sample consists of a stack of 80 SuperPower REBCO tapes (model SCS4050-AP), a copper sample holder and a copper cover layer, as shown in Figure 5-1. The REBCO tapes are 200 mm long, 4 mm wide and 0.1 mm thick. The copper sample holder is 76 mm long, 25 mm wide and 6.3 mm thick, with a machined 4.5 mm deep, 8 mm wide slot in one of the wide faces. The REBCO stack fits tightly in this slot, oriented such that the tapes have one of their edges exposed. The copper cover layer is 76 mm long, 9.5 mm wide and 1 mm thick, machined such that fits tightly on top of the REBCO stack in the copper sample holder slot. The assembled joint sample was soldered with SnPb 60/40 solder. A picture of both soldered joint samples is shown in Figure 5-2. The contact surface of the joint is the surface of the copper cover layer, and the nominal contact area is approximately 725 mm<sup>2</sup>. To improve the electrical contact of the joints and reduce the surface oxidation, the contact surface of the samples were coated with a thin layer of silver.

Three contact conditions were considered, depending on the material added between the two joint samples to improve contact:



Figure 5-1: Components of the electrical joint sample.

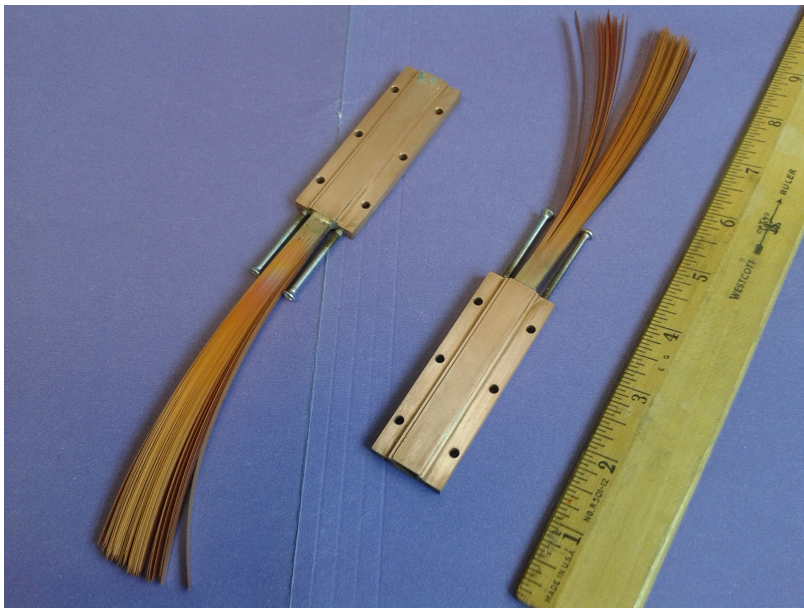


Figure 5-2: Joint samples soldered.

- Feltmetal: a piece of copper feltmetal added between the joints, approximately 0.8 mm thick. The feltmetal is composed by short lengths of 50  $\mu\text{m}$  diameter copper wires randomly dispersed on a copper sheet, bonded by sintering. It is electroplated with silver (approximately 25  $\mu\text{m}$  thick) to improve the electrical contact and minimize oxidation.
- Indium: a 0.05 mm thick Indium film added between the joints, 99.995 % purity.
- Bare: no material added between the joints.

The real contact area between the two joint samples was estimated at room temperature for each of the three conditions described. The procedure and results are discussed in Section 5.1.

To investigate the resistance distribution in the joint, a first experiment was done flowing current up to 100 A through a single REBCO tape in each joint, with the joint pair under compression. This was repeated for several single tape pairs, and for different applied pressures between 10 and 70 MPa. All measurements were performed at 77 K in boiling liquid nitrogen. Further details of this experiment are presented in Section 5.2.

To estimate the total joint resistance, a second experiment was done flowing current up to 3 kA through all the REBCO tapes in each joint, with the joint pair under compression, also at 77 K. This was repeated for several applied pressures between 10 and 35 MPa. Further detail of this experiment is presented in Section 5.3.

## 5.1 Pressure distribution on the contact surface

To estimate the real contact area between the two samples for each of the contact conditions, the joint set was compressed at room temperature with a pressure measurement film between the samples. For this purpose, an Instron 8501 testing machine was used. The applied compressive force was 14.5 kN, which corresponds to an average pressure (calculated as applied force divided by nominal contact area) of 20 MPa.

The pressure measurement film utilized was a Fujifilm Prescale MS, with a pressure range of 10–50 MPa.

The test results are presented in Table 5.1, with the conditions noted and the estimated contact area fraction with respect to the nominal contact area. In the film pictures, dark pink color corresponds to 50 MPa or more, the background color corresponds to 10 MPa or less, and the shades of pink in between correspond to 10–50 MPa. The estimated contact area fraction was calculated as the number of darker pixels in the image divided by the total number of pixels in the nominal contact area.






The first two tests were performed without modifying the samples after soldering, test #1 was in bare condition and test #2 was with Indium. The estimated contact area in both cases are similar, however relatively low (approximately 22 %). The contact surface of both joint samples were polished after this, with 30 and 9  $\mu\text{m}$  polish papers, and tested again in bare condition (test #3), achieving the same contact area. For test #4 the joint samples were mounted with an additional 25 mm thick steel block pair below and above them, between the Instron machine terminals, to increase the stiffness of the setup. The results in bare condition are better, with a 30 % contact area fraction. Lastly, test #5 was done using the same setup as test #4 but with feltmetal, achieving approximately 32 % contact area. Qualitatively, the contact area with Indium and in bare condition is the same, concentrated near the ends of the joint contact surface. With feltmetal, contact area is spread out evenly throughout the entire surface, but nevertheless, the total contact area is similar to the bare surface result.

## **5.2 Single tapes experiment and joint resistance distribution**

### **5.2.1 Experimental setup and procedure**

To analyze the resistance distribution in the joint, access to the individual tapes in each joint sample was required. 3 mm copper square rods were soldered to the end

Table 5.1: Pressure distribution results

Test #	Film picture	Condition	Contact area fraction
1		Bare	22 %
2		Indium	23 %
3		Bare	22 %
4		Bare	30 %
5		Feltmetal	32 %

of several tapes in each joint to be used as current leads. The soldered length for the current leads was 15–20 mm. Insulated wires were soldered in the middle section of these tapes to act as voltage taps, separated at least 20 mm from the current lead and the copper sample holder. The samples, current leads and voltage taps were supported by a plywood board.

The tests were performed in the same Instron 8501 testing machine mentioned in Section 5.1. Two 25 mm thick steel blocks were used to support the sample and to improve the stiffness of the testing apparatus. Two 25 mm thick G10 blocks were used to insulate the Instron terminals from the samples and steel blocks, both electrically and thermally. An aluminum box was used as liquid nitrogen tank, held between the bottom G10 block and the bottom steel block. The box was insulated on the four sides and bottom with expanded polystyrene and plywood, except for a 150 mm circular hole in the bottom to provide access to the Instron terminals. The top terminal of the Instron machine has a ball joint to ensure the face of both terminals are parallel to the joint samples. The experimental setup is shown in Figure 5-3. The power supply utilized was a 100 A, 10 V current supply.

Prior to every test set, the joints contact surfaces were lightly brushed with very

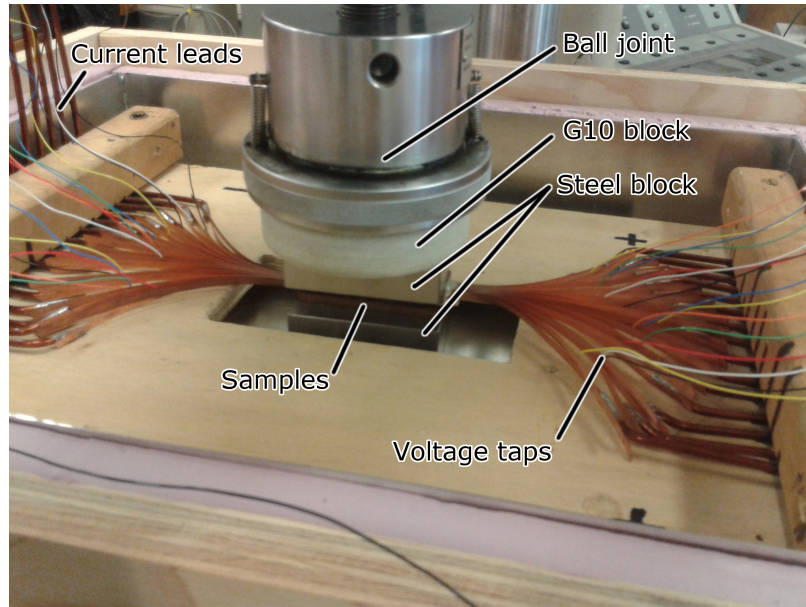


Figure 5-3: Experiment setup for single tapes resistance measurement. The joint pair is pressed with an Instron machine.

fine grade 3M Scotch-Brite, then cleaned with acetone and finally with alcohol. Depending on the condition of the test, additional material was added between the joint samples. Then the set up was assembled as described in the previous paragraph, and a small load (0.7 MPa) was applied to the joint to keep the joint sample aligned and to adjust parallel the top terminal of the Instron machine. Liquid nitrogen was poured into the liquid nitrogen tank until its level was 20 mm above the superconductors; the liquid level was kept at least at that level throughout the experiment.

To measure the resistance of the joint, one superconductor of each side was selected and current was flown through them. Two Keithley 34420A nanovoltmeters were used: one to measure the voltage difference between the taps corresponding to the superconductors chosen, and the other to measure the voltage drop across a calibrated shunt connected in series to calculate the applied current. These voltage vs applied current measurements were performed up to 100A, for four pairs of superconductors at different pressures.



## 5.2.2 Single tapes results

The superconductors in both joints were numbered 1–80, such that once the joint is assembled the superconductors with the same number are roughly aligned. The four pairs of tapes chosen to evaluate the resistance distribution are tapes #4, #26, #69 and #79. Additionally, a few selected measurements were made with non-aligned tapes, using tape #4 from the positive joint terminal and tape #79 from the negative joint terminal.

At each pressure, the voltage vs. current dependence is linear, with similar slope across the different pairs. The slope is the tape-to-tape resistance. An example is shown in Figure 5-4, where the voltage-current measurements for two of the aligned tape pairs and the non-aligned pair is shown.

The joint resistance vs. applied pressure results are shown in Figures 5-5, 5-6, 5-7 for experiments with feltmetal, with Indium and in bare condition, respectively. The arrows represent the chronological order in which the measurements were made: the first five measurements were performed increasing pressure (from 10 to 70 MPa), then the pressure was reduced to 29 MPa, and at last the pressure was reduced to 1 MPa and increased to 29 MPa again.

The feltmetal results show resistance increase after a pressure cycle. This is probably caused by the plastic deformation of feltmetal. The measured resistance with Indium film is much lower than with feltmetal, and the Indium film joints present good memory after cycling. The resistance in bare condition is slightly lower than the resistance with Indium, and it does not present any cycling memory. The resistance at 69 MPa is 0.84–0.90  $\mu\Omega$  for feltmetal, 0.54–0.63  $\mu\Omega$  for Indium, and 0.45–0.49  $\mu\Omega$  for bare condition.

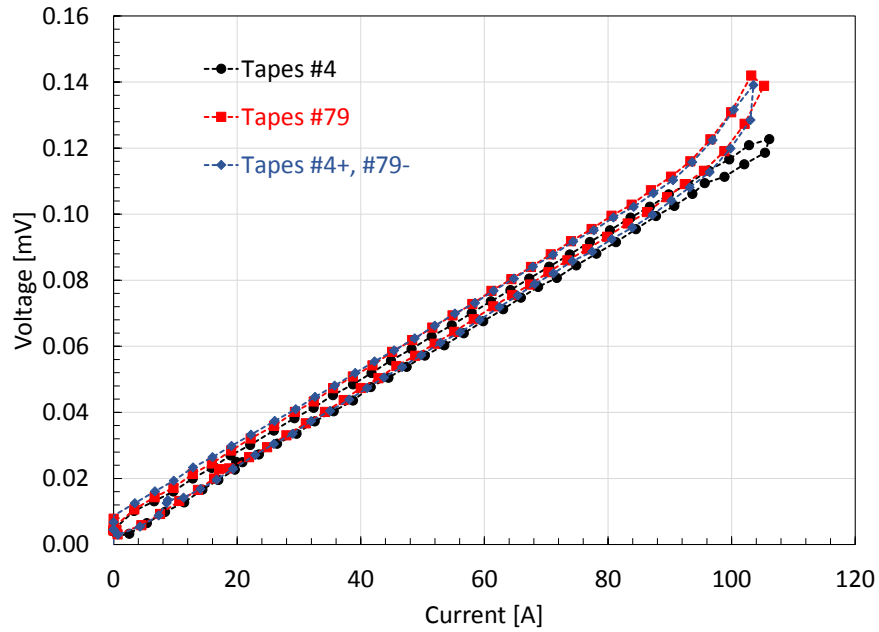


Figure 5-4: Voltage vs. current measurement for the single tapes test with feltmetal. The applied pressure was 29 MPa. The resistance is the slope of the curve. The data points correspond to two aligned tape pairs and the non-aligned pair.

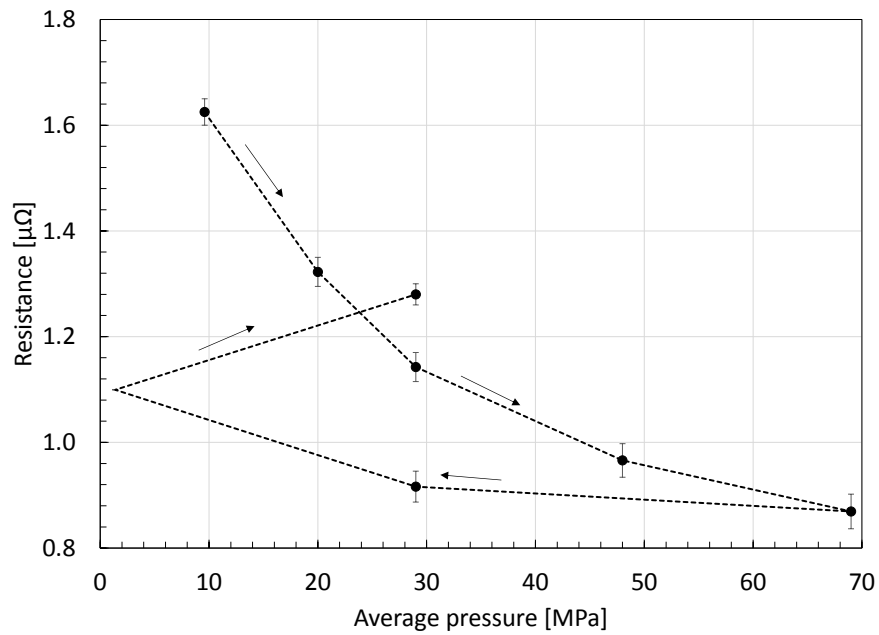


Figure 5-5: Tape-to-tape resistance vs. applied pressure for the joint with felt-metal. The arrows indicate the chronological order of the measurements.

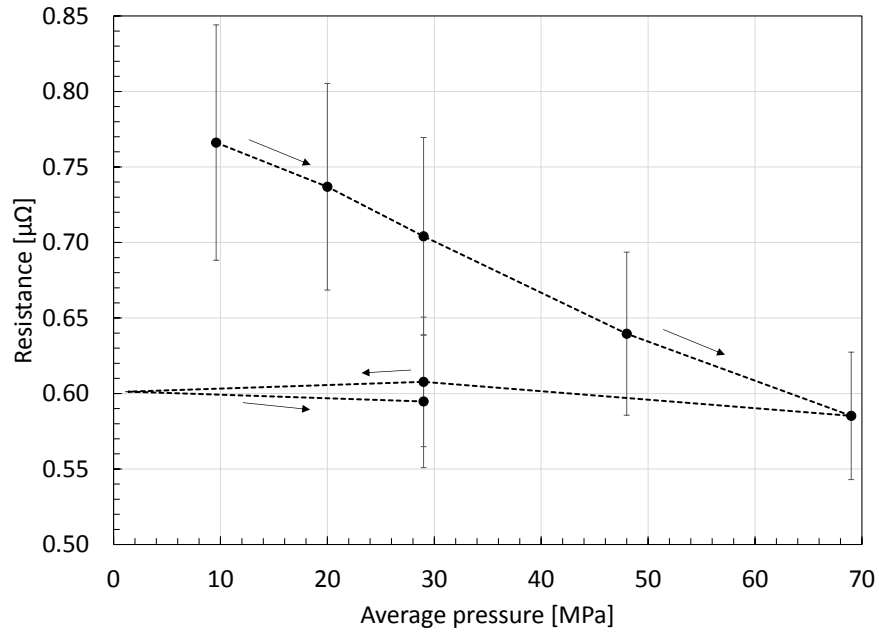


Figure 5-6: Tape-to-tape resistance vs. applied pressure for the joint with  $50\mu m$  Indium film. The arrows indicate the chronological order of the measurements.

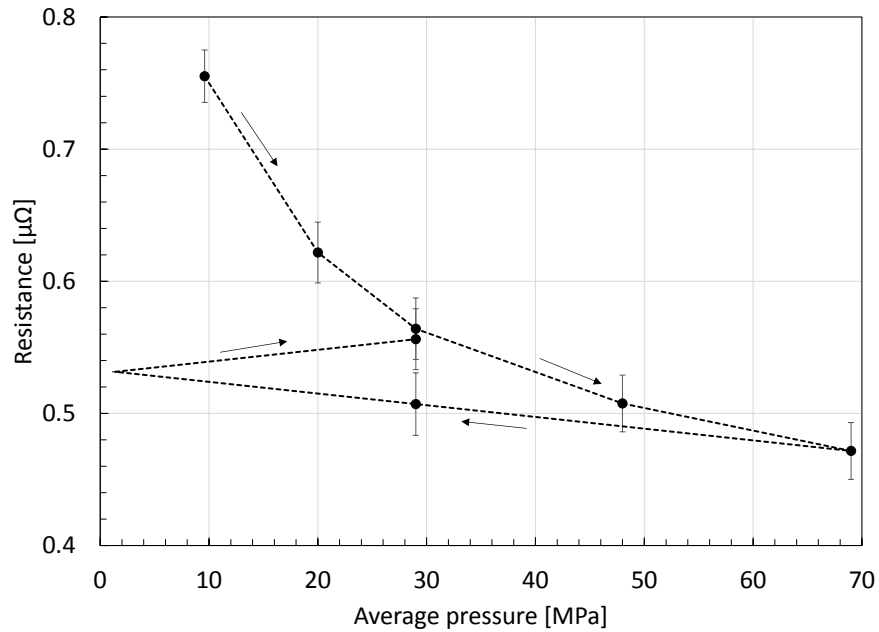


Figure 5-7: Tape-to-tape resistance vs. applied pressure for the joint without material between the terminals. The arrows indicate the chronological order of the measurements.

## 5.3 Cable experiment and total joint resistance

### 5.3.1 Experimental setup and procedure

For the full cable experiment, current was applied to all tapes simultaneously. In order to achieve a uniform and low resistance in the connection between the current leads and the joint sample, a “folding fan” termination (similar to the termination described by Takayasu in [70]) was fabricated in each sample. The termination consists of a 6.3 mm thick copper block with a 2.5 mm deep slot machined in one face. The stack of tapes is slightly twisted and the tapes spread out, such that a portion of the superconducting side of each tape is exposed. The tapes are then pressed against the copper block in the machined slot, the superconducting side facing the copper, and soldered. Voltage taps were soldered to the two external tapes of each sample, and additional voltage taps were bolted to the copper terminations and the bottom of the copper sample holders. In Figure 5-8 a picture of both joint samples with the termination soldered is shown, and the voltage taps locations is indicated.

The tests were performed with a 20 ton (178 kN) hydraulic bottle jack and a steel frame. The applied force was measured with an Omega LC412-5K load cell, with 5000 lb (22 kN) capacity and 7500 lb (33 kN) maximum capacity. Two 25 mm thick steel blocks were used to support the sample and to improve the stiffness of the testing apparatus. The bottom steel block is mounted on top of steel block with a ball joint. A 25 mm thick G10 block was used to thermally insulate the jack and prevent its oil from freezing. A plastic box was used as liquid nitrogen tank; the entire testing apparatus was placed inside the nitrogen tank. The experimental setup is shown in Figure 5-9. The power supply utilized was a 3000 A, 10 V current supply.

As in the single tapes experiment, the joints contact surfaces were lightly brushed with very fine grade 3M Scotch-Brite, then cleaned with acetone and finally with alcohol before every test. Depending on the condition of the test, additional material was added between the joint samples. Then the set up was assembled as described in the previous paragraph, and a small load (1.8 MPa) was applied to the joint to keep everything aligned. Liquid nitrogen was poured into the liquid nitrogen tank until its

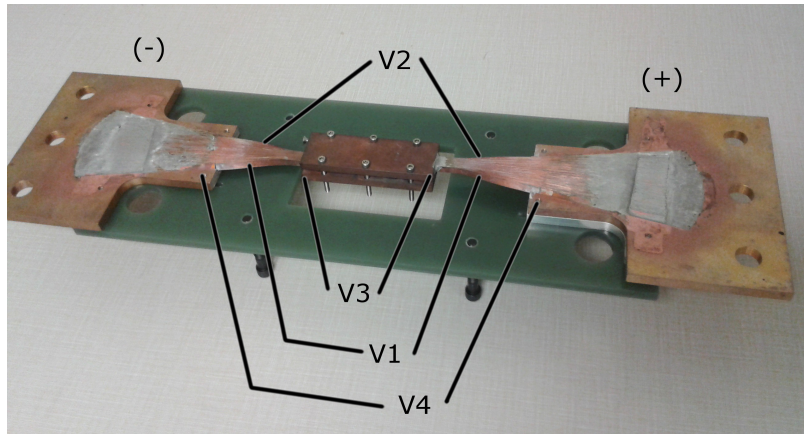


Figure 5-8: Cable experiment samples with terminations. The location of the voltage taps are marked with V1–V4: V1 and V2 are on the superconductors, V3 is on the copper sample holders, and V4 is on the copper terminations.

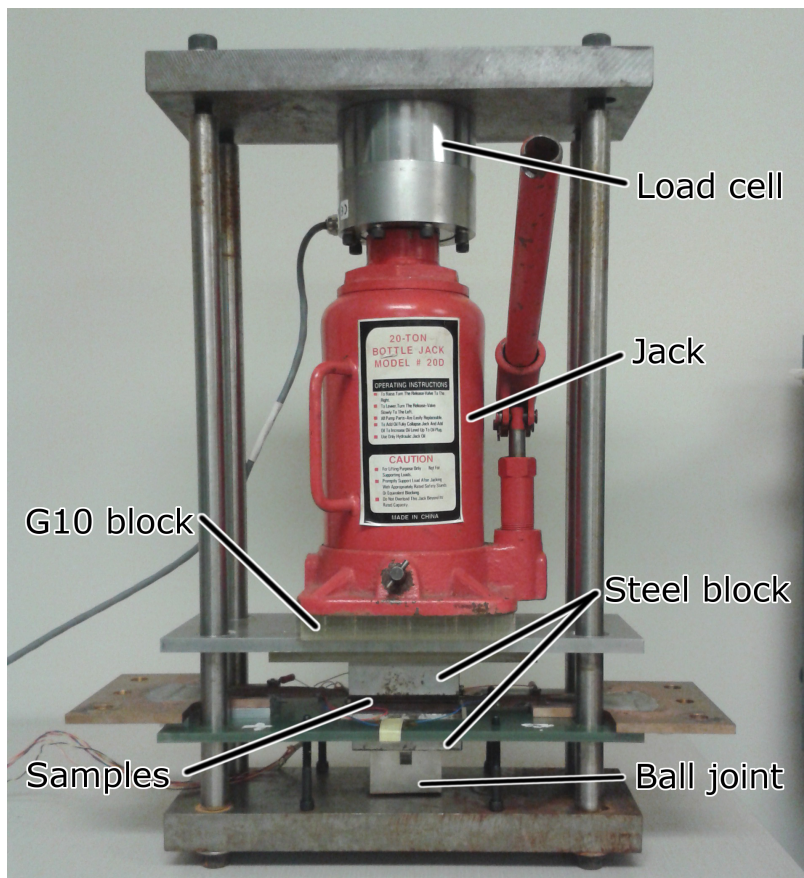


Figure 5-9: Experiment setup for cable resistance measurement. The joint pair is pressed with a 20 ton jack.

level was 20 mm above the superconductors; the liquid level was kept at least at that level throughout the experiment.

For each data point, the jack applied force was manually set near the desired value, and current was flown through the joint. During the experiment, the applied force would constantly change, probably due to thermal contraction of the hydraulic oil, and the applied load before and after each test was noted to estimate the pressure range on which the test was performed. The current was ramped up to 1000 A and then back to 0 A, except in the last run when the current was ramped up to 3000 A. Four Keithley 2182A nanovoltmeters were used for each pair of voltage taps, and a Keithley 2010 nanovoltmeter was used to measure the voltage drop across a calibrated shunt connected in series to calculate the applied current.

### **5.3.2 Results for cable experiment**

At each pressure, the voltage-current dependence is linear, with similar slope across the different pairs of voltage taps. An example of this is shown in Figure 5-10 for a measurement with Indium film at approximately 23 MPa of applied pressure, with current up to 3 kA. The resistance is calculated as the slope of the voltage-current curve.

The joint resistance vs. applied pressure results are shown in Figures 5-11, 5-12, 5-13 for experiments with feltmetal, with Indium and in bare condition respectively. The arrows represent the chronological order in which the measurements were made. Due to difficulties setting the applied force exactly, the load history in each test was slightly different. The first five measurements were performed with increasing pressure (10 MPa to 37 MPa), then the pressure was reduced to about 24 MPa, and at last the pressure was reduced to 2–3 MPa and increased to 25 MPa again. The test in bare condition was performed with an additional load cycle.

In each figure, the error bars in the pressure correspond to the range of pressures under which each measurement was made. The error bars in the resistance correspond to the range of resistances calculated from the voltage-current curves of the two voltage taps pairs soldered to the superconductors.

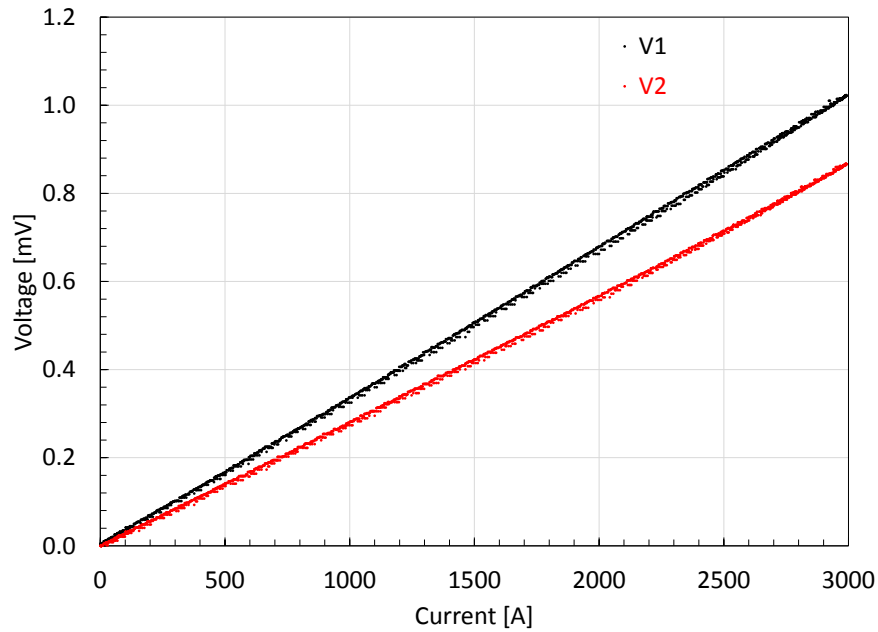


Figure 5-10: Voltage vs. current measurement for the cable test with Indium film. The two data sets correspond to different pairs of voltage taps. This was the last measurement made, with current up to 3 kA. The applied pressure was approximately 23 MPa.

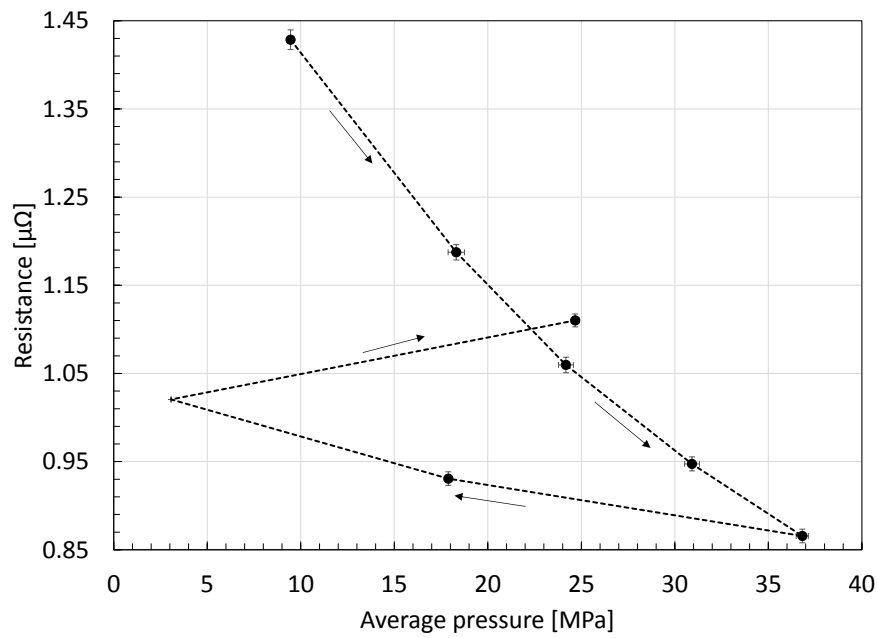


Figure 5-11: Cable resistance vs. applied pressure for the joint with felt-metal. The arrows indicate the chronological order of the measurements.

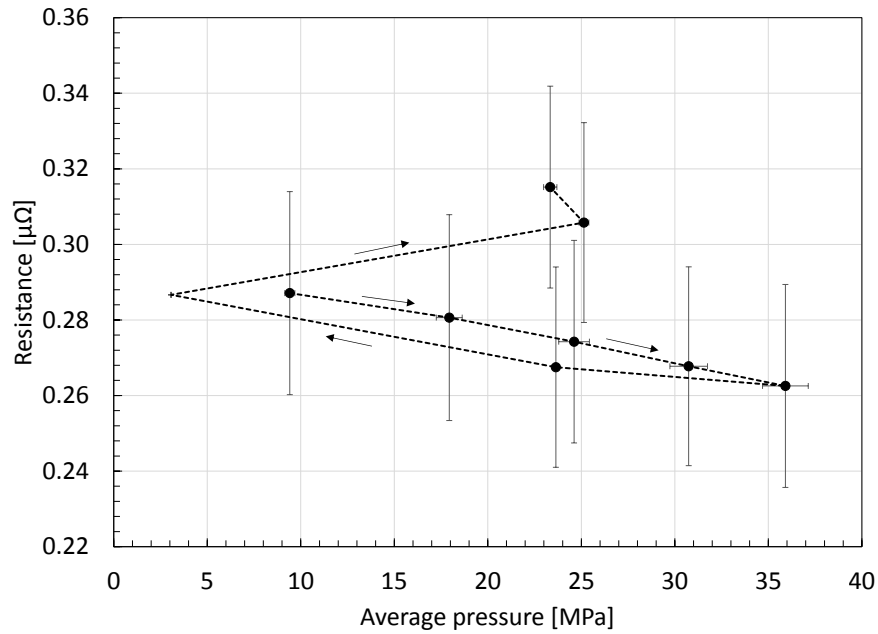


Figure 5-12: Cable resistance vs. applied pressure for the joint with  $50\mu m$  Indium film. The arrows indicate the chronological order of the measurements.

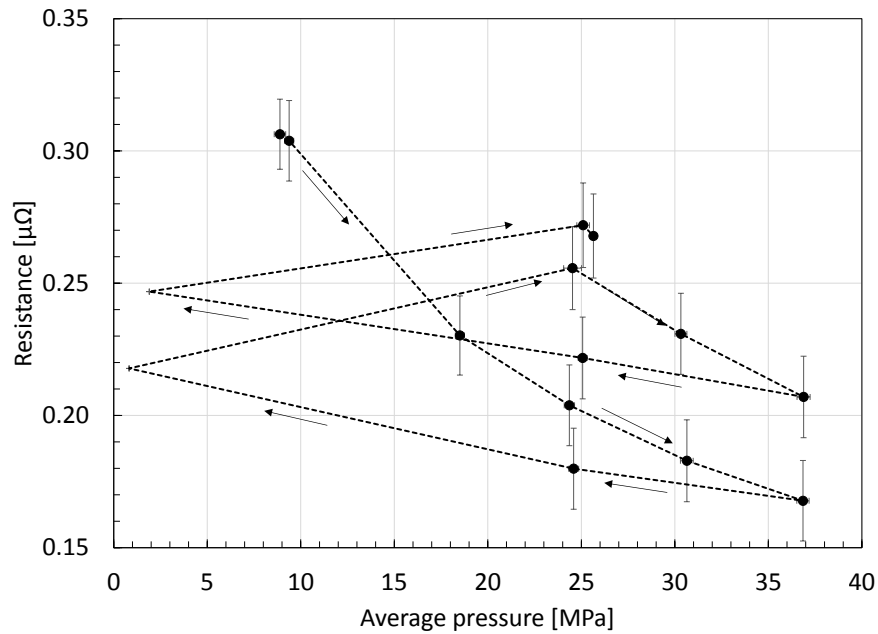


Figure 5-13: Cable resistance vs. applied pressure for the joint without material between the terminals. The arrows indicate the chronological order of the measurements.



All measurements show resistance increase after a pressure cycle. It may have been caused by misalignment in the test setup. The resistance at 36–37 MPa is 0.86–0.87  $\mu\Omega$  for feltmetal, 0.24–0.29  $\mu\Omega$  for Indium, and 0.15–0.18  $\mu\Omega$  for bare condition.

## 5.4 Experiment conclusions and influence in the electrical joint design

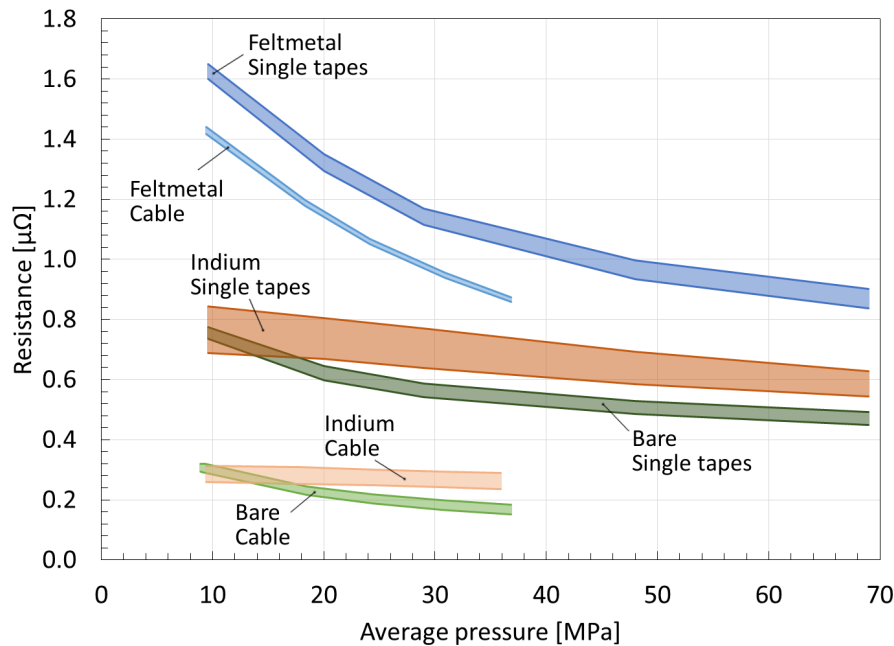


Figure 5-14: Summary of joint resistance vs. applied pressure for the three surface conditions considered. Only the first loading is shown for clarity. The limits of the bands are the maximum and minimum measured resistance for each condition. Applied pressure error bars are not shown.

A summary of the results presented in Sections 5.2 and 5.3 is shown in Figure 5-14. The ratio cable joint resistance to single tapes joint resistance is approximately 85 % with feltmetal, and approximately 40 % with Indium and in bare conditions. Both single tapes and cable experiments present the bare joint resistance to be lower than using Indium or feltmetal, and thus the bare joint condition will be used as the base design. To simplify the analysis only the average value of resistance will be used.

In Figure 5-15 an electrical circuit model of the joint is shown. The total joint

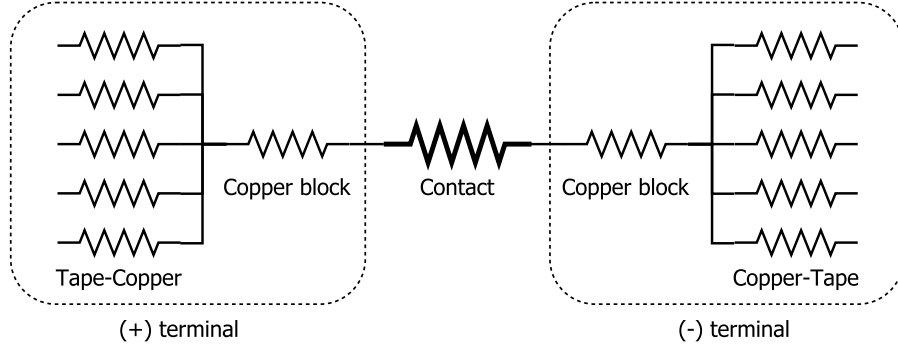


Figure 5-15: Electrical circuit model of the joint. The amount of tape-copper resistors is equal to the amount of tapes connected in each experiment: for the single tapes experiment is one, for the cable experiment is 80. The total resistance for each case is given by equation (5.1) and (5.2) respectively.

resistance measured can be divided into three parts: the resistance from each tape to the copper block  $R_{T-Cu}$ , the common resistance in the copper block  $R_{Cu}$  and the contact resistance  $R_{Ct}$ . For the single tapes experiment, there would only be one  $R_{T-Cu}$  resistance in each terminal, and the total joint resistance  $R_{Tot}^{ST}$  would be:

$$R_{Tot}^{ST} = 2R_{T-Cu} + 2R_{Cu} + R_{Ct} \quad (5.1)$$

For the cable experiment, the 80 tapes in each terminal would be connected in parallel, and the total joint resistance  $R_{Tot}^C$  would be:

$$R_{Tot}^C = \frac{2R_{T-Cu}}{80} + 2R_{Cu} + R_{Ct} \quad (5.2)$$

According to the contact resistance model by Holm [71],  $R_{Ct}$  depends on the average pressure  $p$ , nominal contact area  $A_0$  and the hardness  $H$  and the electric resistivity  $\rho$  of the surface material as follows:

$$R_{Ct} = \frac{\rho}{2} \sqrt{\frac{\pi \xi H}{p A_0}} \quad (5.3)$$

where  $\xi$  is a value between 0 and 1 that represents the quality of the surface, and is around 0.1–0.3 for average pressures larger than 1 kPa. In the bare joint case, the surface material is silver, its hardness  $H_{Ag}$  and its resistivity  $\rho_{Ag}$ .

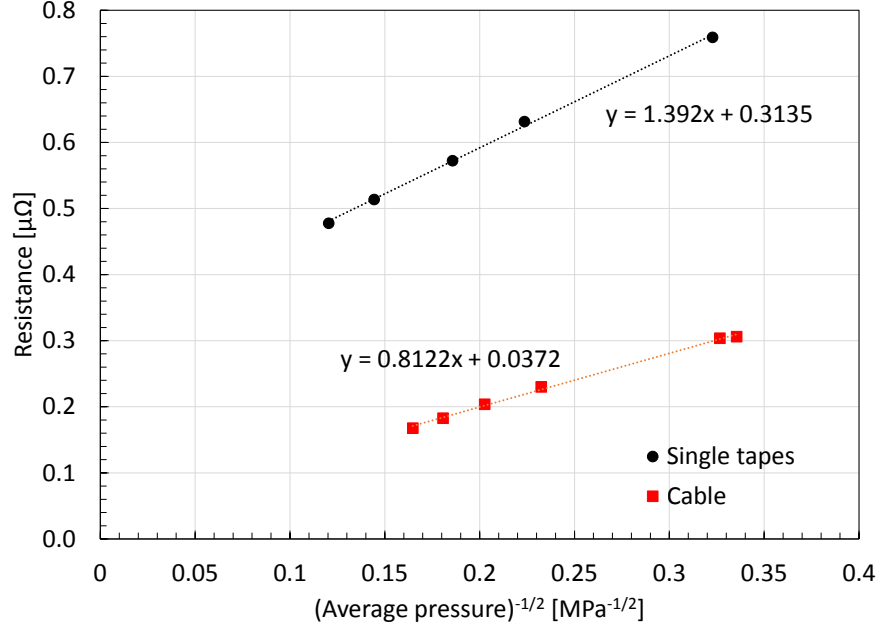


Figure 5-16: Resistance of bare joint as a function of the inverse square root of the applied average pressure for the single tapes and cable experiments. A linear regression was performed with both data sets, the results are shown next to the corresponding data set.

The values of  $R_{T-Cu}$  and  $R_{Cu}$  are hard to calculate analytically, but can be extracted from the measured data. In Figure 5-16 the values of resistance for the bare joint, from the single tapes and cable experiments, is plotted against the inverse of the square root of the applied average pressure. A linear fit was performed to each data series, the slope corresponds to the contact resistance contribution and the constant term corresponds to the sum of tape to copper block resistance and the common copper block resistance. The obtained values are, for single tapes:

$$R_{Tot}^{ST} = \frac{1.392}{\sqrt{p}} \mu\Omega \sqrt{MPa} + 0.3135 \mu\Omega \quad (5.4)$$

which corresponds to:

$$\frac{\rho_{Ag}}{2} \sqrt{\frac{\pi \xi^{ST} H_{Ag}}{A_0}} = 1.392 \mu\Omega \sqrt{MPa} \quad (5.5a)$$

$$2R_{T-Cu} + 2R_{Cu} = 0.3135 \mu\Omega \quad (5.5b)$$

And the values for the cable experiment:

$$R_{Tot}^C = \frac{0.8122}{\sqrt{p}} \mu\Omega \sqrt{MPa} + 0.0372 \mu\Omega \quad (5.6)$$

which corresponds to:

$$\frac{\rho_{Ag}}{2} \sqrt{\frac{\pi \xi^C H_{Ag}}{A_0}} = 0.8122 \mu\Omega \sqrt{MPa} \quad (5.7a)$$

$$\frac{2R_{T-Cu}}{80} + 2R_{Cu} = 0.0372 \mu\Omega \quad (5.7b)$$

From equations (5.5b) and (5.7b) the values of  $R_{T-Cu}$  and  $R_{Cu}$  can be estimated:

$$R_{T-Cu} = 0.14 \mu\Omega \quad (5.8a)$$

$$R_{Cu} = 0.017 \mu\Omega \quad (5.8b)$$

The resistivity of silver at 77 K is  $3 \cdot 10^{-9} \Omega m$  [72]. The hardness of silver at 77 K was estimated as three times its yield strength at that temperature (about 60 MPa [72]), and is about 180 MPa. Using these values in equations (5.5a) and (5.7a) the quality of the surface  $\xi$  can be calculated:

$$\xi^{ST} = 1.10 \quad (5.9a)$$

$$\xi^C = 0.38 \quad (5.9b)$$

The value of  $\xi^{ST}$  is too high, which suggests that for the single tape bare experiment the contact surface might have been contaminated. The value of  $\xi^C$  is a bit higher than the 0.1–0.3 expected, but is reasonable.

The geometric dependencies of the contact term have already been presented in equation (5.3). The  $R_{T-Cu}$  is to be inversely proportional to the length of the joint, and the term  $R_{Cu}$  is expected to be inversely proportional to the nominal area of the

joint. Taking this into account, the total expected joint resistance  $R_E$  for a similar joint can be extrapolated from the values presented in equations (5.8a), (5.8b) and (5.9b):

$$R_E = 0.8122\mu\Omega\sqrt{MPa} \cdot \sqrt{\frac{A_0}{pA}} + 2\frac{0.14\mu\Omega}{N}\frac{L_0}{L} + 2 \cdot 0.017\mu\Omega\frac{A_0}{A} \quad (5.10)$$

with  $L_0$  and  $A_0$  the length and the nominal area of the tested joint,  $L$  and  $A$  the length and the nominal area of the new joint,  $N$  the number of tapes in the new joint, and  $p$  the applied average pressure. Replacing with the numerical values of  $L_0$  and  $A_0$ , equation (5.10) becomes:

$$R_E = \frac{21.9\mu\Omega mm\sqrt{MPa}}{\sqrt{pA}} + \frac{21.3\mu\Omega mm}{NL} + \frac{24.4\mu\Omega mm^2}{A} \quad (5.11)$$

This equation can be applied to estimate the required size of the joints in the reactor. From the calculations in Section 2.2 the required amount of 6 mm wide tapes in the conductors in the innermost layer of the winding pack is 480, divided in six bundles. Each bundle would have 80 tapes and 8 mm width. Assuming the width of the contact area is 1 mm larger than the width of the bundle, the nominal contact area for each bundle would be 9 mm times its length  $L$ . The joint resistance of a single termination-jumper connection  $R_{T-J}$  for a conductor would consist in six equal parallel joints:

$$R_{T-J} = \frac{R_E}{6} \quad (5.12a)$$

$$= \frac{21.9\mu\Omega mm\sqrt{MPa}}{6\sqrt{9mm \cdot Lp}} + \frac{21.3\mu\Omega mm}{6 \cdot 80L} + \frac{24.4\mu\Omega mm^2}{6 \cdot 9mm \cdot L} \quad (5.12b)$$

The values of termination-jumper resistance as a function of length for several average applied pressures is shown in Figure 5-17. To achieve a resistance of 10 n $\Omega$  at 75 MPa the required termination length is 300 mm. At that point, decreasing the applied pressure by 33 % to 50 MPa increases the joint resistance by less than 20 %.

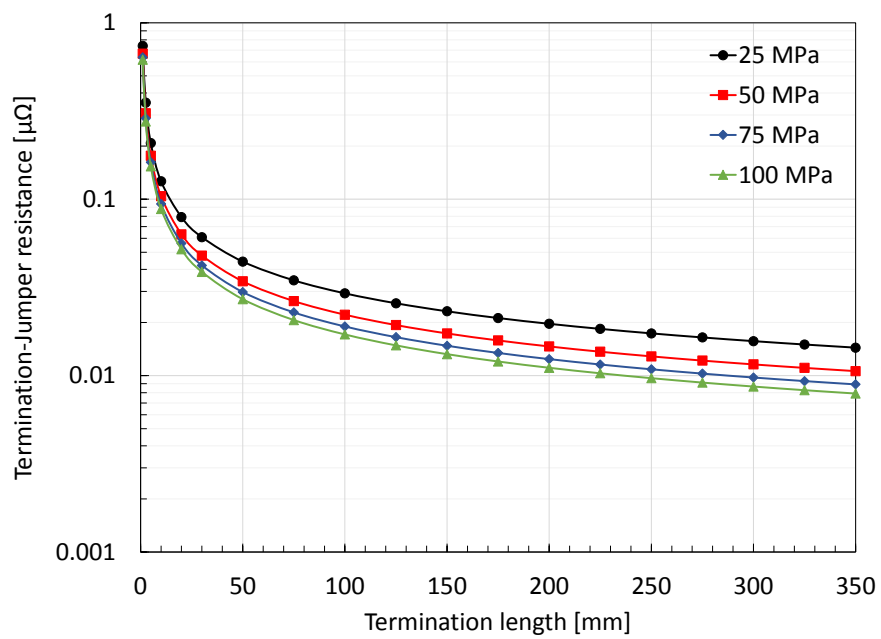


Figure 5-17: Estimation of the termination-jumper connection resistance for the reactor design for different applied average pressures. The goal of  $10 \text{ n}\Omega$  can be reached at 75 MPa and a joint length of 300 mm.

# Chapter 6

## Cooling Requirements & Maintenance Procedure

### 6.1 Cooling during operation

During operation, the sources of heat in the TF coils are two: nuclear heating distributed in the volume of the coil, and joule heating in the resistive joints. From the ARIES-I reactor studies, an estimation of the nuclear heating in the area of highest radiation is  $888 \text{ W/m}^3$  [9]. The maximum total nuclear heat generation  $Q_N$  in a conductor turn would be:

$$Q_N = 888 \frac{W}{m^3} A_{CICC} L_{Turn} \quad (6.1)$$

where  $A_{CICC}$  is the cross sectional area of a conductor,  $3600 \text{ mm}^2$ , and  $L_{Turn}$  is the length of a conductor turn. The length of the conductor in the top leg of the TF coil is approximately 13 m, and in the bottom leg is 24 m, for a total of approximately 37 m. Replacing these numbers in equation (6.1) yields  $Q_N \approx 120 \text{ W}$ .

The joule heating in each joint  $Q_J$  can be calculated from the operation current of the conductor  $I_{CICC}$  and the connection resistance  $R_{T-J}$  estimated in Section 5.4 as follows:

$$Q_J = I_{ICCC}^2 \cdot R_{T-J} = (94 \text{ kA})^2 \cdot 10 \text{ n}\Omega = 88 \text{ W} \quad (6.2)$$

As there are four joints per conductor turn in the TF coil, the total heating power in each conductor would be the sum of the nuclear heating  $Q_N$  and four times the joint heating  $Q_J$ . For a total of 246 conductors per TF coil, the total heating power in a single TF coil  $Q_{TF}$  is:

$$Q_{TF} = 246 \cdot (Q_N + 4Q_J) = 116 \text{ kW} \quad (6.3)$$

This number overestimates the nuclear heating in the conductors, but neglects the nuclear heating in the coil case volume. As the largest part of the coil case volume is in low radiation areas, it is expected that this calculation is still conservative. The total heating power in the 16 TF coils is approximately 1.9 MW, of which about 25 % is nuclear heating and 75 % joint heating. The required electric power  $P_{cool}$  to remove this heating power is [73]:

$$P_{cool} = \frac{16Q_{TF}}{\epsilon_c \cdot \eta} \quad (6.4)$$

where  $\epsilon_c$  is the Carnot efficiency and  $\eta$  is the practically achievable efficiency. Carnot efficiency for cooling from 300 K to 20 K is:

$$\epsilon_c = \frac{20K}{300K - 20K} = \frac{1}{14} \quad (6.5)$$

and the practically achievable efficiency can be calculated from the correlations compiled by Kittel [73]:

$$\log_{10}(\eta) = -0.92237 + 0.07763 \log_{10} \left( 1 + \frac{16Q_{TF}}{1W} \right) = -0.436 \quad (6.6a)$$

$$\eta = 0.367 \quad (6.6b)$$

Replacing the values from equations (6.3), (6.5) and (6.6b) in equation (6.4):



$$P_{cool} = \frac{16 \cdot 116 \text{ kW}}{1/14 \cdot 0.367} = 71 \text{ MW} \quad (6.7)$$

The TF coils are cooled with pressurized liquid hydrogen at 20 K. The conductors and the joints are cooled by independent liquid hydrogen circuits. The details on the cooling strategies and expected operation temperatures for the coil and the joint are described in Sections 6.1.1 and 6.1.2 respectively.

### 6.1.1 Cooling the coil conductors

The conductors in the coil are cooled by liquid hydrogen at 20 K and 0.6 MPa, flowing through a 7 mm diameter conduit in the center of the conductor. At this pressure the boiling temperature of liquid hydrogen is approximately 28.2 K [74]. As the liquid flows through the channel its temperature increases and friction reduces its pressure. The liquid mass flow rate  $\dot{m}$  must be high enough to successfully remove the heat load in the coil while remaining in the liquid phase. The thermal properties of liquid hydrogen were extracted from [74].

The pressure drop in the cooling channel  $\Delta p$  can be calculated from the Darcy-Weisbach equation [75]:

$$\Delta p = 8f_D \frac{L}{a^5} \frac{\dot{m}^2}{\delta \pi^2} \quad (6.8)$$

where  $f_D$  is the friction factor,  $L$  the length of the channel,  $a$  its diameter, and  $\delta$  the mass density of liquid hydrogen. For reference, a pressure drop of 120 kPa reduces the boiling temperature of liquid hydrogen to 27 K. As a conservative estimation the length of the channel will be assumed to be the length of a coil turn, 37 m. Assuming the cooling channel is smooth, the friction factor is approximately:

$$f_D = [0.790 \log_{10}(Re) - 1.64]^{-2} \quad (6.9)$$

with  $Re$  the Reynolds number of the coolant in the conductor. This approximation applies for  $Re > 3000$ . The Reynolds number is calculated as:

$$Re = \frac{4\dot{m}}{\pi\mu a} \quad (6.10)$$

with  $\mu$  the viscosity of the fluid. The output temperature  $T_{out}$  of the liquid can be estimated from the specific enthalpy change through the cooling channel:

$$\int_{20K}^{T_{out}} c_p dT = \frac{Q_N}{\dot{m}} \quad (6.11)$$

where  $c_p$  is the specific heat of hydrogen. Assuming the temperature gradients in the conductor are dominated by the convection heat transfer, the maximum temperature of the conductor  $T_{CICC}$  can be roughly estimated from:

$$\frac{Q_N}{A_C} = h_{HT}(T_{CICC} - T_{out}) \quad (6.12)$$

where  $A_C$  is the wet area of the cooling channel, equal to  $\pi aL$ , and  $h_{HT}$  the convection heat transfer coefficient.  $h_{HT}$  can be calculated from the Nusselt number  $Nu$ :

$$h_{HT} = \frac{kNu}{a} \quad (6.13)$$

where  $k$  is the thermal conductivity of liquid hydrogen. The Nusselt number can be calculated from the Dittus-Boelter correlation [75]:

$$Nu = 0.023Re^{4/5}Pr^{0.4} \quad (6.14)$$

with  $Pr$  the Prandtl number. This approximation applies for approximately  $Re > 10^4$  and  $0.6 < Pr < 160$ . The Prandtl number is calculated as:

$$Pr = \frac{\mu c_p}{k} \approx 1.14 \quad (6.15)$$

Equations (6.8), (6.11) and (6.12) are solved for several input mass flows. The results are shown in Table 6.1. A mass flow of 4 g/s could be a good tradeoff between low pressure drop and mass flow, and efficient cooling of the conductor, keeping the

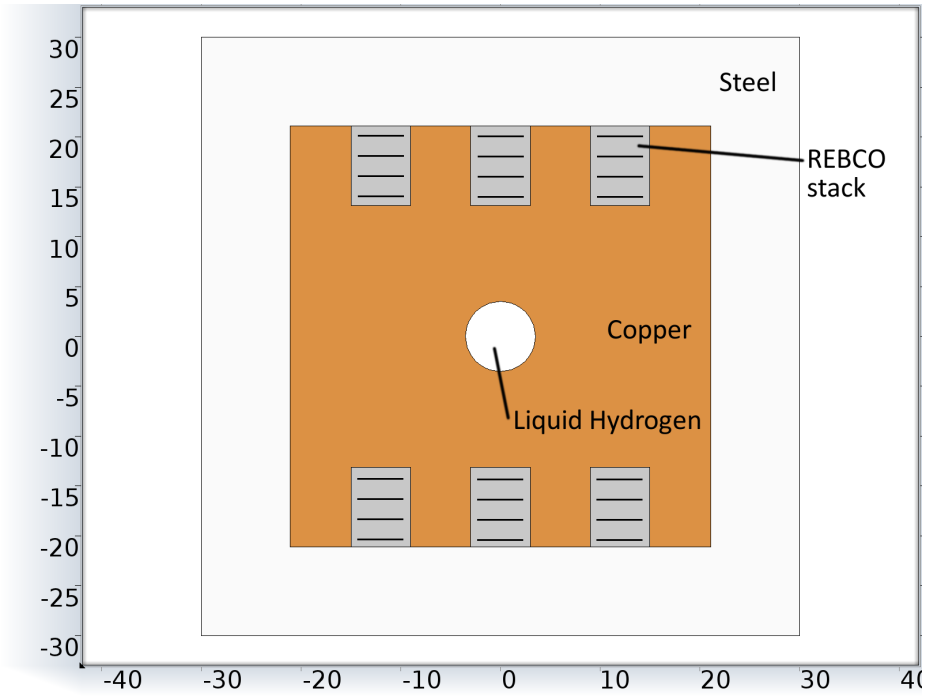


Figure 6-1: Geometry used for the temperature distribution simulation in the coil during operation. The scale is in mm. The lines in the REBCO stacks represent the direction of the tapes.

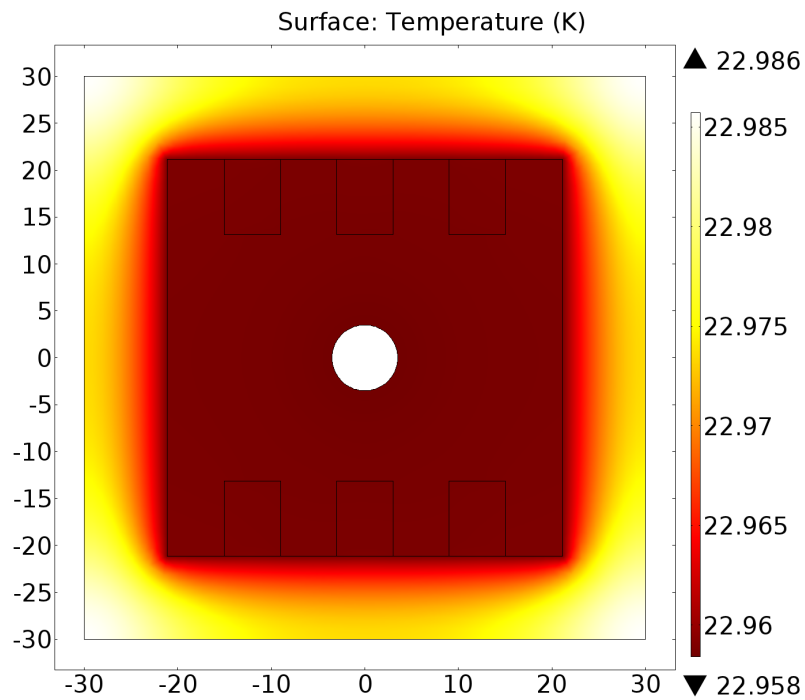


Figure 6-2: Temperature distribution in the conductor during operation. The liquid hydrogen is at 22.9 K, its maximum temperature along the conductor. The temperature in the conductor is about 0.1 K higher, with a high degree of uniformity.

maximum temperature of the conductor at only 23 K (3 K above the design point). The total hydrogen mass flow required to refrigerate all the conductors in the 16 TF coils is about 16 kg/s.

Table 6.1: Coil conductor cooling conditions.

$\dot{m}$	$Re$	$\Delta p$	$T_{out}$	$T_{CICC}$
[g/s]	[ $10^4$ ]	[kPa]	[K]	[K]
2	2.6	2.5	25.5	25.6
4	5.2	8.3	22.9	23.0
6	7.8	17.3	22.0	22.0
8	10.4	28.8	21.5	21.5
10	13.0	43.0	21.2	21.2

A 2-D finite element analysis of the temperature distribution in a conductor was performed using COMSOL, a commercial multiphysics code [60]. The analyzed geometry corresponds to the first conductor layer as described in Section 2.2, and is shown in Figure 6-4. A “thermal insulation” boundary condition was set on the external conductor walls to simulate symmetry. The liquid hydrogen in the internal cooling channel was simulated as a “convective heat flux” boundary condition in the cooling channel walls. The convection coefficient was calculated for a liquid hydrogen flow rate of 4 g/s, and the liquid temperature was 22.9 K representing its warmest point in the cooling circuit. The nuclear heating is simulated as a distributed volumetric heat load of (888 W/m<sup>3</sup>) in the entire conductor volume. The thermal properties of steel, copper and superconducting tapes are summarized in Appendix C. The results are shown in Figure 6-2. The temperature in the conductor is about 23.0 K for liquid hydrogen at 22.9 K, as expected from the calculation according to equation (6.12).

### 6.1.2 Cooling the electrical joints

The electrical joints are cooled by liquid hydrogen at 20 K and 0.6 MPa. Each joint has four independent cooling channels, two in the coil termination and one in each jumper termination. The cooling channels are 4 mm in diameter. The cooling

channels are U-shaped near the joint, with the inlet and outlet far from the joint area. Because of this, the liquid hydrogen flows through the joint area twice. An schematic drawing of the cooling channels in the joint is shown in Figure 6-3. Some heat exchange between the upstream (colder) and downstream (warmer) sections of the cooling channels is expected, yielding lower maximum temperatures in the joint. This effect it will be conservatively ignored for simplicity.

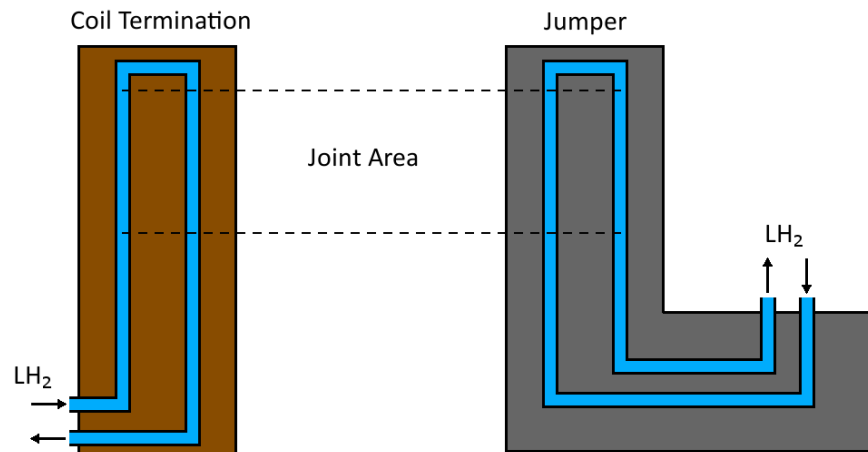


Figure 6-3: Schematic drawing of the cooling channels in the joint.

The hydraulic length  $L_H$  of the cooling channel is the total length of the channel, estimated as the length of the jumper, about 7.7 m. The thermal length  $L_T$  of the cooling channel is the length of the channel in the heat transfer area near the joint, estimated as twice the length of the joint (0.6 m). The mass flow in each channel is  $\dot{m}$ , the total liquid mass flow rate between the four channels is  $4\dot{m}$ .

The equations used to estimate the liquid hydrogen state and the temperature in the coil during operation can be used for the joint, with some modifications. To obtain the pressure drop in the cooling channels in the joint  $\Delta p$  equations (6.8), (6.9) and (6.10) are used, replacing  $L_H$  as the length of the channel and  $\dot{m}$  as the mass flow rate. The output temperature of the liquid is calculated according to equation (6.11), using  $4\dot{m}$  as the mass flow rate. To obtain the maximum joint temperature  $T_{Joint}$  equation (6.12) is used, with the wet area calculated as  $4\pi aL_T$  and  $Q_J$  instead of  $Q_N$  as the heating power.

These equations are solved for several total mass flows  $4\dot{m}$ . The results are shown in Table 6.2. A mass flow of 6 g/s could be a good tradeoff between low pressure drop and mass flow, and efficient cooling of the conductor, keeping the maximum temperature of the conductor at only 22.4 K (2.4 K above the design point). The total hydrogen mass flow required to refrigerate all the joints in all the conductors in the 16 TF coils is about 94 kg/s, or about 6 times that of the TF legs.

Table 6.2: Joint conductor cooling conditions.

$4\dot{m}$ [g/s]	$Re_C$ [ $10^4$ ]	$\Delta p$ [kPa]	$T_{out}$ [K]	$T_{Joint}$ [K]
2	1.1	0.7	24.2	26.5
4	2.3	2.2	22.2	23.5
6	3.4	4.4	21.5	22.4
8	4.5	7.4	21.1	21.8
10	5.7	10.9	20.8	21.5

A 2-D finite element analysis of the temperature distribution in the joint was performed using COMSOL. The analyzed geometry is shown in Figure 6-4, which corresponds to the joint geometry described in Section 4.3. The nuclear heating is simulated as a distributed volumetric heat load of (888 W/m<sup>3</sup>) in the entire conductor volume. The joint Joule heating is simulated as a heat load of 88 W distributed in the 0.3 m long joint contact surface. A “thermal insulation” boundary condition was set on the external walls to simulate symmetry. The liquid hydrogen in the internal cooling channels was simulated as a “convective heat flux” boundary condition in the walls of the cooling channels. The convection coefficient was calculated for a liquid hydrogen flow rate of 6 g/s, and the liquid temperature was 21.5 K representing its warmest point in the cooling circuit. This simulation ignores the heat exchange between the upstream and downstream sections of the cooling channel, and conservatively assumes all the liquid is at the warmest temperature. The thermal properties of steel, copper and superconducting tapes are summarized in Appendix C. The results are shown in Figure 6-2. The results are shown in Figure 6-5. The temperature in

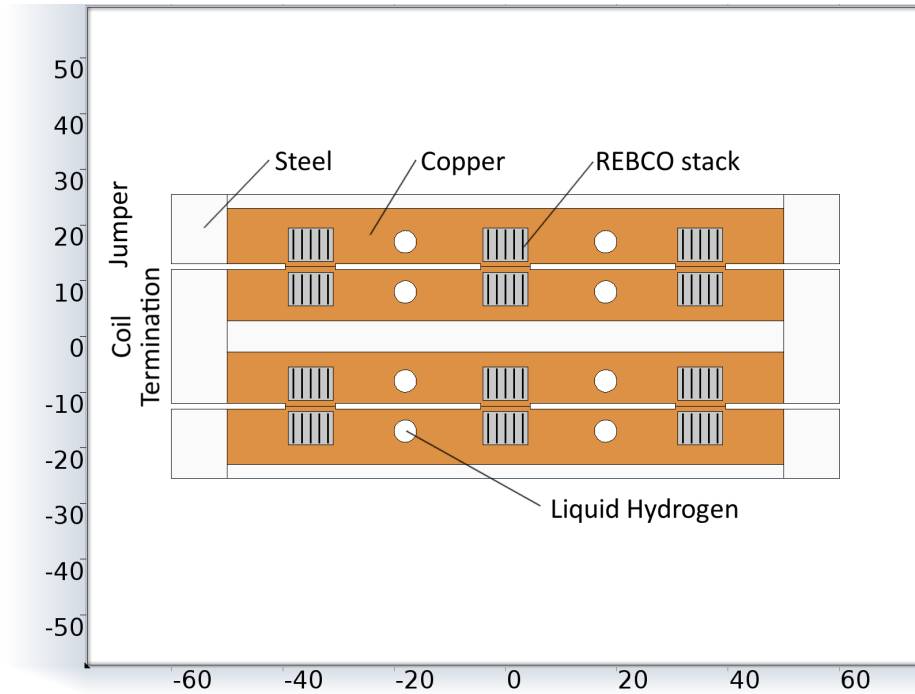


Figure 6-4: Geometry used for the temperature distribution simulation of the joint during operation. The scale is in mm. The lines in the REBCO stacks represent the direction of the tapes.

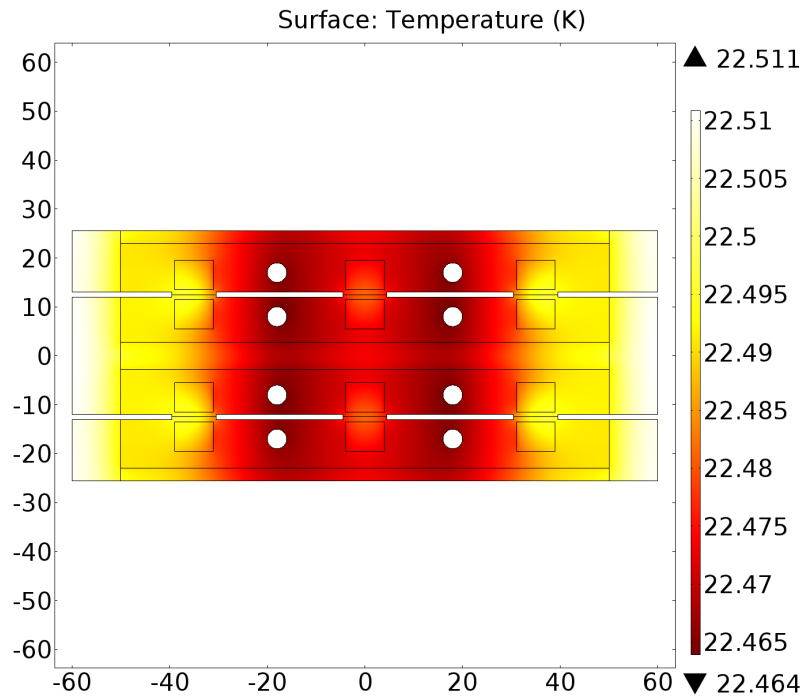


Figure 6-5: Temperature distribution in the joint during operation. The liquid hydrogen is at 21.5 K, its maximum temperature along the joint cooling channel. The temperature in the conductor is about 1.0 K higher.

the joint is about 22.5 K for liquid hydrogen at 21.5 K, similar to what was expected from the calculation according to equation (6.12).

## 6.2 Maintenance protocol

The reactor is expected to require maintenance once every 1–2 full power years. The most important goal of reactor maintenance is removing the entire vacuum vessel, which contains the divertor and other plasma facing components (the parts with higher expected erosion), and placing a new vacuum vessel in its place. As this design assumes a liquid blanket, blanket maintenance is not required, thus eliminating a burdensome and time consuming task. For reference, full blanket replacement would take about 2 years for ITER [36]. Maintenance and repair of other components can be done in parallel, in order to reduce the down time of the power plant.

The proposed maintenance protocol is outlined in Table 6.3. During the maintenance period, the working day will be 24 hours (3 shifts of 8 hours each) to reduce the down-time of the reactor. Of these activities, the ones expected to take the longest time are magnet warm-up and cool-down and electrical joint removal and installation. The expected time to warm-up and cool-down the magnets is calculated in the following subsection. Estimation of the electrical joint removal and installation time requires a more detailed design, including the design of the jumper and pin handling equipment and other auxiliary components, and such detailed design is beyond the scope of this thesis.

For reference, the estimate duration of the major refueling operations in a 1100 MWe Westinghouse PWR fission reactor, excluding the fuel shuffle, is about 5–8 days [76]. These refueling operations in a PWR reactor are similar to the proposed maintenance activities for the tokamak: for instance, removing cooling ducts, insulation, bolts and cable trays, installing lift rig and reactor vessel head removal. Though the size of the tokamak reactor is larger than the PWR, the main challenge is the same: remote handling due to nuclear activation.



Table 6.3: Activities required for maintenance.

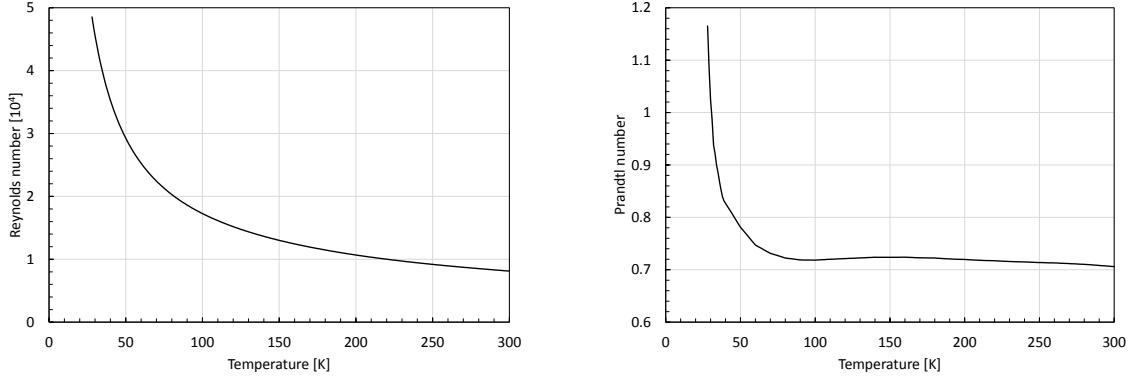
Activities	
1	Warm up magnets
2	Drain liquid blanket
3	Open cryostat
4	Remove electrical joint
5	Remove blanket pipe connections
6	Remove bolts and dovetails
7	Lift top leg of the magnets
8	Remove vacuum vessel
9	Install new vacuum vessel
10	Install top leg of the magnets
11	Install bolts and dovetails
12	Install blanket pipe connections
13	Install electrical joint
14	Close cryostat
15	Replenish liquid blanket
16	Cool down magnets

### 6.2.1 Coil warm-up and cool-down for maintenance

The coil will be brought to room temperature for maintenance, and then cooled down to 20 K when ready to be operated again. Hydrogen will be used to exchange heat with the coil, in liquid form below its saturation temperature (28 K at 0.6 MPa of pressure) and in gaseous form above that temperature.

The required time to warm up and cool down the coils is mostly determined by the 28–300 K region, as the heat capacity of the materials in the coil is much larger above 100 K than around 20 K. That simplifies the estimation of the required time, as only hydrogen gas needs to be considered as the cooling or warming fluid.

In order to estimate the required time to warm up and cool down the coil, a 3D time-dependent finite element analysis of the temperature distribution in a single conductor was performed using COMSOL. The simulated conductor is 37 m long, with the cross section of layer 1 as described in Section 2.2. Hydrogen gas flows through



(a) Reynolds number

(b) Prandtl number

Figure 6-6: Reynolds and Prandtl numbers for gaseous hydrogen heat transfer, for temperatures between 28–300 K. These values approximately fit in the range of application of the Dittus-Boelter correlation.

the cooling channel. The temperature distribution of the flowing hydrogen gas was simulated. The solid conductor and hydrogen gas models were linked with a “heat flux” boundary condition in the cooling channel walls that simulates the convective heat transfer. A “thermal insulation” boundary condition was set on the external walls to simulate symmetry. The properties of steel, copper, superconducting tapes and gaseous hydrogen are summarized in Appendix C.

The hydrogen gas mass flow  $\dot{m}_g$  is 0.4 g/s. The Reynolds ( $Re_g$ ) and Prandtl ( $Pr_g$ ) numbers for hydrogen gas are calculated from equations (6.10) and (6.15), and their value for temperatures between 28 and 300 K is shown in Figure 6-6. The values obtained approximately fit in the range of application of the Dittus-Boelter correlation, which is used to calculate the Nusselt number ( $Nu_g$ ):

$$Nu_g = 0.023 Re_g^{4/5} Pr_g^{n_{DB}} \quad (6.16)$$

where  $n_{DB}$  a constant equal to 0.4 when the solid is cooling down (equivalent to equation (6.14)) and 0.3 when it is warming up. The convection coefficient can be obtained replacing equation (6.16) in (6.13), and is used as a parameter for the “heat flux” boundary conditions in the transient simulation.

The input hydrogen gas temperature  $T_{g,in}$  during the sequence was set as:

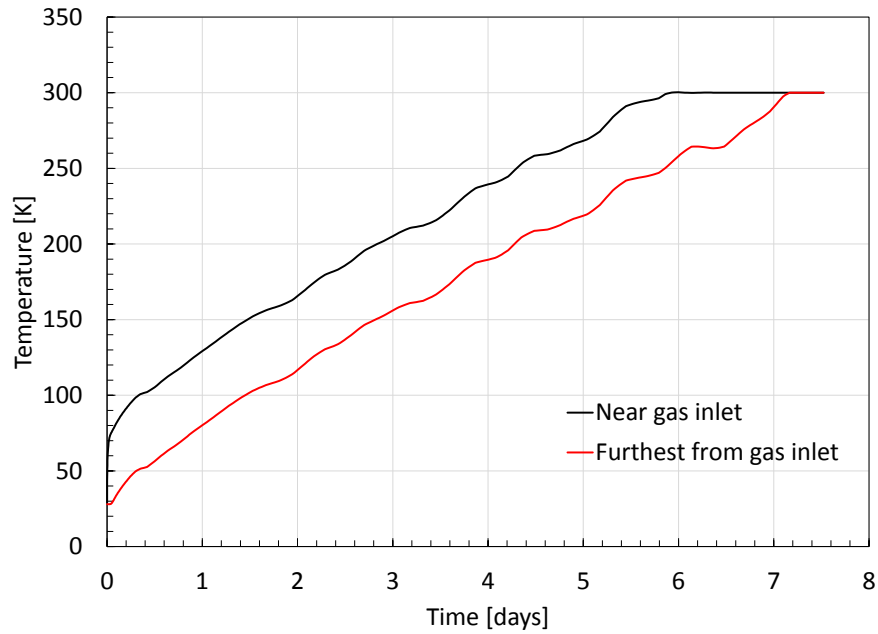


Figure 6-7: Temperature in the coil for warming up transient. The coil requires about 7 days and 5 hours to reach 300 K, starting at 28 K. The temperature difference is never larger than 50 K in order to avoid excessive thermal stress in the coils.

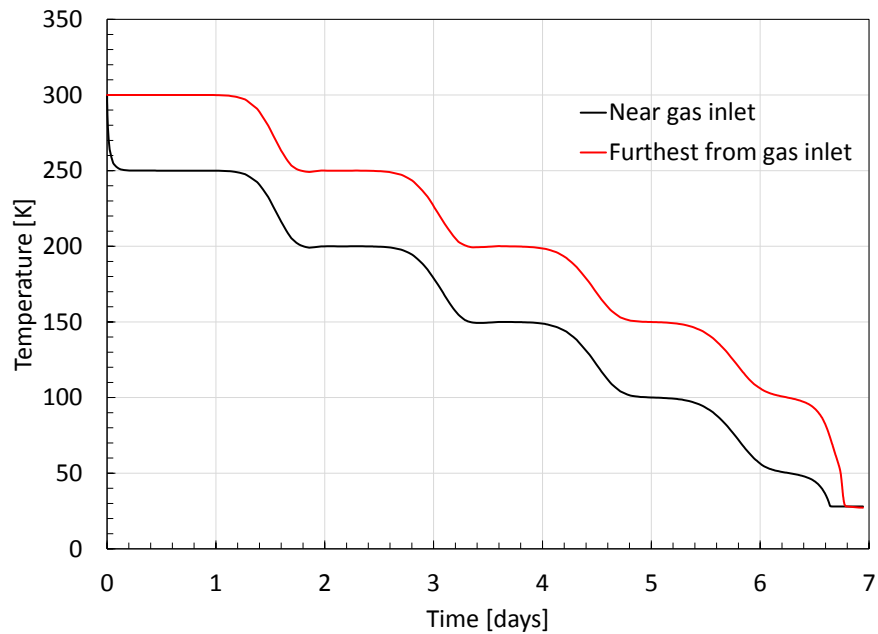


Figure 6-8: Temperature in the coil for cooling down transient. The coil requires less than 7 days to reach 28 K, starting at 300 K. The temperature difference is never larger than 50 K in order to avoid excessive thermal stress in the coils.

$$T_{g,in} = \begin{cases} \max(28K, T_{s,Far} - 50K) & \text{for cooling down} \\ \min(300K, T_{s,Far} + 50K) & \text{for warming up} \end{cases} \quad (6.17)$$

with  $T_{s,Far}$  the temperature in the conductor at the furthest point from the hydrogen gas input. The initial temperature of the conductor and hydrogen gas is 28 K when warming up and 300 K when cooling down. The results of the temperature in the coil for the warming up and cooling down transients are shown in Figures 6-7 and 6-8 respectively. For warm-up, the temperature evolution is relatively smooth, as the low thermal capacity and high thermal conductivity of the metals at low temperature naturally yield a relatively constant thermal gradient along the length of the conductor. When cooling down, the temperature in the furthest point from the gas inlet is delayed with respect to the temperature near the gas inlet. This “staircase” like feature is caused by the high thermal capacity and relatively low thermal conductivity of the metals near room temperature, which generates a more localized temperature gradient that slowly advances along the conductor length.

The warm-up transient is estimated to be about 7 days and 5 hours long, and the cool-down about 6 days and 19 hours long. These times are roughly proportional to the length of the cooling channels: for instance, having separated hydrogen gas circuits for the top and bottom legs (with cooling channels 13 m and 24 m long, respectively) and cooling/warming the two legs at the same rate, the transient times are expected to be reduced to about 65 %.

# Chapter 7

## Conclusions

### 7.1 Summary

A new toroidal field magnet conceptual design for an ARIES-I class tokamak fusion reactor has been developed. The maximum magnetic field in the magnets is approximately 20 T. REBCO superconductors are used as conductors to achieve the large required magnetic fields at a relatively high temperature (20–23 K) with almost no electrical power loss. The magnets are divided into two parts and can be detached and remounted to allow the internal components of the reactor (such as the vacuum vessel) to be removed vertically as one piece.

Different aspects of the design were analyzed to evaluate its viability. To evaluate the mechanical response of the magnets to the large forces in the winding pack, the coil composition was calculated and structural materials were compared to choose an optimum. Stress simulations in the coil and in the joint area were performed at the high magnetic field expected; the stress obtained in the coil structure is lower than the maximum allowable of the stainless steel 316LN structural material, and the equivalent strain on the superconducting tape is lower than the maximum allowed before permanent degradation. A few minor areas in the bolts in the outer midplane joint and in the pins and sockets that hold the joint support ring in the top joint have stresses larger than allowed for 316LN. Obtaining an engineering solution to reduce the stresses in these areas is critical, but the effort required to successfully design

these areas with acceptable design is beyond the scope of this thesis.

The coil joint was designed to withstand the mechanical force and make the electrical connection in different areas of the coil. The mechanical joint includes dovetail systems to lock the two parts of the magnets together. In the electrical joint the REBCO stacks are connected through the edges and protected with a thin copper layer. The insulation and cooling in the electrical joint was analyzed, and a small scale characterization experiment of the joint resistance was made.

In addition to the analysis of these individual components, the expected maintenance procedure was outlined. Two of the most time consuming activities for this are the thermal transients: cool down and warm up the coils between room and operation temperature, both estimated to last about 7 days.

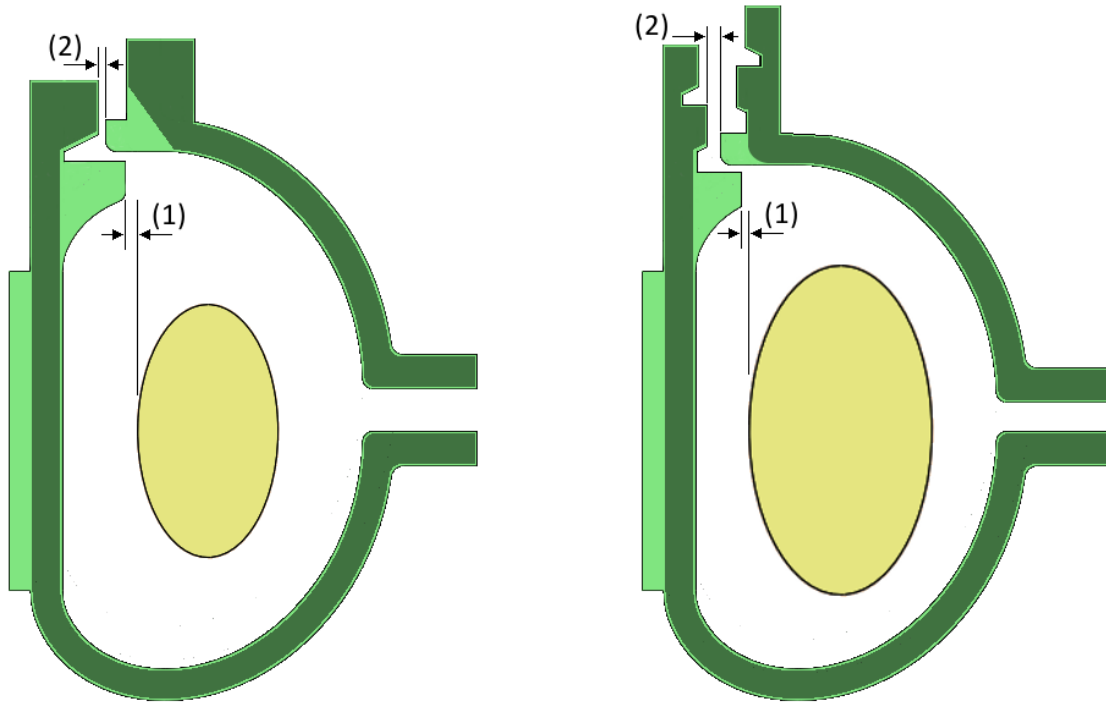
The analysis of these aspects of the magnets design presented in this thesis is encouraging. The analysis results are acceptable, and no insuperable problems have been identified. The ideas described in the previous chapters can be used as a conceptual design for a full engineering design of demountable magnets for ARIES-I class reactors, and also can be used as a starting point in the design of magnets for other fusion reactors.

## **7.2 Applicability to other reactor designs**

Some or all of the concepts described in this thesis can be applied to other reactor designs. Depending on the reactor dimensions and characteristics some modifications would be needed.

The most important issue to take into account when applying this concept to other designs is the top joint, its location and size. The radial size of the mechanical joint is limited by the size of the vacuum vessel in order to allow vertical removal of the vacuum vessel in one piece. The size of the dovetail in the top leg of the TF coil is limited by the size of the electrical joint. The electrical joint needs to be large enough to accommodate the coil terminations and the jumpers – it roughly requires twice the radial space as the winding pack. This is shown in Figure 7-1a.

For low aspect ratio tokamaks, where the distance between the TF coils and the vacuum vessel is similar to the thickness of the TF coil, using the electrical joint design proposed in Chapter 3 may not be viable. A possible solution is outlined in Figure 7-1b, and consists in extending the electrical joint area vertically, such that only a few conductors are expanded radially at each joint position, reducing the required radial space for the joint.



(a) Concept for ARIES-I reactor.

(b) Concept for low aspect ratio reactors.

Figure 7-1: Modification of joint concept for other reactor designs. In both figures the radial space between the vacuum vessel and the inner leg, and between the top leg and the top electrical joint are marked (1) and (2) respectively. For low aspect ratio reactors, keeping the electrical joint equal to the proposed ARIES-I joint would result in too low radial margin (2), which can be solved with multiple joints.

### 7.3 Future Work

In the short term, several tasks can be done to improve the magnet design described in this thesis. A full scale joint prototype can be built, in order to corroborate the joint resistance calculations and to check the installation procedure. Full characterization

of REBCO tapes at the operation conditions (22 K, 0–25 T) is required to optimize the winding pack composition. Additionally, characterization of REBCO cables at the mechanical loads that they will be subject to is necessary.

The winding pack insulation has been only briefly discussed in this thesis. The use of no-insulation coils has been suggested and demonstrated for continuously wound superconducting NMR magnets [77], reporting improved mechanical integrity and thermal stability. No-insulation magnets could be of interest for demountable magnets for fusion as a quench protection mechanism. Analysis of this option, in addition to further analysis of the traditional coil insulation, is necessary to optimize the coil composition.

Detailed engineering design of the coil is required to reduce the areas with high stresses. In addition, the coils can be optimized, removing unnecessary coil volume and reducing the number of parts.

The coils structural material was selected from a list of high strength cryogenic alloys. New alloys and composites with better performance in cryogenic conditions could allow increasing the magnetic fields or reducing the required size of the coils.

In the longer term, the engineering effort has to be concentrated into a broader magnet R&D program. In addition to the conductor and joint designs proposed here, other alternative concepts must be developed and thoroughly evaluated. Production of REBCO tape must be standardized, with guaranteed minimum performance. The ultimate test would be to build a full scale magnet, to check at the operation conditions the behavior of all the systems.



# Appendix A

## Critical current of REBCO tapes estimation

There is no complete characterization of the critical current density of REBCO tapes as function of magnetic field magnitude and direction at 22 K. The critical current density is estimated with data from several sources [8, 78, 79, 37].

The dependence of the critical current density at 22 K ( $J_C^{22}(B, \theta)$ ) with magnetic field magnitude ( $B$ ) and direction ( $\theta$ , measured as angle between magnetic field and the normal to the tape plane) is:

$$J_C^{22}(B, \theta) = J_{C\perp}^{22}(B) + (J_{C\parallel}^{22}(B) - J_{C\perp}^{22}(B)) \exp\left(-\frac{90^\circ - \theta}{\theta_0}\right) \quad (\text{A.1})$$

where  $J_{C\perp}^{22}$  and  $J_{C\parallel}^{22}$  are the critical current densities at 22 K with magnetic field perpendicular ( $\theta = 0$ ) and parallel ( $\theta = 90^\circ$ ) to the tape plane, and  $\theta_0$  a parameter. In Figure A-1 the value of  $J_C^{22}$  versus the angle between the magnetic field and the normal to the tape is shown for several magnetic fields, calculated according to this equation.

The values of  $J_{C\perp}^{22}$  and  $J_{C\parallel}^{22}$  are estimated from measurements of critical current density at 4.2 K ( $J_{C\perp}^{4.2}$  and  $J_{C\parallel}^{4.2}$ ). To obtain the relationship between critical current density at 22 K and 4.2 K, data of lift factor as function of magnetic field for both orientations at several temperatures was taken from [79]. The ratio between the

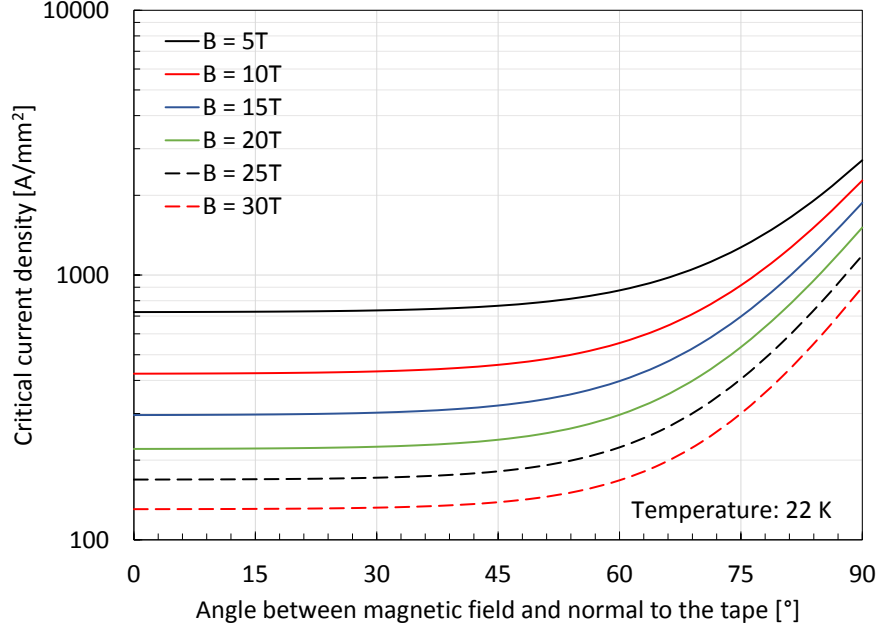


Figure A-1: Critical current of REBCO tapes vs. magnetic field angle to the tape, at several magnetic fields and 22 K.

critical current density at 22 K and at 4.2 K ( $f_{\perp}$  and  $f_{\parallel}$  for the respective orientations) as a function of magnetic field magnitude was estimated as:

$$f_{\perp}(B) = \frac{J_{C\perp}^{22}(B)}{J_{C\perp}^{4.2}(B)} = 0.6781 - 0.0107 \frac{B}{1T} \quad (\text{A.2a})$$

$$f_{\parallel}(B) = \frac{J_{C\parallel}^{22}(B)}{J_{C\parallel}^{4.2}(B)} = 0.7808 - 0.0105 \frac{B}{1T} \quad (\text{A.2b})$$

The magnitude of the critical current density at 4.2 K, with magnetic field oriented parallel to the tape plane ( $J_{C\parallel}^{4.2}$ ) as a function of magnetic field intensity was estimated from the data collected by Peter Lee [37]:

$$J_{C\parallel}^{4.2}(B) = \left( 4086 - 71.859 \frac{B}{1T} \right) \frac{A}{mm^2} \quad (\text{A.3})$$

The magnitude of the critical current density at 4.2 K, with magnetic field oriented perpendicular to the tape plane ( $J_{C\perp}^{4.2}$ ) as a function of magnetic field intensity was estimated from the data presented by Hazelton [8]:

$$J_{C\perp}^{4.2}(B) = 3268.2 \left( \frac{B}{1T} \right)^{-0.6442} \frac{A}{mm^2} \quad (\text{A.4})$$

The parameter  $\theta_0$  was calculated by fitting an exponential equation to the data of angle dependence of critical current of REBCO tapes at 4.2 K presented by Xu [78]. The magnetic field dependence of these values is approximately:

$$\theta_0 = 11.99^\circ - 0.069^\circ \frac{B}{1T} \quad (\text{A.5})$$



# Appendix B

## D-Shape calculation algorithm

This model is based on the calculations by Thome and Tarrh as described in [80]. The inputs are  $r_o$  and  $r_i$ , the radius of the center of the outer and inner leg of the TF coil, respectively. The output is the file *D-shape\_1.txt*, which contains the coordinates in 3 dimensions of several points along the D-shaped curve. This file was used afterwards in SolidWorks to generate the D-shaped base coils.

```
1 function [] = dshape1(r_o, r_i)
2
3 k = .5*log(r_o/r_i);
4 R = sqrt(r_i*r_o);
5 j = 3;
6
7 d = .0015 * R;
8 rho0 = r_o/R;
9 theta0 = 0;
10 P(1,1) = rho0;
11 P(1,2) = theta0;
12
13 plot (rho0, theta0);
14 hold on;
15
16 rho = rho0 - d/100;
17 theta = theta0 + log(rho) / ((k^2 - log(rho)^2)^.5) * d/100;
18 P(2,1) = rho;
19 P(2,2) = theta;
20
21 while (rho > (r_i/R) && theta < 5*R)
22     if rho < 1
23         Sign = -1;
24     else
```

```

25     Sign = +1;
26 end
27
28 if (rho > 1.3 || rho < 1.02 * r_i/R)
29     Dtheta = Sign * d;
30     Drho = Sign * (k^2 - log(rho)^2)^.5 / log(rho) * d;
31 else
32     Drho = d;
33     Dtheta = log(rho) / ((k^2 - log(rho)^2)^.5) * d;
34 end
35
36 rho = rho - Drho;
37 theta = theta + Dtheta;
38 P(j,1) = rho;
39 P(j,2) = theta;
40 j = j+1;
41 end
42
43 fileID = fopen('D-shape_1.txt','w');
44 for i = 1 : j-1
45     Q(i,1) = R*P(j-i,1);
46     Q(i,2) = R*P(j-i,2);
47     fprintf(fileID, '%f %f 0\r\n',Q(i,1),Q(i,2));
48 end
49 % top part of the D-shape
50
51 for i = j : 2 * j - 3
52     Q(i,1) = R*P(i-j+2,1);
53     Q(i,2) = -R*P(i-j+2,2);
54     fprintf(fileID, '%f %f 0\r\n',Q(i,1),Q(i,2));
55 end
56 % bottom part of the D-shape
57
58 Vert1 = R*P(j-1,1);
59 for i = 1 : 200
60     Vert2 = R*P(j-1,2)*(-1+i/100);
61     fprintf(fileID, '%f %f 0\r\n',Vert1,Vert2);
62
63 end
64 % vertical part of the D-shape
65
66 fclose(fileID);

```

# Appendix C

## Thermal properties of relevant materials

### C.1 Copper properties

Table C.1: Coefficients for copper properties calculation

Curve fit	$\rho_{Cu,1}$	$c_{p,Cu}$	$k_{Cu}$
$a_0$	$1.31 \cdot 10^{-2}$	-1.91844	2.2154
$a_1$	$1.23 \cdot 10^{-3}$	-0.15973	-0.47461
$a_2$	$-1.09 \cdot 10^{-4}$	8.61013	-0.88068
$a_3$	$3.46 \cdot 10^{-6}$	-18.9960	0.13871
$a_4$	$-3.36 \cdot 10^{-8}$	21.9661	0.29505
$a_5$	$1.42 \cdot 10^{-10}$	-12.7328	-0.02043
$a_6$	$-2.22 \cdot 10^{-13}$	3.54322	-0.04831
$a_7$	—	-0.37970	0.001281
$a_8$	—	—	0.003207

#### Electrical resistivity ( $\rho_{Cu}$ )

The electrical resistivity of copper is a function of purity ( $RRR$ ), temperature ( $T$ ) and magnetic field ( $B$ ). In this thesis all copper was assumed to have an  $RRR = 100$ .

The electrical resistivity is approximated as follows:

$$\rho_{Cu}(T, B) = \rho_{Cu,1}(T) + \rho_{Cu,2}(B) \quad (C.1)$$

Both  $\rho_{Cu,1}$  and  $\rho_{Cu,2}$  are approximated from data extracted from [44]:

$$\rho_{Cu,1}(T) = 10^{-8} \Omega m \cdot \sum_{i=0}^6 a_i \left( \frac{T}{1K} \right)^i \quad (C.2)$$

$$\rho_{Cu,2}(B) \approx 2.5 \cdot 10^{-3} \rho_{Cu}(273K, 0) \frac{B}{1T} \quad (C.3)$$

Equation (C.2) is valid for temperatures up to 200 K. The values of the coefficients are detailed in Table C.1.

Data for equation (C.3) is available for magnetic fields up to 10 T, but the equation was extrapolated beyond that value.  $\rho_{Cu}(273K, 0) = 1.545 \cdot 10^{-8} \Omega m$

### Specific heat ( $c_{p,Cu}$ )

A curve fit for the specific heat of copper is provided by NIST [81]:

$$\log_{10} \left( \frac{c_{p,Cu}(T)}{1J/(kgK)} \right) = \sum_{i=0}^7 a_i \left[ \log_{10} \left( \frac{T}{1K} \right) \right]^i \quad (C.4)$$

This equation is valid for temperatures between 4 K and 300 K. The values of the coefficients are detailed in Table C.1.

### Thermal conductivity ( $k_{Cu}$ )

Curve fits for the thermal conductivity of copper is provided by NIST [81] for several *RRR*. In this thesis all copper was assumed to have an  $RRR = 100$ . The corresponding thermal conductivity curve fit is:

$$\log_{10} \left( \frac{k_{Cu}(T)}{1W/(mK)} \right) = \frac{\sum_{i=0}^4 a_{2i} \left( \frac{T}{1K} \right)^{i/2}}{\sum_{i=1}^4 a_{2i-1} \left( \frac{T}{1K} \right)^{i/2}} \quad (C.5)$$



This equation is valid for temperatures between 4 K and 300 K. The values of the coefficients are detailed in Table C.1.

## C.2 Stainless Steel 316LN properties

Table C.2: Coefficients for stainless steel 316 properties calculation

Curve fit	$c_{p,SS,1}$	$c_{p,SS,2}$	$k_{SS}$
$a_0$	12.2486	-1879.464	-1.4087
$a_1$	-80.6422	3643.198	1.3982
$a_2$	218.743	76.70125	0.2543
$a_3$	-308.854	-6176.028	-0.6260
$a_4$	239.5296	7437.6247	0.2334
$a_5$	-89.9982	-4305.7217	0.4256
$a_6$	3.15315	1382.4627	-0.4658
$a_7$	8.44996	-237.22704	0.1650
$a_8$	-1.91368	17.05262	-0.0199

### Specific heat ( $c_{p,SS}$ )

Two curve fits for the specific heat of copper is provided by NIST [82], one for temperatures between 4 and 50 K and another for temperatures between 50 and 300 K:

$$c_{p,SS}(T) = \begin{cases} c_{p,SS,1}(T) & 4K < T < 50K \\ c_{p,SS,2}(T) & 50K < T < 300K \end{cases} \quad (C.6)$$

Both curve fits have the same shape, but different coefficients. The values of the coefficients are detailed in Table C.2.

$$\log_{10} \left( \frac{c_{p,SS,1}(T)}{1J/(kgK)} \right) = \sum_{i=0}^8 a_i \left[ \log_{10} \left( \frac{T}{1K} \right) \right]^i \quad (C.7)$$

$$\log_{10} \left( \frac{c_{p,SS,2}(T)}{1J/(kgK)} \right) = \sum_{i=0}^8 a_i \left[ \log_{10} \left( \frac{T}{1K} \right) \right]^i \quad (C.8)$$

### Thermal conductivity ( $k_{SS}$ )

A curve fit for the thermal conductivity of stainless steel 316 is provided by NIST [82]. In this thesis all copper was assumed to have an  $RRR = 100$ . The corresponding thermal conductivity curve fit is:

$$\log_{10} \left( \frac{k_{SS}(T)}{1W/(mK)} \right) = \sum_{i=0}^8 a_i \left[ \log_{10} \left( \frac{T}{1K} \right) \right]^i \quad (C.9)$$

This equation is valid for temperatures between 4 K and 300 K. The values of the coefficients are detailed in Table C.2.

## C.3 REBCO tape properties

For the thermal simulations in Chapter 6, the REBCO tape was assumed to be a  $90 \mu m$  thick tape composed of a  $50 \mu m$  stainless steel layer and a  $40 \mu m$  copper layer. Stainless steel was used instead of Hastelloy because both materials have similar thermal properties.

### Specific heat ( $c_{p,Sc}$ )

The specific heat of the REBCO tape is approximated as the weighted average of the specific heat of steel and copper:

$$c_{p,Sc}(T) = \frac{40\mu m \cdot c_{p,Cu}(T) + 50\mu m \cdot c_{p,SS}(T)}{90\mu m} \quad (C.10)$$

### Thermal conductivity

The thermal conductivity of the REBCO tape depends on the direction of heat transfer. For heat transfer across the tape (perpendicular to the face of the REBCO tape), the thermal conductivity ( $k_{Sc,\perp}$ ) is calculated as:

$$\frac{90\mu m}{k_{Sc,\perp}(T)} = \frac{40\mu m}{k_{Cu}(T)} + \frac{50\mu m}{k_{SS}(T)} \quad (C.11)$$

$$k_{Sc,\perp}(T) = \frac{90\mu m}{\frac{40\mu m}{k_{Cu}(T)} + \frac{50\mu m}{k_{SS}(T)}} \quad (C.12)$$

And for heat transfer along the tape (parallel to the face of the REBCO tape), the thermal conductivity ( $k_{Sc,\parallel}$ ) is calculated as:

$$90\mu m \cdot k_{Sc,\parallel}(T) = 40\mu m \cdot k_{Cu}(T) + 50\mu m \cdot k_{SS}(T) \quad (C.13)$$

$$k_{Sc,\parallel}(T) = \frac{40\mu m \cdot k_{Cu}(T) + 50\mu m \cdot k_{SS}(T)}{90\mu m} \quad (C.14)$$

## C.4 Gaseous Hydrogen

Table C.3: Coefficients for hydrogen gas properties calculation

Curve fit	$\mu_g$	$k_g$
$a_0$	$-1.0766 \cdot 10^{-7}$	$-1.1017 \cdot 10^{-3}$
$a_1$	$6.6342 \cdot 10^{-8}$	$9.1581 \cdot 10^{-4}$
$a_2$	$-3.6546 \cdot 10^{-10}$	$-5.0591 \cdot 10^{-6}$
$a_3$	$1.7414 \cdot 10^{-12}$	$3.8071 \cdot 10^{-8}$
$a_4$	$-4.4451 \cdot 10^{-15}$	$-1.2805 \cdot 10^{-10}$
$a_5$	$4.5464 \cdot 10^{-18}$	$1.5343 \cdot 10^{-13}$

### Mass density ( $\delta_g$ )

The density of hydrogen gas as function of pressure and temperature is approximated from the ideal gas law:

$$p = \delta_g \frac{R}{M_{H_2}} T \quad (C.15)$$

$$\delta_g(p, T) = \frac{M_{H_2} p}{RT} \quad (\text{C.16})$$

with  $R = 8.314 \text{ J}/(\text{mol K})$  the gas constant and  $M_{H_2} = 2 \cdot 10^{-3} \text{ kg/mol}$  the molar mass of hydrogen.

### Viscosity ( $\mu_g$ )

A curve was fit to the viscosity data for gaseous hydrogen at atmospheric pressure, extracted from [74]:

$$\frac{\mu_g(T)}{\text{kg}/(\text{sm})} = \sum_{i=0}^5 a_i \left( \frac{T}{1\text{K}} \right)^i \quad (\text{C.17})$$

This equation is valid for temperatures between 28 K and 300 K. The values of the coefficients are detailed in Table C.3.

### Specific heat ( $c_{p,g}$ )

The specific heat of hydrogen gas at 5 atm as function of temperature was interpolated from the data shown in Table C.4, extracted from [74].

Table C.4: Specific heat vs temperature for hydrogen gas

Temp. [K]	Specific heat [J/(kg K)]	Temp. [K]	Specific heat [J/(kg K)]	Temp. [K]	Specific heat [J/(kg K)]
27.1	17881.3	37.0	12187.6	160.0	12879.8
28.1	16477.1	38.4	11940.2	180.0	13263.7
29.1	15316.5	50.0	11321.1	200.0	13564.5
30.1	14521.9	60.0	10978.6	220.0	13808.0
31.1	14031.7	70.0	10923.0	240.0	13995.5
32.0	13358.9	80.0	10987.0	260.0	14141.9
33.1	13112.2	90.0	11145.5	270.0	14197.8
34.1	12804.9	100.0	11366.3	280.0	14247.1
35.1	12619.4	120.0	11892.2	300.0	14323.3
36.1	12373.0	140.0	12418.1	350.0	14323.3

### Thermal conductivity ( $k_g$ )

A curve was fit to the thermal conductivity data for gaseous hydrogen, extracted from [74]:

$$\frac{k_g(T)}{1W/(mK)} = \sum_{i=0}^5 a_i \left( \frac{T}{1K} \right)^i \quad (\text{C.18})$$

This equation is valid for temperatures between 28 K and 300 K. The values of the coefficients are detailed in Table C.3.

### Saturation temperature

The saturation temperature of hydrogen liquid-gas as function of pressure was interpolated from the data shown in Table C.5, extracted from [74].

Table C.5: Saturation temperature vs pressure of hydrogen liquid-gas

Temp. [K]	Pressure [kPa]
20	90.2583
21	121.1548
22	158.9397
23	204.4234
24	258.4163
25	321.9314
26	395.6778
27	480.7698
28	577.9165
29	688.2322
30	812.7299



# Bibliography

- [1] D. W. Hazelton, “SuperPower 2G HTS Conductor,” in *WAM 1st Workshop on Accelerator Magnets in HTS*, (Hamburg, Germany), 2014.
- [2] R. Rouse, “AMSC advanced conductor: 350 A/cm-w, 12 mm, copper stabilized conductor,” in *2nd HTS4Fusion Conductor Workshop*, (Villigen, Switzerland), 2014.
- [3] M. Takayasu, L. Chiesa, L. Bromberg, and J. V. Minervini, “HTS twisted stacked-tape cable conductor,” *Superconductor Science and Technology*, vol. 25, p. 014011, jan 2012.
- [4] D. C. van der Laan, X. F. Lu, and L. F. Goodrich, “Compact GdBa 2 Cu 3 O 7 $\delta$  coated conductor cables for electric power transmission and magnet applications,” *Superconductor Science and Technology*, vol. 24, p. 042001, apr 2011.
- [5] G. Celentano, “Recent developments of the ENEA HTS cable-in-conduit conductor with dual channel,” in *2nd HTS4Fusion Conductor Workshop*, (Villigen, Switzerland), 2014.
- [6] S. Ito, T. Ohinata, L. Bromberg, and H. Hashizume, “Structure Improvement and Joint Resistance Estimation in Demountable Butt and Edge Joints of a Stacked REBCO Conductor Within a Metal Jacket,” *IEEE Transactions on Applied Superconductivity*, vol. 23, pp. 4802408–4802408, jun 2013.
- [7] M. Takayasu, L. Chiesa, and J. V. Minervini, “Development of Termination Methods for 2G HTS Tape Cable Conductors,” *IEEE Transactions on Applied Superconductivity*, vol. 24, pp. 1–5, jun 2014.
- [8] D. W. Hazelton, “Applications Using SuperPower 2G HTS Conductor,” in *CEC/ICMC Conf.*, (Spokane, WA), 2011.
- [9] F. Najmabadi, R. W. Conn, P. I. H. Cooke, S. P. Grotz, M. Z. Hasan, E. Ibrahim, T. Kunugi, T.-K. Mau, R. C. Martin, and S. Sharafat, “The ARIES-I Tokamak Reactor Study,” tech. rep., University of California, Los Angeles, Los Angeles, CA, 1991.
- [10] C. Sborchia, Y. Fu, R. Gallix, C. Jong, J. Knaster, and N. Mitchell, “Design and Specifications of the ITER TF Coils,” *IEEE Transactions on Applied Superconductivity*, vol. 18, pp. 463–466, jun 2008.

- [11] G. Olynyk, Z. Hartwig, D. Whyte, H. Barnard, P. Bonoli, L. Bromberg, M. Garrett, C. Haakonsen, R. Mumgaard, and Y. Podpaly, “Vulcan: A steady-state tokamak for reactor-relevant plasmamaterial interaction science,” *Fusion Engineering and Design*, vol. 87, pp. 224–233, mar 2012.
- [12] Z. Hartwig, C. Haakonsen, R. Mumgaard, and L. Bromberg, “An initial study of demountable high-temperature superconducting toroidal field magnets for the Vulcan tokamak conceptual design,” *Fusion Engineering and Design*, vol. 87, pp. 201–214, mar 2012.
- [13] B. Sorbom, J. Ball, T. Palmer, F. Mangiarotti, J. Sierchio, P. Bonoli, C. Kasten, D. Sutherland, H. Barnard, C. Haakonsen, J. Goh, C. Sung, and D. Whyte, “ARC: A compact, high-field, fusion nuclear science facility and demonstration power plant with demountable magnets,” *Fusion Engineering and Design*, vol. 100, pp. 378–405, nov 2015.
- [14] Kaye & Laby Online, “Tables of Physical & Chemical Constants (16th edition 1995). 4.7.4 Nuclear Fusion.” [www.kayelaby.npl.co.uk](http://www.kayelaby.npl.co.uk), 2005.
- [15] J. P. Freidberg, *Plasma Physics and Fusion Energy*. Cambridge, UK: Cambridge University Press, 2008.
- [16] N. Balshaw, “All-the-Worlds-Tokamaks.” [www.tokamak.info](http://www.tokamak.info), 2015.
- [17] S. Nishio, K. Tobita, K. Ushigusa, S. Konishi, and R. D. Team, “Conceptual Design of Tokamak High Power Reactor (A-SSTR2).,” *Journal of Plasma and Fusion Research*, vol. 78, no. 11, pp. 1218–1230, 2002.
- [18] T. Ando, S. Nishio, and H. Yoshimura, “Design of the high-Tc superconducting TF coil for the tight aspect ratio tokamak power reactor (VECTOR),” *IEEE Transactions on Applied Superconductivity*, vol. 14, no. 2, pp. 1481–1484, 2004.
- [19] T. Ando and S. Nishio, “Design of the TF Coil for a Tokamak Fusion Power Reactor with YBCO Tape Superconductors,” in *21st IEEE/NPS Symposium on Fusion Engineering SOFE 05*, pp. 1–4, IEEE, sep 2005.
- [20] D. Maisonnier, “European DEMO design and maintenance strategy,” *Fusion Engineering and Design*, vol. 83, pp. 858–864, dec 2008.
- [21] C. E. Kessel, M. S. Tillack, F. Najmabadi, F. M. Poli, K. Ghantous, N. Gorelenkov, X. R. Wang, D. Navaei, H. H. Toudeshki, C. Koehly, J. P. Blanchard, C. J. Martin, L. Mynsburge, P. Humrickhouse, M. E. Rensink, T. D. Rognlien, M. Yoda, M. D. Hageman, B. H. Mills, J. D. Rader, D. L. Sadowski, P. B. Snyder, a. D. Turnbull, L. M. Waganer, S. Malang, and a. F. Rowcliffe, “The ARIES Advanced and Conservative Tokamak Power Plant Study,” *Fusion Science and Technology*, vol. 67, no. 1, pp. 1–21, 2014.
- [22] EUROfusion Consortium, “JET — EUROfusion.” <https://www.euro-fusion.org/jet/>, 2017.



- [23] Japan Atomic Energy Agency, “JT-60 Home Page.” <http://www-jt60.naka.jaea.go.jp/english/jt60/project/html/purpose.html>.
- [24] Y. Koide, K. Yoshida, M. Wanner, P. Barabaschi, A. Cucchiaro, S. Davis, P. Decool, E. Di Pietro, G. Disset, L. Genini, N. Hajnal, R. Heller, A. Honda, Y. Ikeda, Y. Kamada, Y. Kashiwa, K. Kizu, K. Kamiya, H. Murakami, F. Michel, J. Marechal, G. Phillips, G. Polli, P. Rossi, K. Shibanuma, K. Takahata, V. Tomarchio, K. Tsuchiya, K. Usui, M. Verrecchia, and L. Zani, “JT-60SA superconducting magnet system,” *Nuclear Fusion*, vol. 55, p. 086001, aug 2015.
- [25] U. S. Department of Energy Office of Science, “DIII-D National Fusion Facility (DIII-D) — U.S. DOE Office of Science (SC).” <http://science.energy.gov/fes/facilities/user-facilities/diii-d/>, 2015.
- [26] Plasma Science and Fusion Center, “Alcator C-Mod tokamak.” <http://www.psfc.mit.edu/research/topics/alcator-c-mod-tokamak>, 2016.
- [27] Y. X. Wan, P. D. Weng, J. G. Li, D. M. Gao, S. T. Wu, and EAST Team, “Progress of the EAST Project in China,” in *20th International Atomic Energy Agency (IAEA) Fusion Energy Conference*, (Vilamoura, Portugal), 2004.
- [28] National Fusion Research Institute, “KSTAR at NFRI.” [https://www.nfri.re.kr/english/research/kstar\\_operation\\_01.php](https://www.nfri.re.kr/english/research/kstar_operation_01.php).
- [29] D. Clery, “ITER fusion project to take at least 6 years longer than planned,” *Science*, nov 2015.
- [30] ITER, “ITER - the way to new energy.” <https://www.iter.org/>, 2015.
- [31] Y. Iwasa, “2.64: Superconducting Magnet Technology,” 2011.
- [32] “SuperPower Inc..” <http://www.superpower-inc.com/>.
- [33] J. F. Maguire, F. Schmidt, S. Bratt, T. E. Welsh, J. Yuan, A. Allais, and F. Hamber, “Development and Demonstration of a HTS Power Cable to Operate in the Long Island Power Authority Transmission Grid,” *IEEE Transactions on Applied Superconductivity*, vol. 17, pp. 2034–2037, jun 2007.
- [34] W. Goldacker, A. Frank, A. Kudymow, R. Heller, A. Kling, S. Terzieva, and C. Schmidt, “Improvement of Superconducting Properties in ROEBEL Assembled Coated Conductors (RACC),” *IEEE Transactions on Applied Superconductivity*, vol. 19, pp. 3098–3101, jun 2009.
- [35] M. Takayasu, J. V. Minervini, L. Bromberg, M. K. Rudziak, and T. Wong, “Investigation of twisted stacked-tape cable conductor,” in *AIP Conference Proceedings*, vol. 1435, pp. 273–280, 2012.
- [36] ITER, “Design Requirements and Guidelines Level 2. Chapter 8.1 Remote Handling Equipment - General,” tech. rep., ITER, 2001.

- [37] P. J. Lee, “A comparison of superconductor critical currents.” <http://fs.magnet.fsu.edu/lee/plot/plot.htm>, 2014.
- [38] V. Selvamanickam, M. H. Gharahcheshmeh, A. Xu, E. Galstyan, Y. Zhang, R. Pratap, R. Soriaga, G. Majkic, A. Ben Yahia, and X.-F. Li, “Heavily-doped REBCO Coated Conductors with Excellent Performance in High Fields,” in *3rd HTS4Fusion Conductor Workshop*, (Pieve S. Stefano, Italy), 2015.
- [39] G. Bansal, N. Yanagi, T. Hemmi, K. Takahata, T. Mito, and A. Sagara, “High-Temperature Superconducting Coil Option for the LHD-Type Fusion Energy Reactor FFHR,” *Plasma and Fusion Research*, vol. 3, pp. S1049–S1049, 2008.
- [40] F. Najmabadi, R. Conn, J. Bartlit, C. Bathke, W. Beecraft, J. Blanchard, L. Bromberg, J. Brooks, E. Cheng, D. Cohn, P. Cooke, R. Creedon, D. Ehst, G. Emmert, K. Evans, N. Ghoniem, S. Grotz, E. Greenspan, M. Hasan, J. Hogan, J. Herring, A. Hyatt, E. Ibrahim, S. Jardin, W. Kernbichler, M. Klasky, A. Klein, R. Krakowski, T. Kungi, J. Leuer, J. Mandrekas, R. Martin, T.-K. Mau, G. Miley, R. Miller, Y.-K. Peng, R. Reid, J. Santarius, M. Schaffer, J. Schultz, K. Schultz, J. Schwartz, S. Sharafat, C. Singer, L. Snead, D. Steiner, D. Stricker, I. Sviatoslavsky, D.-K. Sze, M. Valenti, D. Ward, J. Whitson, J. Williams, L. Wittenberg, and C. Wong, “The ARIES tokamak fusion reactor study,” in *IEEE Thirteenth Symposium on Fusion Engineering*, vol. 2, pp. 1021–1026, IEEE, 1989.
- [41] K. Osamura, S. Machiya, Y. Tsuchiya, and H. Suzuki, “Internal Strain and Mechanical Properties at Low Temperatures of Surround Cu Stabilized YBCO Coated Conductor,” *IEEE Transactions on Applied Superconductivity*, vol. 20, pp. 1532–1536, jun 2010.
- [42] C. Clickner, J. Ekin, N. Cheggour, C. Thieme, Y. Qiao, Y.-Y. Xie, and A. Goyal, “Mechanical properties of pure Ni and Ni-alloy substrate materials for YBaCuO coated superconductors,” *Cryogenics*, vol. 46, pp. 432–438, jun 2006.
- [43] J. Lu, E. S. Choi, and H. D. Zhou, “Physical properties of Hastelloy C-276 at cryogenic temperatures,” *Journal of Applied Physics*, vol. 103, no. 6, p. 064908, 2008.
- [44] C. Thompson, W. Manganaro, and F. Fickett, “Cryogenic Properties of Copper,” 1990.
- [45] H. Shin, J. Dizon, R. Ko, T. Kim, D. Ha, and S. Oh, “Reversible tensile strain dependence of the critical current in YBCO coated conductor tapes,” *Physica C: Superconductivity and its Applications*, vol. 463-465, pp. 736–741, oct 2007.
- [46] SuperPower Inc., “2015 Technology and Manufacturing Innovations at SuperPower,” tech. rep., SuperPower Inc., 2015.
- [47] Y. Iwasa, *Case Studies in Superconducting Magnets*. Boston, MA: Springer US, 2009.

- [48] M. Coatanea, J. Duchateau, S. Nicollet, B. Lacroix, and F. Topin, “Investigations About Quench Detection in the ITER TF Coil System,” *IEEE Transactions on Applied Superconductivity*, vol. 22, pp. 4702404–4702404, jun 2012.
- [49] A. Nyilas, K. Nikbin, A. Portone, and C. Sborchia, “Tensile, Fracture, Fatigue Life, and Fatigue Crack Growth Rate Behavior of Structural Materials for the ITER Magnets: The European Contribution,” in *AIP Conference Proceedings*, vol. 711, pp. 176–183, AIP, 2004.
- [50] R. P. Walsh, “Effect of an Aging Heat Treatment on the 4 K Fracture and Fatigue Properties of 316LN and Haynes 242,” in *AIP Conference Proceedings*, vol. 824, pp. 107–114, AIP, 2006.
- [51] ASM International Handbook Committee, “Maraging Steels,” in *ASM Handbook, Volume 01 - Properties and Selection: Irons, Steels, and High-Performance Alloys*, ASM International, jul 1990.
- [52] H. Nakajima, K. Yoshida, S. Shimamoto, R. Tobler, R. Reed, R. Walsh, and P. Purtscher, “Interlaboratory tension and fracture toughness test results for CSUS-JN1 (Fe-25Cr-Ni-0.35N) austenitic stainless steel at 4K,” in *Advances in Cryogenic Engineering*, vol. 36B, pp. 1069–1076, 1990.
- [53] H. Nakajima, “Structural Materials Data Handbook,” tech. rep., Superconducting Magnet Laboratory, Department of Fusion Engineering Research, Japan Atomic Energy Research Institute, 1994.
- [54] P. Libeyre, C. Brosset, P. Decool, M. Rubino, G. Bevilacqua, A. Laurenti, P. Pessenti, M. Ursuleac, N. Valle, and A. Nyilas, “Risks and benefits of Incoloy 908,” *Fusion Engineering and Design*, vol. 58-59, pp. 129–134, nov 2001.
- [55] R. Tobler, “Low temperature effects on the fracture behaviour of a nickel base superalloy,” *Cryogenics*, vol. 16, pp. 669–674, nov 1976.
- [56] Advanced Research Projects Agency and Battelle Columbus Laboratories. Metals and Ceramics Information Center, *Handbook on Materials for Superconducting Machinery*. Columbus, OH: Metals and Ceramics Information Center of the Battelle Columbus Laboratories, 1977.
- [57] R. Walsh and C. Swenson, “Mechanical Properties of Zylon/Epoxy Composite at 295K and 77 K,” *IEEE Transactions on Applied Superconductivity*, vol. 16, pp. 1761–1764, jun 2006.
- [58] Y. Huang, P. Frings, and E. Hennes, “Mechanical properties of Zylon/epoxy composite,” *Composites Part B: Engineering*, vol. 33, pp. 109–115, mar 2002.
- [59] S. G. Caldwell, “Tungsten Heavy Alloy - Design manual,” tech. rep., Tungsten Products, Madison, AL.
- [60] COMSOL Inc., “COMSOL Multiphysics 4.3b,” 2013.

- [61] M. Ferrari, P. Barabaschi, C. T. Jong, Y. Krivchenkov, R. K. Maix, and N. Mitchell, “Design optimisation of the ITER TF coil case and structures,” *Fusion Engineering and Design*, vol. 75-79, pp. 207–213, nov 2005.
- [62] R. L. Mott, *Machine Elements in Mechanical Design*, vol. 1. Upper Saddle River, NJ: Pearson Education, Inc., fourth ed., 2004.
- [63] International Nickel Limited, “Materials for Cryogenic Service: Engineering Properties of Austenitic Stainless Steels,” tech. rep., International Nickel Limited, 1974.
- [64] J. Irby, D. Gwinn, W. Beck, B. LaBombard, R. Granetz, and R. Vieira, “Alcator C-Mod Design, Engineering, and Disruption Research,” *Fusion Science and Technology*, vol. 51, no. 3, pp. 460–475, 2007.
- [65] F. J. Mangiarotti, J. Goh, M. Takayasu, L. Bromberg, J. V. Minervini, and D. Whyte, “Demountable Toroidal Field Magnets for Use in a Compact Modular Fusion Reactor,” *Journal of Physics: Conference Series*, vol. 507, p. 032030, may 2014.
- [66] W. Chung, “Mechanical and Thermal Characteristics of Insulation Materials for the KSTAR Magnet System at Cryogenic Temperature,” in *AIP Conference Proceedings*, vol. 711, pp. 297–306, AIP, 2004.
- [67] W. Chung, K. Lee, K. Park, Y. Oh, and J. S. Bak, “Electrical Insulation of KSTAR Magnet Lead,” *Journal of the Korean Physical Society*, vol. 49, no. December, pp. S228–S231, 2006.
- [68] P. Avivi and F. Deutsch, “A possible deviation from Paschen’s law in hydrogen at low temperature,” *British Journal of Applied Physics*, vol. 14, no. 11, p. 819, 1963.
- [69] R. A. Haarman and K. D. Williamson, “Electrical Breakdown and Tracking Characteristics of Pulsed High Voltages in Cryogenic Helium and Nitrogen,” in *Advances in Cryogenic Engineering*, pp. 102–108, Boston, MA: Springer US, 1960.
- [70] M. Takayasu, F. J. Mangiarotti, J. V. Minervini, L. Bromberg, L. Chiesa, N. Allen, W. Nachtrab, M. K. Rudziak, and T. Wong, “Development of REBCO Twisted Stacked-Tape Cables for Magnet Application,” in *1st Workshop on Accelerator Magnets in HTS*, (Hamburg, Germany), 2014.
- [71] R. Holm, *Electric Contacts*. Berlin, Heidelberg: Springer Berlin Heidelberg, 1967.
- [72] D. Smith and F. Fickett, “Low-Temperature Properties of Silver,” *Journal of Research of the National Institute of Standards and Technology*, vol. 100, p. 119, mar 1995.

- [73] P. Kittel, “Cryocooler Performance Estimator,” *Cryocoolers*, vol. 14, pp. 563–572, 2007.
- [74] J. Jensen, W. Tuttle, R. Stewart, H. Brechna, and A. Prodell, “Properties of Hydrogen,” in *Brookhaven National Laboratory Selected Cryogenic Data Notebook*, ch. 3, Brookhaven National Laboratory, Associated Universities Inc., 1980.
- [75] T. L. Bergman, A. S. Lavine, F. P. Incropera, and D. P. DeWitt, *Fundamentals of Heat and Mass Transfer*. Jefferson City: John Wiley & Sons, Inc., 2011.
- [76] Westinghouse Electric Corporation, *The Westinghouse Pressurized Water Reactor Nuclear Power Plant*. Pittsburgh, PA: Westinghouse Electric Corporation, 1984.
- [77] S. Hahn, D. K. Park, J. Bascunan, and Y. Iwasa, “HTS Pancake Coils Without Turn-to-Turn Insulation,” *IEEE Transactions on Applied Superconductivity*, vol. 21, pp. 1592–1595, jun 2011.
- [78] A. Xu, Y. Viouchkov, C. Tarantini, V. Griffin, J. Lu, J. Jaroszynski, D. Larbalestier, Y. Chen, Y.-Y. Xie, and V. Selvamanickam, “Angular dependent  $J_c$  at very high field in YBCO coated conductors,” in *International Workshop on Coated Conductors for Applications*, (Houston, TX), 2008.
- [79] SuperPower Inc., “Temperature vs. Field Data of SuperPower Advanced Pinning (“AP”) 2G HTS Wire,” tech. rep., SuperPower Inc., 2010.
- [80] R. J. Thome and J. M. Tarrh, *MHD and fusion magnets*. New York, NY: John Wiley & Sons, Inc., 1982.
- [81] National Institute of Standards and Technology, “Material Properties: OFHC Copper (UNS C10100/C10200).” [http://cryogenics.boulder.nist.gov/MPropsMAY/OFHC%20Copper/OFHC\\_Copper\\_rev1.htm](http://cryogenics.boulder.nist.gov/MPropsMAY/OFHC%20Copper/OFHC_Copper_rev1.htm), 2010.
- [82] National Institute of Standards and Technology, “Material Properties: 316 Stainless (UNS S31600).” [http://www.cryogenics.nist.gov/MPropsMAY/316Stainless/316Stainless\\_rev.htm](http://www.cryogenics.nist.gov/MPropsMAY/316Stainless/316Stainless_rev.htm).